ISSN : 2349-6495(P) | 2456-1908 (O)

International Journal of Advanced Engineering Research and Science

(IJAERS)

An Open Access Peer-Reviewed International Journal

Journal DOI: 10.22161/ijaers

Issue DOI: 10.22161/ijaers.133

AI PUBLICATIONS

Vol.- 13 | Issue - 3 | Mar 2026

editor.ijaers@gmail.com | editor@ijaers.com | https://www.ijaers.com/

International Journal of Advanced Engineering Research and Science (IJAERS)

(ISSN: 2349-6495(P)| 2456-1908(O))

DOI: 10.22161/ijaers

Vol-13, Issue-3

March, 2026

Publisher

AI Publication

Email: editor.ijaers@gmail.com; editor@ijaers.com

Web: www.ijaers.com

International Editorial/ Reviewer Board

- **Dr. Neel Kamal Purohit,** S.S. Jain Subodh P.G. College, Rambagh, Jaipur, India
- **Mohd Muntjir,** Taif University, Kingdom of Saudi Arabia
- **Xian Ming Meng,** China Automotive Technology & Research Center No.68, East Xianfeng Road, Dongli District, Tianjin, China
- **Herlandi de Souza Andrade,** FATEC Guaratingueta, State Center for Technological Education Paula Souza - CEETEPS
- **Dr. Payal Chadha,** University of Maryland University College Europe, Kuwait
- **Ahmed Moustafa Abd El-hamid Elmahalawy,** Menoufia University, Al Minufya, Egypt
- **Prof. Mark H. Rummeli,** University & Head of the characterisation center, Soochow Institute for Energy Materials Innovasions (SIEMES), Suzhou, Jiangsu Province, China
- **Dr. Eman Yaser Daraghmi,** Ptuk, Tulkarm, Palestine
- **Holmes Rajagukguk,** State University of Medan, Lecturer in Sisingamangaraja University North Tapanuli, Indonesia
- **Dr. Menderes KAM,** Dr. Engin PAK Cumayeri Vocational School, DÜZCE UNIVERSITY (University in Turkey), Turkey
- **Dr. Jatin Goyal,** Punjabi University, Patiala, Punjab, India | International Collaborator of GEITEC / UNIR / CNPq, Brazil
- **Ahmet İPEKÇİ,** Dr. Engin PAK Cumayeri Vocational School, DÜZCE UNIVERSITY, Turkey
- **Baarimah Abdullah Omar,** Universiti Malaysia Pahang (UMP), Gambang, 26300, Malaysia
- **Sabri UZUNER,** Dr. Engin PAK Cumayeri Vocational School Cumayeri/Duzce/Turkey
- **Ümit AĞBULUT,** Düzce University, Turkey
- **Dr. Mustafa ÖZKAN,** Trakya University, Edirne/ TURKEY
- **Dr. Indrani Bhattacharyya,** Dr. B.C. Roy College of Pharmacy and Allied Health Sciences, Durgapur, West Bengal, India
- **Egnon Kouakouc,** Nutrition/Health at University Felix Houphouet Boigny Abidjan, Ivory Coast
- **Dr. Suat SARIDEMİR,** Düzce University, Faculty of Technology, Turkey
- **Dr. Manvinder Singh Pahwa,** Director, Alumni Relations at Manipal University Jaipur, India
- **Omid Habibzadeh Bigdarvish,** University of Texas at Arlington, Texas, USA
- **Professor Dr. Ho Soon Min,** INTI International University, Jln BBN 12/1, Bandar, Baru Nilai, 71800 Negeri Sembilan, Malaysia
- **Ahmed Mohammed Morsy Hassan,** South Egypt Cancer Institute, Assiut University, Assiut, Egypt
- **Xian Ming Meng (Ph.D),** China Automotive Technology & Research Center, No.68, East Xianfeng Road, Tianjin, China
- **Ömer Erkan,** Konuralp Campus, Düzce-Turkey
- **Dr. Yousef Daradkeh,** Prince Sattam bin Abdulaziz University) PSAU), KSA
- **Peter JO,** IPB University, Indonesia
- **Nazmi Liana Binti Azmi,** Raja Perempuan Zainab II Hospital, 15586 Kota Bharu, Kelantan, Malaysia
- **Mr. Sagar Jamle,** Oriental University, Indore, India
- **Professor Grazione de Souza,** Applied Mathematics, Rio de Janeiro State University, Brazil
- **Kim Edward S. Santos,** Nueva Ecija University of Science and Technology, Philippines.
- **Dr. Jhonas Geraldo Peixoto Flauzino,** Department of Neurosciences, Pontifical Catholic University of Rio Grande do Sul, Brazil.
- **Narender Chinthamu,** Massachusetts Institute of Technology, 7 Massachusetts Ave, Cambridge, MA 02139
- **Dr. Geeta S Nadella,** CSP-SM | Quality Assurance Specialist IEEE ENCS CS Chair
- **Dr. Karthik Meduri,** University of the Cumberlands, Kentucky, USA

Vol-13, Issue-3, March 2026

(10.22161/ijaers.133)

Detail with DOI (CrossRef)

International Journal of Advanced Engineering Research and Science (IJAERS)
Peer-Reviewed Journal
ISSN: 2349-6495(P) | 2456-1908(O)
Vol-13, Issue-3; Mar, 2026
Journal Home Page Available: https://ijaers.com/
Article DOI: https://dx.doi.org/10.22161/ijaers.133.1

Effects of Social Media Entertainment, e-WOM and Trendiness on Fashion Consumers Purchase Intention: A Stimulus–Organism–Response Perspective

Md Yousof Talukdar[1], Liu Lixian[2], Md Kowsar Alam Sarkar[3]

[1]MSc Student in Fashion Design and Engineering, Zhejiang Sci-Tech University, Hangzhou, China.
Email: 20232104e3005@mails.zstu.edu.cn
[2]Professor, Fashion Design College of Istituto Marangoni, Zhejiang Sci-Tech University, Hangzhou, China.
Email: adio1983@zstu.edu.cn
[3]MSc Student in Fashion Design and Engineering, Zhejiang Sci-Tech University, Hangzhou, China.
Email: 20242104e4007@mails.zstu.edu.cn

Received: 25 Jan 2026,

Received in revised form: 23 Feb 2026,

Accepted: 28 Feb 2026,

Available online: 05 Mar 2026

***Keywords*— Social media marketing, Entertainment, e-WOM, Trendiness, Brand engagement, Purchase intention.**

***Abstract*—** *This study examines the relationships between social media marketing stimuli—namely entertainment, electronic word of mouth, and trendiness—and fashion consumers' purchase intentions, with brand engagement serving as a mediating variable within the Stimulus-Organism-Response (SOR) framework. Data were collected from fashion consumers in Bangladesh using a cross sectional survey and a convenience sampling technique. A total of 270 valid responses were analyzed. Data analysis was conducted using IBM SPSS Statistics through reliability, correlation, and regression analyses. Mediation effects were examined using bootstrapping procedures with PROCESS Macro.*

I. INTRODUCTION

In the digital age, social media platforms have become pivotal in shaping consumer behavior and purchase decisions in the fashion industry (Bommawar & Tiwari, 2022). Research indicates that consumers increasingly use social media to interact with brands and obtain product information, making digital platforms central to contemporary fashion consumption (Bonilla-Quijada et al., 2024; Muturi, 2024; Xue et al., 2023). Platforms such as Instagram, Facebook, TikTok, and YouTube have transformed the ways fashion brands engage with consumers by enabling personalized, interactive, and trend-oriented marketing experiences (Ismagilova et al., 2020; Khraiwish & Alsharif, 2024). Within the fashion industry, these platforms provide brands with unprecedented opportunities to influence purchase intentions through entertaining content, peer communication channels, and continuous exposure to emerging trends (Asmirani & Islamiah, 2025; Bilal M, 2021).

Entertainment, as a core component of social media marketing, enhances consumer engagement by delivering enjoyable and captivating content that strengthens emotional attachment and brand involvement, thereby positively influencing purchase intentions (Bilal et al., 2021; Cheung et al., 2021; Thanasi-Boçe et al., 2022). Similarly, electronic word-of-mouth (e-WOM) allows consumers to share experiences with a broader audience, increasing perceived credibility and reducing purchase uncertainty, which significantly shapes fashion consumers' decision-making processes (Chia-Jo et al., 2023; Dwivedi et al., 2021; Ismagilova et al., 2020). Trendiness, reflecting the novelty and relevance of social media content, attracts consumer attention and motivates interaction with fashion brands, ultimately influencing purchasing behavior (Appel et al.,

2020; Felix et al., 2017; Zahra, 2025). Collectively, entertainment, e-WOM, and trendiness represent powerful external stimuli that shape consumers cognitive, affective, and behavioral responses in digital environments (Kian Yeik et al., 2021).

The Stimulus–Organism–Response (S–O–R) framework provides a theoretical lens for understanding how these marketing stimuli affect consumer behavior (Cheung et al., 2021; Y. Huang et al., 2024). External stimuli (S), such as entertainment, e-WOM, and trendiness, influence internal psychological states organism (O), including engagement, emotions, and attitudes, which subsequently drive behavioral responses (R) like purchase intentions (Yadav & Rahman, 2018). Previous research has validated the S–O–R framework in online marketing contexts, demonstrating its effectiveness in explaining how digital stimuli translate into consumer purchase behavior (Cheung et al., 2021; Kian Yeik et al., 2021).

Despite these findings, most studies have examined social media marketing elements in isolation, without an integrated framework explaining their combined effect on purchase intentions (Asmirani & Islamiah, 2025; Bilal M, 2021). Furthermore, in emerging markets such as Bangladesh, rapid social media adoption and increasing digital connectivity have amplified consumers' influence on fashion trends and brand perceptions (Pick, 2021; Taher, 2022). Young consumers, who are highly active on social media platforms, play a particularly important role in shaping market dynamics and fashion consumption patterns (Ebrahimi et al., 2022; Ying et al., 2021).

Addressing these gaps, the present study investigates the effects of social media entertainment, e-WOM and trendiness on fashion consumers purchase intentions, while examining the mediating role of brand engagement through the S–O–R framework (Bonilla-Quijada et al., 2024; Ismagilova et al., 2020; Muturi, 2024). The findings aim to provide actionable insights for fashion brands seeking to optimize social media strategies and understand the psychological processes driving purchase behavior in digital environments (Bilal et al., 2021; Khraiwish & Alsharif, 2024).

II. LITERATURE REVIEW

2.1 EMPIRICAL LITERATURE REVIEW

Social media marketing has fundamentally reshaped consumer interactions in the fashion industry, with studies indicating that consumers increasingly rely on digital platforms when making purchase decisions for apparel and fashion products (Bommawar & Tiwari, 2022). Unlike traditional marketing channels, social media enables continuous, bidirectional interactions, allowing brands to cultivate relationships that extend beyond mere information dissemination (El-Shihy & Awaad, 2025). This shift toward interactive communication ecosystems has been shown to strengthen consumers' attitudes toward social commerce and encourage adoption of online purchasing behaviors (Cho & Son, 2019). In emerging markets such as Bangladesh, rising mobile internet penetration further intensifies these dynamics, positioning social media as a dominant marketing interface for fashion brands seeking digitally active audiences (Zaki et al., 2025).

Social media platforms, including Facebook, Instagram, TikTok, and YouTube, provide brands with versatile content marketing infrastructures that integrate visual storytelling, video-based persuasion, and interactive functionalities (Banjongprasert, 2024; Kaplan & Haenlein, 2010). Interactive features like likes, shares, and comments facilitate consumer participation, increasing brand involvement and emotional attachment, which in turn strengthens purchase intentions (Thanasi-Boçe et al., 2022). Additionally, user-generated content and peer interactions enhance perceived authenticity and credibility, allowing consumers to contribute to brand narratives and influence one another's purchasing decisions (Abdelsalam et al., 2024).

The strategic use of entertaining and trend-oriented content is crucial in fashion marketing, as consumers seek experiences that align with their preferences for enjoyment and novelty (Moghddam et al., 2025). Empirical evidence highlights that exposure to such content positively affects consumer perceptions, emotional engagement, and brand loyalty (Fetais et al., 2023; George et al., 2025). Social media marketing also allows brands to disseminate emerging fashion trends rapidly, reinforcing perceptions of modernity and relevance, which are key drivers of purchase behavior in fashion (Pan et al., 2025; Xu, 2025). In Bangladesh, creating culturally relevant and locally tailored content enhances engagement with younger demographics, who are the primary drivers of fashion consumption (Chatterjee et al., 2025; Ismael et al., 2025).

Furthermore, social media facilitates electronic word-of-mouth (e-WOM), which significantly shapes fashion consumers' decision-making processes. Consumers increasingly rely on reviews, recommendations, and shared experiences from peers and influencers to reduce uncertainty and validate their purchasing choices (Alfraihat et al., 2025; Ntousi et al., 2025). The feedback loop inherent in social media platforms also allows brands to continuously refine content strategies based on consumer interactions, thereby enhancing the effectiveness of marketing campaigns (John et al., 2025; Sherief et al., 2025).

From a theoretical standpoint the Stimulus–Organism–Response (S-O-R) framework**,** social media marketing activities function as external stimuli (S) that influence internal consumer states (O), including perceived enjoyment, brand trust, and engagement, which ultimately drive purchase intentions (Alfraihat et al., 2025). This theoretical lens helps explain the psychological mechanisms through which fashion consumers process social media content and convert it into behavioral outcomes, emphasizing the strategic importance of integrated, content-rich, and interactive marketing approaches for fashion brands (Fetais et al., 2023; Pan et al., 2025).

Despite extensive empirical evidence on social media marketing outcomes, limited research integrates entertainment, e-WOM and trendiness within a unified S–O–R framework to explain fashion consumers purchase intentions.

2.2 THEORETICAL FOUNDATIONS AND HYPOTHESIS DEVELOPMENT

Stimulus - Organism - Response (S-O-R) Theory

The Stimulus–Organism–Response (S-O-R) theory**,** first proposed by (Mehrabian & Russell, 1974), explains how external environmental stimuli influence individuals internal psychological states, which in turn shape behavioural responses (Lee, 2024). The primary advantage of using this S-O-R model here is its ability to explain how individuals' emotional states (the organism) are influenced by different environmental elements and lead to their behavioural responses (Zhang et al., 2023). Stimulus refers to the external factors that lead to changes within the individual, organism refers to the internal psychological state of the individual, and response refers to the corresponding behaviour triggered by these external stimuli (Li et al., 2024).

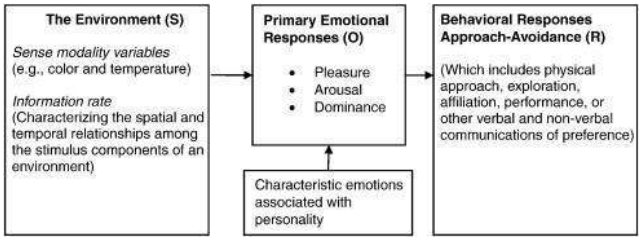

Fig. 1: S–O–R framework Mehrabian and Russell (Vieira, 2013)

Source: Mehrabian and Russell (1974, p.8) (Vieira, 2013).

Empirical evidence from social commerce research demonstrates that social media cues influence internal states including perceived enjoyment, brand engagement, which mediate the relationship between external stimuli and purchase intention (Bui et al., 2025). Therefore, applying the SOR framework provides a theoretically robust basis for examining the mechanisms through which social media marketing characteristics shape fashion consumers' purchase intentions (Luo et al., 2025).

2.2.1 STIMULUS (S): SOCIAL MEDIA

Social media has become a pivotal external stimulus influencing purchase intention in the fashion industry. Platforms such as Instagram, Facebook, TikTok, and YouTube enable brands to deliver targeted, interactive, and personalized content (Antczak, 2024). Key stimuli embedded within social media marketing entertainment, e-WOM, and trendiness—significantly influence consumer responses. Entertaining and engaging content enhances emotional connections and consumer engagement (Bilal et al., 2021). while e-WOM, including reviews and endorsements, strengthens trust and reduces purchase uncertainty (Febyola & Widyanesti, 2024). Trendiness, driven by the rapid diffusion of fashion trends, captures attention and encourages brand interaction (Appel et al., 2020). These stimuli foster positive emotional and psychological responses, reinforcing brand engagement and ultimately enhancing purchase intentions (Hu & Zhu, 2022; Leong et al., 2022; Ngo et al., 2025). Integrating these stimuli into a cohesive strategy helps brands guide consumer decision-making and strengthen purchase intentions (Muturi, 2024).

Based on the reviewed literature, the conceptual framework is presented in Fig. 2.

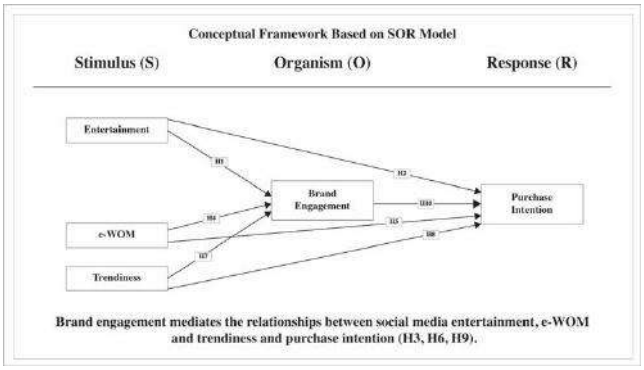

Fig. 2: Conceptual framework of the study Based on S-O-R Model

Using this framework, the study develops hypotheses to examine the relationships among social media stimuli, organismic variables, and purchase intention within the proposed S–O–R model.

2.2.1.1 ENTERTAINMENT

People use various social media sites for entertainment, information, and virtual social experiences (Garg & Bakshi, 2024). In marketing, entertainment refers to creating engaging content that resonates with the target audience and captivates users through creativity and interactivity (Kethuda & Ayoubi, 2025; Lin et al., 2024). Marketers can enhance entertainment value by incorporating humor, creativity, and visually appealing elements to reach a broader audience (van Deventer & Saraiva, 2025). Empirical studies show that highly engaging content increases user interaction, strengthens emotional connections, and fosters favorable perceptions of the brand (Bilal M, 2021). Entertainment, as a stimulus in the S–O–R framework, elicits cognitive and emotional responses that may influence purchase intention. The following hypothesis is proposed:

H1: Social media entertainment positively influences brand engagement.

H2: Social media entertainment positively affects purchase intention (direct effect).

H3: Brand engagement mediates the relationship between social media entertainment and purchase intention.

2.2.1.2 ELECTRONIC WORD-OF-MOUTH (E-WOM)

Electronic word-of-mouth (e-WOM) significantly shapes consumer decision-making in digital fashion purchases (Ngo et al., 2024). On social media, e-WOM appears as user-generated posts, reviews, discussions, and fan communities, through which consumers share opinions and recommendations about fashion brands (Rahaman et al., 2022). Acting as an external informational cue, e-WOM guides consumer evaluation (Kim et al., 2018), with positive e-WOM enhancing brand credibility and engagement, and negative e-WOM increasing perceived risk and reducing interaction (Erkan & Evans, 2018; Filieri, 2015). Social platforms facilitate rapid dissemination, allowing users to influence peers and shape brand perceptions (Nabivi, 2025; Putri et al., 2023). Within the Stimulus–Organism–Response (SOR) framework, e-WOM is a key external stimulus (S) that can trigger internal evaluations and ultimately affect purchase intention (Cheung & Thadani, 2012). Accordingly, the following hypothesis is proposed:

H4: e-WOM positively affects brand engagement.

H5: e-WOM positively affects purchase intention (direct effect).

H6: Brand engagement mediates the relationship between e-WOM and purchase intention.

2.2.1.3 TRENDINESS –

Trendiness refers to the extent to which social media content delivers up-to-date and fashionable information about products or services (Wilopo & Nuralam, 2025). Timely and frequent posts effectively capture consumer attention (M. Huang et al., 2024). Trending products are perceived as attractive, socially endorsed, and aligned with prevailing norms (Andonopoulos et al., 2023; Nguyen et al., 2024), enabling fashion brands to enhance engagement, visibility, and competitiveness on social media (Anas et al., 2023). Empirical evidence shows that trendiness positively influences consumer perceptions and behavioral intentions, especially among younger consumers (Ibrahim et al., 2020). In the SOR framework, trendiness serves as an external stimulus (S) that influences internal responses, ultimately shaping purchase intention. Accordingly, the following hypothesis is proposed:

H7: Trendiness positively affects brand engagement.

H8: Trendiness positively affects purchase intention (direct effect).

H9: Brand engagement mediates the relationship between trendiness and purchase intention.

2.2.2 ORGANISM (O): BRAND ENGAGEMENT

Within the S–O–R framework, the organism represents consumers' internal psychological states that mediate the effect of external stimuli on behavior, including cognitive, emotional, and motivational processes such as brand engagement (Hollebeek, 2011; Mehrabian & Russell, 1974). These states explain how consumers interpret and process social media stimuli—entertainment, e-WOM, and trendiness—before forming purchase intentions, highlighting how psychological involvement transforms marketing stimuli into actionable responses (Lin & Shen, 2023; Zahrah et al., 2024).

In fashion, brand engagement captures consumers' emotional, cognitive, and behavioral connection with a brand (Park & Ha, 2021), expressed through attention, affective attachment, and participation in brand-related social media activities (Aziz et al., 2025). Exposure to entertaining or trend-aligned content enhances engagement, which mediates the effect of social media stimuli on purchase intention (Thanasi-Boçe et al., 2022; Wang et al., 2024). Accordingly, the following hypothesis is proposed:

H10: Brand engagement positively influences purchase intention.

2.2.3 RESPONSE (R): PURCHASE INTENTION

Purchase intention refers to a consumer's likelihood or willingness to buy a product in the future, reflecting motivational readiness and the probability of action (Bogdan et al., 2025). In social media contexts, it predicts actual buying behavior, shaped by digital information, peer reviews, and interactive engagement (Utami & Astuti, 2024). Within the Stimulus–Organism–Response (SOR)

framework, purchase intention is the behavioral outcome of consumers' internal evaluations of social media stimuli. Entertainment enhances enjoyment and relevance (Omeish et al., 2024), e-WOM facilitates information adoption and engagement (Bui et al., 2025), and trendiness reinforces self-expression and fashion identity, all contributing to stronger purchase intention through brand engagement (Ningrum & Susila, 2025).

In this study, purchase intention is modeled as the final behavioral response within the S–O–R framework and is influenced both directly by social media stimuli and indirectly through brand engagement, as specified in the proposed hypotheses.

III. RESEARCH METHODOLOGY

3.1 RESEARCH DESIGN

This study adopts a quantitative, explanatory, and cross-sectional research design to examine the effects of social media entertainment, electronic word-of-mouth (e-WOM), and trendiness on fashion consumers' purchase intention, with brand engagement acting as a mediating variable. A quantitative approach is appropriate as the study aims to test hypothesized relationships between constructs and to generalize findings across a defined population. The cross-sectional design allows data to be collected at a single point in time, which is suitable for analyzing consumer perceptions and behavioral intentions in the context of social media marketing.

3.2 POPULATION AND SAMPLING TECHNIQUE

The target population for this study comprises fashion consumers in Bangladesh who actively use social media platforms (such as Facebook, Instagram, and TikTok) to access fashion-related information, follow fashion brands, or interact with fashion content. These individuals are suitable respondents as they are exposed to social media entertainment, e-WOM, and trend-related information relevant to the study variables.

A non-probability convenience sampling method was employed due to accessibility limitations and the exploratory nature of research on consumer behavior in digital contexts. Data were collected from respondents who met the screening criteria of being active social media users with prior experience engaging with fashion-related content online.

3.3 SAMPLE SIZE DETERMINATION

The sample size was determined based on established guidelines for multivariate analysis, which recommend a minimum of 10 responses per observed variable to ensure reliable results. With 270 respondents, the study comfortably exceeds this minimum requirement, providing sufficient data for robust statistical analysis. This sample size is also consistent with previous research on social media marketing and purchase intention.

3.4 DATA COLLECTION TECHNIQUES

Primary data were collected using a structured questionnaire distributed online through social media platforms and messaging applications. Online data collection is appropriate for this study as the research context involves social media usage and digital consumer behavior. Participation will be voluntary, and respondents will be informed about the academic purpose of the study prior to completing the questionnaire.

3.5 DATA ANALYSIS TECHNIQUES

The collected data were analyzed using descriptive statistics to summarize respondent characteristics and survey responses. Reliability and convergent validity were assessed using Cronbach's Alpha and factor loadings, while Pearson correlation and regression analyses were conducted to examine relationships and the influence of independent variables on purchase intention. Mediator effects were tested using the PROCESS macro to evaluate the indirect impact of the mediating variable.

3.6 ETHICAL CONSIDERATIONS

Ethical considerations are essential to ensure the credibility and integrity of this research. Informed consent was obtained from all participants prior to their participation in the online survey, and they were clearly informed that the data collected would be used solely for academic purposes. Participants' identities were kept confidential at all times. Additionally, academic integrity was upheld throughout the literature review, with all sources properly cited and referenced to avoid plagiarism.

IV. RESULTS

4.1 DESCRIPTIVE STATISTICS

The study surveyed 270 participants. Among the participants, the largest age group was 25–34 years comprising 63% of the sample, the next most significant group was 18–24 years representing 31.50%. The remaining 5.60% were aged 35 and above.

The gender distribution shows a higher proportion of male respondents 62.20% compared to female respondents 37.80%, indicating a moderate gender imbalance in the sample. While both groups are represented, this disparity should be considered when interpreting gender-related differences in fashion content preferences.

Regarding educational background, a large number of participants 61.90% held a bachelor's degree, while 31.90%

of respondents had completed a master's degree or higher. A smaller segment of the respondents 4.80% possessed a Diploma degree, and only 1.50% had completed their education at the high school level.

The most popular platform for fashion content was Facebook with 58.50%, followed by other platforms like Instagram at 29.30%, TikTok at 2.60%, YouTube at 6.70% and various others platforms like twitter, Snapchat, etc. accounted for 2.80%.

The study also looked at the time participants spent on social media daily. 34.40% of the respondents reported spending more than 4 hours per day on social media, followed by 28.10% of participants spending 3–4 hours daily. Additionally, 34.40% spent 1-2 hours, and a smaller portion 3.0% spending less than 1 hour per day on social media. These insights offer a comprehensive analysis of engagement levels and platform choices among social media users interacting with fashion content.

Table. 1: Socio-demographic characteristics of the respondents (N=270)

Characteristics	Category	Frequency	%
Gender	Male	168	62.20%
	Female	102	37.80%
Age	18-24	85	31.50%
	25-34	170	63%
	35-44	16	5.60%
Education Level	Intermediate / High School	4	1.50%
	Diploma	13	4.80%
	Bachelor's Degree	167	61.90%
	Master's Degree or above	86	31.90%
Primary Social Media Platform	Facebook	158	58.50%
	Instagram	79	29.30%
	TikTok	7	2.60%
	YouTube	18	6.70%
	Others	8	2.80%
Average daily time spend on social media	Less than 1 hour	8	3.0%
	1-2 Hours	93	34.40%
	3-4 Hours	76	28.10%
	More than 4 Hours	93	34.40%

4.2 RELIABILITY AND CONVERGENT VALIDITY

Table. 2: Reliability and Convergent Validity

Variables	Items	Mean	SD	Item Loading	CR	AVE	Cronbach's Alpha
EN	EN1	3.86	1.063	0.889	0.9497	0.8251	0.929
	EN2	3.66	1.164	0.914			
	EN3	3.61	1.173	0.922			
	EN4	3.72	1.154	0.908			
e-WOM	EWOM1	3.49	1.113	0.800	0.899	0.690	0.848
	EWOM2	3.33	1.231	0.825			

	EWOM3	3.45	1.082	0.870			
	EWOM4	3.80	1.042	0.826			
TR	TR1	3.77	1.042	0.798	0.908	0.713	0.863
	TR2	4.01	0.904	0.827			
	TR3	3.99	0.974	0.888			
	TR4	4.09	0.916	0.862			
BE	BE1	3.46	1.146	0.847	0.918	0.736	0.880
	BE2	3.70	1.046	0.853			
	BE3	3.39	1.040	0.883			
	BE4	3.51	1.140	0.848			
PI	PI1	3.68	0.966	0.828	0.9147	0.7284	0.875
	PI2	3.89	1.023	0.882			
	PI3	3.81	1.068	0.849			
	PI4	3.82	1.006	0.854			

Note: SD= Standard Deviations, CR = Composite Reliability, AVE = Average Variance Extracted

The factor loadings in this study indicate strong convergent validity of the underlying constructs, as all factor loadings surpassed 0.5 and were highly significant ($p < 0.001$). This suggests that each item contributes meaningfully to its respective construct, reinforcing the importance of the underlying structures. Specifically, the Factor Loadings for entertainment (EN) items ranged from 0.889 to 0.914, for e-WOM items from 0.800 to 0.870, for trendiness (TR) from 0.798 to 0.888, for brand engagement (BE) from 0.847 to 0.883, and for purchase intention (PI) from 0.828 to 0.8882, all indicating robust relationships between the items and the constructs.

Furthermore, Cronbach's Alpha values for all constructs were above 0.80, demonstrating excellent internal consistency. Specifically, entertainment (EN) had Cronbach's Alpha values of 0.929, e-WOM had 0.848, trendiness (TR) had 0.863 brand engagement (BE) had 0.880, and purchase intention (PI) had 0.875. All these values fall within the acceptable range for reliability, indicating good internal consistency across the measures.

In summary, the reliability and validity of the constructs are satisfactory, with all factor loadings exceeding 0.5, and Cronbach's Alpha values confirming good internal consistency across the measures. The convergent and discriminant validity tests further support the robustness of the measurement model.

4.3 CORRELATION ANALYSIS

Table. 3: Pearson Correlation Matrix

Variable	EN	e-WOM	TR	BE	PI
EN	1	0.609**	0.675**	0.608**	0.542**
e-WOM	0.609**	1	0.562**	0.579**	0.530**
TR	0.675**	0.562**	1	0.629**	0.627**
BE	0.608**	0.579**	0.629**	1	0.744**
PI	0.542**	0.530**	0.627**	0.744**	1

Note**:** Pearson's r represents the strength and direction of the correlation. p-value < 0.001 indicates statistical significance at the 0.01 level (two-tailed), marked with asterisks (**).

The correlation analysis reveals that all variables are positively and significantly correlated at the 0.01 level (two-tailed). The strongest correlation is between brand engagement (BE) and purchase intention (PI) **(**r = 0.744). Entertainment (EN) shows strong correlations with e-WOM **(**r = 0.609), trendiness (TR) (r = 0.675), and brand engagement (BE) **(**r = 0.608), while trendiness (TR) also correlates strongly with both brand engagement (BE) **(**r = 0.629**)** and purchase intention (PI) **(**r = 0.627).

4.4 REGRESSION COEFFICIENTS

4.4.1 HYPOTHESIS TESTING

Table. 4: Regression Coefficients (Hypothesis Testing)

H	Path	Estimates (B)	SE	(t) CR	p-value	Result
H1	EN → BE	0.571	0.046	12.535	p < 0.001	Supported
H2	EN → PI	0.454	0.043	10.546	p < 0.001	Supported
H4	e-WOM → BE	0.606	0.052	11.618	p < 0.001	Supported
H5	e-WOM → PI	0.495	0.048	10.236	p < 0.001	Supported
H7	TR → BE	0.755	0.057	13.239	p < 0.001	Supported
H8	TR → PI	0.671	0.051	13.159	p < 0.001	Supported
H10	BE → PI	0.833	0.046	18.211	p < 0.001	Supported

Note: SE = Standard Error, CR = Critical Ratio, ***p-value < 0.001, **P < 0.05

The regression analysis highlights the significant roles of entertainment, e-WOM and trendiness in influencing brand engagement and purchase intention. Entertainment (EN) positively affects both brand engagement (BE) (0.571) and purchase intention (PI) (0.454), with strong significance. e-WOM also plays a key role, driving brand engagement (BE) (0.606) and purchase intention (PI) (0.495) significantly. Trendiness (TR) shows a particularly strong influence, enhancing both brand engagement (BE) (0.755) and purchase intention (PI) (0.671), with high significance. Lastly, brand Engagement (BE) is a powerful driver of purchase intention (PI) (0.833). These results underline the importance of entertainment, e-WOM, and trendiness in shaping consumer behavior, particularly in driving brand engagement and purchase decisions.

4.4.2 MEDIATOR ANALYSIS

Table. 5. Regression Coefficients (Mediator analysis)

Dependent Variable	Effect of IV on M (a)		Effect of M on DV (b)		Total Effect of IV on DV (c)		Direct Effect of IV on DV(c')		Bootstrap Result for Indirect Effect (ab)		Result
	β	**t**	**β**	**t**	**β**	**t**	**β**	**t**	**LL 95% CI**	**UL 95% CI**	
EN → BE → PI	0.5708	12.5352	1.3930	7.9321	1.9578	19.34	1.0472	9.29	0.4811	0.6605	Supported
e-WOM → BE → PI	0.6060	11.6181	1.3839	7.2991	1.7517	8.32	1.016	1.7571	0.2594	0.4589	Partial Supported
TR → BE → PI	0.7550	13.2387	0.8688	5.0967	1.4162	15.53	0.5163	11.5458	0.4283	0.6043	Supported

Source: Calculations based on the sample using PROCESS v4.2 by Andrew F. Hayes

Note: IV = independent variable, DV = dependent variable, M = mediator, **β** = coefficient, **t** = t-statistic, LL 95% CI and UL 95% CI = lower and upper limits of the 95% confidence, *** p < 0.001; ** p < 0.05.

Based on the analysis from Table 5 using the PROCESS v4.2 macro, the bootstrapping method was applied to assess the mediation of brand engagement in the relationship between entertainment (EN), e-WOM, trendiness (TR) and purchase intention (PI). With 5,000 bootstrap resamples, confidence intervals for the indirect effects of entertainment (LLCI 0.4811, ULCI 0.6605), trendiness (LLCI 0.4283, ULCI 0.6043) on purchase intention do not include zero, indicating that these indirect effects are statistically significant at $p < 0.001$.

However, the indirect effect of e-WOM on purchase intention via brand engagement is significant (LLCI = 0.2594, ULCI = 0.4589) as zero is not contained within the interval. Since the direct effect remains significant, partial mediation is supported.

V. DISCUSSION AND CONCLUSIONS

5.1 DISCUSSION

This study examined the effects of social media entertainment, electronic word-of-mouth, and trendiness on fashion consumers purchase intention with brand engagement acting as a mediating mechanism, grounded in the Stimulus–Organism–Response (S–O–R) framework.

The findings indicate that all three stimuli—entertainment, e-WOM, and trendiness—positively influence both brand engagement and purchase intention. Among them, trendiness had the strongest effect on brand engagement ($\beta = 0.755$) and purchase intention ($\beta = 0.671$), highlighting that up-to-date, fashionable, and socially relevant content strongly drives consumers' behavioral intentions. Entertainment also positively affected brand engagement ($\beta = 0.571$) and purchase intention ($\beta = 0.454$), demonstrating that enjoyable and emotionally engaging content enhances consumer interaction and buying motivation. Similarly, e-WOM significantly influenced brand engagement ($\beta = 0.606$) and purchase intention ($\beta = 0.495$), confirming that peer opinions and online reviews provide crucial informational cues that reduce uncertainty and build consumer confidence.

Brand engagement, as the organism, emerged as the strongest direct predictor of purchase intention ($\beta = 0.833$), supporting the S–O–R framework. Social media stimuli (S) influence internal psychological states (O), which in turn drive behavioral responses (R). Mediation analysis revealed that brand engagement significantly mediates the effects of entertainment and trendiness on purchase intention, while partial mediate the relationship between e-WOM and purchase intention. This suggests that emotion-driven stimuli (entertainment, trendiness) operate through affective engagement, whereas e-WOM functions primarily as an informational and trust-building mechanism.

5.2 THEORETICAL CONTRIBUTIONS

This study contributes to the literature by integrating entertainment, e-WOM, and trendiness into a unified S–O–R framework in the fashion context. It clarifies that social media stimuli operate through different psychological pathways. The research also offers empirical evidence from Bangladesh, enriching social media marketing literature in emerging markets. Additionally, it distinguishes between emotion-driven stimuli–entertainment, trendiness and cognition-driven stimuli– e-WOM advancing theoretical understanding in marketing.

5.3 MANAGERIAL IMPLICATIONS

For fashion brands on social media, several strategies are essential to drive engagement and sales. First, brands should prioritize trend-driven content, as trendiness has the strongest impact on consumer behavior. Regularly updating content to align with current fashion trends will keep the brand relevant. Additionally, investing in entertaining content such as creative storytelling, reels, interactive posts, and influencer collaborations can significantly boost engagement and motivate purchases. Managing e-WOM is also critical, as it directly influences purchase intentions. Encouraging positive reviews, monitoring negative feedback, and developing robust reputation management systems will help maintain a positive brand image. Finally, brands should focus on engagement strategies, as active brand engagement strongly predicts purchase intentions. Encouraging comments, building community interactions, and utilizing interactive tools like polls, Q&A, and live sessions can help foster deeper connections with consumers.

5.4 CONCLUSION

This study confirms that social media marketing elements significantly influence fashion consumers' purchase intention. Trendiness emerges as the most influential stimulus, followed by e-WOM and entertainment. Brand engagement plays a crucial mediating role, particularly for entertainment and trendiness.

By applying the S–O–R framework, this research provides a comprehensive explanation of how social media stimuli translate into consumer purchase intention. The findings highlight the psychological importance of engagement and demonstrate that different marketing stimuli operate through distinct cognitive and affective pathways.

Overall, the study reinforces the strategic importance of integrated social media marketing in shaping fashion consumption behavior in emerging digital markets.

VI. LIMITATION AND FUTURE RESEARCH

6.1 LIMITATIONS

Despite its contributions, the study has several limitations.

1. Data were collected at a single point in time, limiting causal inference. Consumer perceptions and intentions may change over time.
2. In terms of gender distribution, the sample showed a moderate skew toward male respondents.
3. Convenience sampling restricts generalizability, as the sample may not represent the broader population of Bangladeshi fashion consumers.
4. Cultural and economic factors in other markets may influence responses differently.
5. The study measured purchase intention rather than actual behavior, which may not always align with real purchases.
6. Only brand engagement was examined; other psychological mechanisms like brand trust, perceived value, or emotional attachment were not included.

6.2 FUTURE RESEARCH DIRECTIONS

Future research can build upon this study in several important ways.

1. Track social media engagement and purchase behavior over time to assess causal relationships.
2. Explore cultural moderation by comparing Bangladesh with other emerging or developed markets, such as China–Bangladesh comparisons.
3. Include variables like brand trust, perceived value, emotional attachment, or consumer-brand identification to deepen understanding.
4. Examine gender, social media usage intensity, fashion involvement, or influencer credibility to capture nuanced consumer responses.
5. Use real purchase data to complement self-reported intentions and better assess behavioral outcomes.

REFERENCES

[1] Abdelsalam, S., Salim, N., Alias, R. A., Husain, O., Salih, S. H., Thurasamy, R., Hamzah, M., Hamdan, M., & Shehzad, H. M. F. (2024). Using Theory Integration to Explain Online Impulse Buying Behavior in Social Commerce. *Ieee Access*, *12*, 32033-32052. https://doi.org/10.1109/access.2024.3363024

[2] Alfraihat, S. F. A., Ali, A. M., Hodaifa, G., & Alghizzawi, M. (2025). The Impact of Digital Content Marketing on Brand Defence: The Mediating Role of Behavioural Engagement and Brand Attachment. *Administrative Sciences*, *15*(4), 19, Article 124. https://doi.org/10.3390/admsci15040124

[3] Anas, A. M., Abdou, A. H., Hassan, T. H., Alrefae, W. M. M., Daradkeh, F. M., El-Amin, M., Kegour, A. B. A., & Alboray, H. M. M. (2023). Satisfaction on the Driving Seat: Exploring the Influence of Social Media Marketing Activities on Followers' Purchase Intention in the Restaurant Industry Context. *Sustainability*, *15*(9), 21, Article 7207. https://doi.org/10.3390/su15097207

[4] Andonopoulos, V., Lee, J., & Mathies, C. (2023). Authentic isn't always best: When inauthentic social media influencers induce positive consumer purchase intention through inspiration. *Journal of Retailing and Consumer Services*, *75*, 10, Article 103521. https://doi.org/10.1016/j.jretconser.2023.103521

[5] Antczak, B. (2024). The influence of digital marketing and social media marketing on consumer buying behavior. *Journal of Modern Science*, *56*, 310-335. https://doi.org/10.13166/jms/189429

[6] Appel, G., Grewal, L., Hadi, R., & Stephen, A. T. (2020). The future of social media in marketing. *Journal of the Academy of Marketing Science*, *48*(1), 79-95. https://doi.org/10.1007/s11747-019-00695-1

[7] Asmirani, S., & Islamiah, F. (2025). INTEGRATING SOCIAL MEDIA AND CONSUMER BEHAVIOR: AN ANALYSIS OF THE EFFECTS OF CONTENT, INFLUENCER CREDIBILITY, AND E-WOM ON PURCHASE INTENTION THROUGH BRAND ENGAGEMENT. *Jurnal Ekonomi Ichsan Sidenreng Rappang*, *4*(2), 266-275. https://doi.org/10.61912/jeinsa.v4i2.270

[8] Aziz, M. A., Ahmed, M. A., Khan, S. A., Iftikhar, A., & Pervaiz, S. (2025). Customer Brand Engagement and Purchase Intention: The Mediation Effect of Brand Trust and Consumer Brand Identification on the Fashion Apparel Industry of Pakistan. *Regional Lens*, *4*(3), 182-197. https://doi.org/10.55737/rl.2025.43117

[9] Banjongprasert, J. (2024). Online social enterprise customer behaviour: influences of e-commerce, social media, and altruism on online impulsive buying. *Cogent Business & Management*, *11*(1), 20, Article 2370423. https://doi.org/10.1080/23311975.2024.2370423

[10] Bilal, M., Jianqiu, Z., Dukhaykh, S., Fan, M., & Trunk, A. (2021). Understanding the Effects of eWOM Antecedents on Online Purchase Intention in China. *Information*, *12*(5), 192. https://www.mdpi.com/2078-2489/12/5/192

[11] Bilal M, J. Z., Ming J. (2021). How Consumer Brand Engagement Effect on Purchase Intention? The Role of Social Media Elements [Article]. *Journal of Business Strategy Finance and Management*, *4*(7), 44-55. https://doi.org/10.12944/jbsfm.02.01-02.06

[12] Bogdan, A., Dospinescu, N., & Dospinescu, O. (2025). Beyond Credibility: Understanding the Mediators Between Electronic Word-of-Mouth and Purchase Intention.

[13] Bommawar, R., & Tiwari, C. D. (2022). Social Media Marketing Strategies and Their Effects on Consumer Engagement and Buying Behavior in the Fashion Industry. *Innovative Research Thoughts*, *8*(1), 174-180. https://doi.org/10.36676/irt.v8.i1.1431

[14] Bonilla-Quijada, M., Olmo-Arriaga, J. L. D., Adreu Domingo, D., & Ripoll-i-Alcon, J. (2024). Fast fashion consumer engagement on Instagram: a case study.

Cogent Business & Management, *11*(1), 2322111. https://doi.org/10.1080/23311975.2024.2322111

[15] Bui, C. T., Ngo, T. T. A., Chau, H. K. L., & Tran, N. P. N. (2025). How perceived eWOM in visual form influences online purchase intention on social media: A research based on the SOR theory. *PLOS ONE*, *20*(7), e0328093. https://doi.org/10.1371/journal.pone.0328093

[16] Chatterjee, D., Pati, S., Dhaigude, A. S., & Kamath, G. B. (2025). Examining the acceptance of over-the-top services among young consumers during pandemic: a multi-theory approach. *Cogent Business & Management*, *12*(1), 16, Article 2439544. https://doi.org/10.1080/23311975.2024.2439544

[17] Cheung, C. M. K., & Thadani, D. R. (2012). The impact of electronic word-of-mouth communication: A literature analysis and integrative model. *Decision Support Systems*, *54*(1), 461-470. https://doi.org/https://doi.org/10.1016/j.dss.2012.06.008

[18] Cheung, M. L., Pires, G. D., Rosenberger, P. J., & De Oliveira, M. J. (2021). Driving COBRAs: the power of social media marketing. *Marketing Intelligence & Planning*, *39*(3), 361-376. https://doi.org/10.1108/mip-11-2019-0583

[19] Chia-Jo, C., Chiang, I. P., Kuen-Hung, T., & Yi-Hsin, T. (2023). Exploring the Effects of Personalized Advertising on Social Network Sites. *Journal of Social Media Marketing*, *1*(2), 38-54. https://doi.org/10.33422/jsmm.v1i2.1051

[20] Cho, E., & Son, J. (2019). The effect of social connectedness on consumer adoption of social commerce in apparel shopping. *Fashion and Textiles*, *6*(1), 14. https://doi.org/10.1186/s40691-019-0171-7

[21] Dwivedi, Y. K., Ismagilova, E., Hughes, D. L., Carlson, J., Filieri, R., Jacobson, J., Jain, V., Karjaluoto, H., Kefi, H., Krishen, A. S., Kumar, V., Rahman, M. M., Raman, R., Rauschnabel, P. A., Rowley, J., Salo, J., Tran, G. A., & Wang, Y. C. (2021). Setting the future of digital and social media marketing research: Perspectives and research propositions. *International Journal of Information Management*, *59*, 37, Article 102168. https://doi.org/10.1016/j.ijinfomgt.2020.102168

[22] Ebrahimi, P., Basirat, M., Yousefi, A., Nekmahmud, M., Gholampour, A., & Fekete-Farkas, M. (2022). Social Networks Marketing and Consumer Purchase Behavior: The Combination of SEM and Unsupervised Machine Learning Approaches. *Big Data and Cognitive Computing*, *6*(2), 35. https://doi.org/10.3390/bdcc6020035

[23] El-Shihy, D., & Awaad, S. (2025). Leveraging social media for sustainable fashion: how brand and user-generated content influence Gen Z's purchase intentions. *Future Business Journal*, *11*(1), 113. https://doi.org/10.1186/s43093-025-00529-3

[24] Erkan, I., & Evans, C. (2018). Social media or shopping websites? The influence of eWOM on consumers' online purchase intentions. *Journal of Marketing Communications*, *24*(6), 617-632. https://doi.org/10.1080/13527266.2016.1184706

[25] Febyola, A., & Widyanesti, S. (2024). The influence of social media usage and electronic word-of-mouth (eWOM) on purchase intention for local fashion products on Tiktok social media. *Keynesia : International Journal of Economy and Business*, *3*, 94-103. https://doi.org/10.55904/keynesia.v3i2.1237

[26] Felix, R., Rauschnabel, P. A., & Hinsch, C. (2017). Elements of strategic social media marketing: A holistic framework. *Journal of Business Research*, *70*, 118-126. https://doi.org/10.1016/j.jbusres.2016.05.001

[27] Fetais, A. H., Algharabat, R. S., Aljafari, A., & Rana, N. P. (2023). Do Social Media Marketing Activities Improve Brand Loyalty? An Empirical Study on Luxury Fashion Brands. *Information Systems Frontiers*, *25*(2), 795-817. https://doi.org/10.1007/s10796-022-10264-7

[28] Filieri, R. (2015). What makes online reviews helpful? A diagnosticity-adoption framework to explain informational and normative influences in e-WOM. *Journal of Business Research*, *68*(6), 1261-1270. https://doi.org/https://doi.org/10.1016/j.jbusres.2014.11.006

[29] Garg, M., & Bakshi, A. (2024). Exploring the impact of beauty vloggers' credible attributes, parasocial interaction, and trust on consumer purchase intention in influencer marketing. *Humanities & Social Sciences Communications*, *11*(1), 14, Article 235. https://doi.org/10.1057/s41599-024-02760-9

[30] George, A., Shibu, M., Joseph, E. T., & Sunny, P. (2025). Impact of social media influencer marketing on customer purchase intention in the fashion industry: a systematic literature review [Systematic Review]. *Frontiers in Communication*, *Volume 10 - 2025*. https://doi.org/10.3389/fcomm.2025.1676901

[31] Hollebeek, L. (2011). Exploring customer brand engagement: Definition and themes. *Journal of Strategic Marketing*, *19*. https://doi.org/10.1080/0965254X.2011.599493

[32] Hu, S., & Zhu, Z. (2022). Effects of Social Media Usage on Consumers' Purchase Intention in Social Commerce: A Cross-Cultural Empirical Analysis [Original Research]. *Frontiers in Psychology*, *Volume 13 - 2022*. https://doi.org/10.3389/fpsyg.2022.837752

[33] Huang, M., Saleh, M. S. M., & Zolkepli, I. A. (2024). The moderating effect of environmental gamification on the relationship between social media marketing and consumer-brand engagement: A case study of Ant Forest Gen Z users. *Heliyon*, *10*(4), 15, Article e25948. https://doi.org/10.1016/j.heliyon.2024.e25948

[34] Huang, Y., Bunchapattanasakda, C., Suo, L., & Boonmek, B. (2024). THE INFLUENCE OF SOCIAL MEDIA MARKETING ON PURCHASE INTENTIONS THROUGH CONSUMER ENGAGEMENT. *Asian Administration and Management Review*, *7*(2), 45-55. https://doi.org/10.14456/aamr.2024.21

[35] Ibrahim, B., Aljarah, A., & Ababneh, B. (2020). Do Social Media Marketing Activities Enhance Consumer Perception of Brands? A Meta-Analytic Examination. *Journal of Promotion Management*, *26*, 1-25. https://doi.org/10.1080/10496491.2020.1719956

[36] Ismael, A. S., Bin Amin, M., Ali, M. J., Hajdu, Z., & Peter, B. (2025). Relationship between social media marketing and young customers' purchase intention towards online shopping. *Cogent Social Sciences*, *11*(1), 16, Article 2459881. https://doi.org/10.1080/23311886.2025.2459881

[37] Ismagilova, E., Slade, E. L., Rana, N. P., & Dwivedi, Y. K. (2020). The Effect of Electronic Word of Mouth Communications on Intention to Buy: A Meta-Analysis. *Information Systems Frontiers*, *22*(5), 1203-1226. https://doi.org/10.1007/s10796-019-09924-y

[38] John, J. K., Kilumile, J. W., Makorere, R., Mrisha, S. H., Nyagawa, M., & Hussein, M. M. (2025). From business-to-consumer interactions to brand equity: driving social commerce purchase intentions. *Cogent Business & Management*, *12*(1), 16, Article 2494064. https://doi.org/10.1080/23311975.2025.2494064

[39] Kaplan, A. M., & Haenlein, M. (2010). Users of the world, unite! The challenges and opportunities of Social Media. *Business Horizons*, *53*(1), 59-68. https://doi.org/https://doi.org/10.1016/j.bushor.2009.09.003

[40] Kethuda, O., & Ayoubi, R. (2025). Perceived Market Leadership and Customer Engagement for IT Companies in the Enterprise Software Market: Evaluating the Role of Social Media Marketing [; Early Access]. *Journal of Business-to-Business Marketing*, 20. https://doi.org/10.1080/1051712x.2024.2446812

[41] Khraiwish, A., & Alsharif, A. H. (2024). Insights and Influencers: A Decade of Social Media Marketing Research Revealed Through Bibliometrics. *Scientific Annals of Economics and Business*, *71*(4), 497-518. https://doi.org/10.47743/saeb-2024-0023

[42] Kian Yeik, K., Ong, D., Khoo, K. L., & Yeoh, H. J. (2021). Perceived Social Media Marketing Activities and Consumer-Based Brand Equity: Testing a Moderated Mediation Model. *Asia Pacific Journal of Marketing and Logistics*, *33*, 53-72. https://doi.org/10.1108/APJML-07-2019-0453

[43] Kim, S., Kandampully, J., & Bilgihan, A. (2018). The influence of eWOM communications: An application of online social network framework. *Computers in Human Behavior*, *80*, 243-254. https://doi.org/https://doi.org/10.1016/j.chb.2017.11.015

[44] Lee, H. (2024). Interest-Based E-Commerce and Users' Purchase Intention on Social Network Platforms. *Ieee Access*, *12*, 87451-87466. https://doi.org/10.1109/access.2024.3417440

[45] Leong, C.-M., Loi, A. M.-W., & Woon, S. (2022). The influence of social media eWOM information on purchase intention. *Journal of Marketing Analytics*, *10*(2), 145-157. https://doi.org/10.1057/s41270-021-00132-9

[46] Li, X., Huang, D., Dong, G., & Wang, B. (2024). Why consumers have impulsive purchase behavior in live streaming: the role of the streamer. *BMC Psychology*, *12*(1), 129. https://doi.org/10.1186/s40359-024-01632-w

[47] Lin, B., & Shen, B. (2023). Study of Consumers' Purchase Intentions on Community E-commerce Platform with the SOR Model: A Case Study of China's "Xiaohongshu" App. *Behavioral Sciences*, *13*(2), 103. https://www.mdpi.com/2076-328X/13/2/103

[48] Lin, X., Al Mamun, A., Masukujjaman, M., & Yang, Q. (2024). Unveiling the effect of social media marketing activities on logistics brand equity and reuse intention. *Humanities and Social Sciences Communications*, *11*(1), 1474. https://doi.org/10.1057/s41599-024-04022-0

[49] Luo, C., Hasan, N. A. M., Zamri bin Ahmad, A. M. t., & Lei, G. (2025). Influence of short video content on consumers purchase intentions on social media platforms with trust as a mediator. *Scientific Reports*, *15*(1), 16605. https://doi.org/10.1038/s41598-025-94994-z

[50] Mehrabian, A., & Russell, J. A. (1974). *An approach to environmental psychology*. MIT Press. https://archive.org/details/approachtoenviro00albe

[51] Moghddam, H. A., Ahmadi, H., & Barari, M. (2025). Decoding online brand-related activities: unveiling motivations, experiences, and personality factors in social commerce [; Early Access]. *Electronic Commerce Research*, 33. https://doi.org/10.1007/s10660-024-09946-y

[52] Muturi, H. (2024). Impact of Social Media on Fashion Trends and Consumer Behavior in Kenya. *International Journal of Fashion and Design*, *3*, 24-36. https://doi.org/10.47604/ijfd.2386

[53] Nabivi, E. (2025). The Role of Social Media in Green Marketing: How Eco-Friendly Content Influences Brand Attitude and Consumer Engagement. *Sustainability*, *17*(5), 22, Article 1965. https://doi.org/10.3390/su17051965

[54] Ngo, T. T. A., An, G. K., Dao, D. K., Nguyen, N. Q. N., Phong, B. H., Nguyen, N. Y. V., & Nguyen, T. B. N. (2025). Leveraging social media marketing activities (SMMAs) to enhance consumer satisfaction and purchase intention for bio-cosmetics. *Acta Psychologica*, *261*, Article 105768. https://doi.org/10.1016/j.actpsy.2025.105768

[55] Ngo, T. T. A., Long, V. B., Dien, L. M., Trung, N. T., My, T. M., & and Nguyen, Q. K. (2024). The impact of eWOM information in social media on the online purchase intention of Generation Z. *Cogent Business & Management*, *11*(1), 2316933. https://doi.org/10.1080/23311975.2024.2316933

[56] Nguyen, C., Tran, T., & Nguyen, T. (2024). FACTORS AFFECTING USERS' BRAND AWARENESS THROUGH SOCIAL MEDIA MARKETING ON TIKTOK. *Innovative Marketing*, *20*(1), 11. https://doi.org/10.21511/im.20(1).2024.11

[57] Ningrum, M. H., & Susila, I. (2025). Pengaruh Social Experience, Trendiness dan E-WOM terhadap Purchase Intention Melalui Brand Awarness Sebagai Mediasi pada Social Media Marketing Produk Kecantikan di Socialla. *Al-Kharaj: Jurnal Ekonomi, Keuangan & Bisnis Syariah*, *7*(1), 1359 – 1379. https://doi.org/10.47467/alkharaj.v7i1.6920

[58] Ntousi, E., Lazaris, C., Katiaj, P., & Koukopoulos, A. (2025). Directed Consumer-Generated Content (DCGC) for Social Media Marketing: Analyzing Performance Metrics from a Field Experiment in the Publishing Industry. *Systems*, *13*(2), 20, Article 124. https://doi.org/10.3390/systems13020124

[59] Omeish, F., Alrousan, M., Alghizzawi, M., Aqqad, A., & Daboub, R. (2024). Social media marketing elements, purchase intentions, and cultural moderators in fast fashion: Evidence from Jordan, Morocco, and Spain. *International Journal of Data and Network Science*, *8*, 1613-1624. https://doi.org/10.5267/j.ijdns.2024.3.005

[60] Pan, M. Z., Blut, M., Ghiassaleh, A., & Lee, Z. W. Y. (2025). Influencer marketing effectiveness: A meta-analytic review [Review]. *Journal of the Academy of Marketing Science*, *53*(1), 52-78. https://doi.org/10.1007/s11747-024-01052-7

[61] Park, J.-S., & Ha, S. (2021). From information experiences to consumer engagement on brand's social media accounts. *Fashion and Textiles*, *8*(1), 21. https://doi.org/10.1186/s40691-021-00246-9

[62] Pick, M. (2021). Psychological ownership in social media influencer marketing. *European Business Review*, *33*(1), 9-30. https://doi.org/10.1108/ebr-08-2019-0165

[63] Putri, V. R., Rahim, H., Rasool, M. S. A., Zakaria, N. B., & Irpan, H. M. (2023). TRUSTWORTHINESS, EXPERTISE AND LIKEABILITY TOWARDS HALAL PURCHASING BEHAVIOUR: DOES ATTITUDE MATTER? *Journal of Nusantara Studies-Jonus*, *8*(3), 26-42. https://doi.org/10.24200/jonus.vol8iss3pp26-42

[64] Rahaman, M. A., Hassan, H. M. K., Asheq, A. A., & Islam, K. M. A. (2022). The interplay between eWOM information and purchase intention on social media: Through the lens of IAM and TAM theory. *PLOS ONE*, *17*(9), e0272926. https://doi.org/10.1371/journal.pone.0272926

[65] Sherief, A. R., Tarofder, A. K., Ibrahim, A. M., Sabir, R. I., Ahmad, M., & Rahman, A. U. (2025). Bibliometric analysis of social media persuasiveness and influence: a comprehensive review from 2010 to 2023. *Cogent Business & Management*, *12*(1), 19, Article 2449247. https://doi.org/10.1080/23311975.2024.2449247

[66] Taher, A. (2022). *"Influence of online marketing on SME start-ups; A study on Bangladesh Perspective" ii | Page*

[67] Thanasi-Boçe, M., Zeqiri, J., & Kurtishi-Kastrati, S. (2022). The Role of Social Media Usage and Engagement on Purchase Intentions for Fashion Brands. *International Journal of E-Services and Mobile Applications*, *14*(1). https://doi.org/https://doi.org/10.4018/IJESMA.300269

[68] Utami, N. R., & Astuti, R. D. (2024). Prioritizing social media marketing activities: unveiling the SMMA dimensions for enhancing brand attitude, experience, and purchase intention. *International Journal of Research in Business and Social Science (2147- 4478)*, *13*(5), 58-71. https://doi.org/10.20525/ijrbs.v13i5.3465

[69] van Deventer, M., & Saraiva, M. (2025). Antecedents of Generation Y consumers' perceived value of social media advertisements. *Cogent Social Sciences*, *11*(1), 15, Article 2450097. https://doi.org/10.1080/23311886.2025.2450097

[70] Vieira, V. A. (2013). Stimuli–organism-response framework: A meta-analytic review in the store environment. *Journal of Business Research*, *66*(9), 1420-1426. https://doi.org/https://doi.org/10.1016/j.jbusres.2012.05.009

[71] Wang, F., Wang, K., Han, Y., & Cho, J. H. (2024). Influences of design-driven FMCG on consumers' purchase intentions: A test of S-O-R model. *Humanities and Social Sciences Communications*, *11*(1), 852. https://doi.org/10.1057/s41599-024-03362-1

[72] Wilopo, W., & Nuralam, I. P. (2025). An investigating the influence of social media marketing activities on revisit intention among Indonesian international tourists. *Cogent Business & Management*, *12*(1), 20, Article 2440626. https://doi.org/10.1080/23311975.2024.2440626

[73] Xu, W. (2025). Research on the Influence of Digital Marketing on Consumer Behavior in the Fashion Industry. *Advances in Economics, Management and Political Sciences*, *181*, 161-166. https://doi.org/10.54254/2754-1169/2025.23250

[74] Xue, Z., Li, Q., & Zeng, X. (2023). Social media user behavior analysis applied to the fashion and apparel industry in the big data era. *Journal of Retailing and Consumer Services*, *72*, 103299. https://doi.org/https://doi.org/10.1016/j.jretconser.2023.103299

[75] Yadav, M., & Rahman, Z. (2018). The Influence of Social Media Marketing Activities on Customer Loyalty: A Study of E-commerce Industry. *Benchmarking An International Journal*, *25*, 3882-3905. https://doi.org/10.1108/BIJ-05-2017-0092

[76] Ying, N., Ab-Rahim, R., & Mohd Kamal, K. (2021). Impact of Social Media on Consumer Purchasing Behaviour in Sarawak. *International Journal of Academic Research in Business and Social Sciences*, *11*. https://doi.org/10.6007/IJARBSS/v11-i5/9935

[77] Zahra, T. (2025). The influence of social media marketing on consumer brand engagement and brand knowledge in fast food products [social media marketing; consumer brand engagement; brand knowledge; fast food]. *2025*, *24*(1), 15. https://doi.org/10.24123/mabis.v24i1.844

[78] Zahrah, N., Sengorou, M. F. R. J. A., & Salleh, N. S. M. (2024). The Impact of User-Generated Content and Electronic Word-of-Mouth on Consumer Purchase Intention: Consumer Engagement as a Mediator. *International Journal of Academic Research in Business and Social Sciences*, *14*(7), 2159–2174. https://doi.org/http://dx.doi.org/10.6007/IJARBSS/v14-i7/21981

[79] Zaki, K., Alhomaid, A., & Shared, H. (2025). Leveraging Machine Learning to Analyze Influencer Credibility's Impact on Brand Admiration and

Consumer Purchase Intent in Social Media Marketing. *Human Behavior and Emerging Technologies*, *2025*(1), 15, Article 9959697. https://doi.org/10.1155/hbe2/9959697

[80] Zhang, P. L., Chao, C. W., Chiong, R., Hasan, N., Aljaroodi, H. M., & Tian, F. (2023). Effects of in-store live stream on consumers' offline purchase intention. *Journal of Retailing and Consumer Services*, *72*, 12, Article 103262. https://doi.org/10.1016/j.jretconser.2023.103262

International Journal of Advanced Engineering Research and Science (IJAERS)
Peer-Reviewed Journal
ISSN: 2349-6495(P) | 2456-1908(O)
Vol-13, Issue-3; Mar, 2026
Journal Home Page Available: https://ijaers.com/
Article DOI: https://dx.doi.org/10.22161/ijaers.133.2

Simulation and Optimization of Satellite Re-Entry Trajectories Using MATLAB

Mohamed Shuaib.A[1*], Dr. S. Charulatha[2]

[1]Student, Department of Aerospace, Hindustan Institute of Technology and Science, Chennai, Tamilnadu, India
ORCID ID: 0004 0038 3459
[2]Professor, Department of Aerospace, Hindustan Institute of Technology and Science, Chennai, Tamilnadu, India
*Corresponding Author

Received: 28 Jan 2026,

Received in revised form: 25 Feb 2026,

Accepted: 02 Mar 2026,

Available online: 17 Mar 2026

***Keywords*— Satellite re-entry, MATLAB simulation, flight path angle, re-entry trajectory, Atmospheric drag, Differential equations, orbital dynamics, altitude-varying air density.**

***Abstract*—** *This paper presents a simulation-focused methodology for performing satellite re-entry dynamics analysis with MATLAB. When a satellite is descending, it is subjected to gravitational attraction, atmospheric drag and applied thrust; these factors can be described by solving a system of differential equations. The simulation is initiated at an altitude of 300 km with the given initial conditions and with the use of real-world properties such as altitude-varying air density and orbital dynamics. The simulations give an altitude decay, velocity change and flight path angle history of re-entry. In addition, this model illustrates that atmospheric resistance becomes the dominant force of deceleration at low altitudes.*

I. INTRODUCTION

With the increasing number of space debris in near earth orbit due to the presence of artificial satellites, a reliable post mission disposal technique has emerged. Atmospheric re-entry – a process involving massive aerodynamic heating, supersonic deceleration and pinpoint trajectory guidance – is one of the most extreme environmental conditions a satellite can endure during its life-span. Regardless of whether satellite re-entry is intentional or accidental, careful consideration is required to assure both safety and successful mission and to satisfy international guidelines about space debris mitigation.

Re-entry evolution is controlled by a variety of competing physical forces, such as gravitational pull, aerodynamic drag, and, in some cases, engine thrust. These will shift the satellite's speed, height and orientation as it falls. The system of nonlinear ordinary differential equations describing such interactions under realistic atmospheric conditions needs to be solved in order to predict and optimize the re-entry trajectory.

This paper describes a MATLAB-based simulation approach to satellite re-entry analysis. The model considers the atmospheric density variation with altitude, the gravitational force depending on the altitude and it is postulated a constant thrust. The initial conditions are taken at the satellite position of 300 km and then the satellite velocity, altitude and path angle are calculated as the satellite re- entry in the atmosphere. The results of the simulation show the forces dominating the structure at different stages of descent, and indicate design guide lines for the flight trajectories and control.

This paper provides a foundational MATLAB-based simulation framework for analysing satellite re-entry dynamics. It models key forces gravity, drag, and thrust affecting descent. The approach supports trajectory planning, safety assessment, and mission design, and can be

extended for various satellite configurations and advanced scenarios in aerospace engineering research and education.

II. LITERATURE REVIEW

Satellite re-entry is the most critical and dynamic stage of the life of any man-made spacecraft. With adding traffic in low Earth orbit (LEO) and transnational emphasis on space debris mitigation, understanding and bluffing there-entry process has gained significant significance in both academic exploration and aerospace assiduity operations.

Kaplan's early work in orbital mechanics laid a theoretical foundation for studying the motion of satellites, with specific emphasis on the influence of gravity and first-order atmospheric drag during orbital decay and re-entry [1]. His analytic models played a central role in laying the foundation for re-entry analysis. Only that they did not cover more complex effects of dynamic atmospheric variations and dynamic controlling functions flying a crucial role during the re-entry process or during the re-entry phase. Braun and Manning [2] contributed significantly to the field of re-entry modelling by integrating high-resolution atmospheric data with advanced guidance algorithms tailored for entry vehicles. Their study provided valuable insights into the challenges of vehicle control during atmospheric re-entry, particularly for missions targeting planets such as Earth and Mars. They underscored the importance of accurate simulation environments capable of accounting for variations in atmospheric density, thermal loads, and trajectory control mechanisms.

Cook [3] added to knowledge of Aerodynamic drag by proposing rational models for the computation of Satellite drag areas before various atmospheric and flux conditions. His results provide the foundation of many of today's drag models employed to predict decays and re-entry times. At lower mound, the drag as well as the exobase are even more important as the increase of atmospheric density becomes even more exponential.

For small satellites and CubeSats, Leipold et al. [4] have suggested active as well as non-resistant de-orbiting techniques to facilitate controlled re-entry. They studied drag addition bias such as sails and tethers which might augment face area, and thus atmospheric drag and also hasten de-orbit. This method is especially effective for low-delta V, low-cost missions with little to no on-board propulsion.

Pardini and Anselmo [5] conducted a statistical analysis of derelict satellite re-entries and long-term orbital decay under the influence of solar activity cycles. Their research demonstrated that even minor atmospheric variations, driven by changes in solar flux and geomagnetic indices, can significantly alter re-entry timelines. The study emphasized the importance of adaptable models that incorporate both environmental variability and object-specific characteristics.

Schaub and Junkins [6] created logical mechanics and optimization techniques for satellite line control with special treatment of descent and re-entry. Their procedure has been widely adopted for determining optimization de-orbit burns, re-entry circles, orbital rendezvous and even pushes. The inclusion of thrust modelling means that their approach is particularly appropriate for thrust-supported re-entry analysis.

Recently, the use of MATLAB as a tool for engineering simulation has sky zoomed because of its flexibility and built-in numerical solvers. Mukhopadhyay et al. [7] used MATLAB to simulate ballistic re-entry with simplified force models. Their results were a validation of generalization of MATLAB application in education and early charge development.

Rodriguez-Donaire et al. [8] presented an elementary re-entering satellite model appropriate for educational and research purposes. They focused on implementation simplicity and efficient computation, making it accessible for students and beginners. By balancing accuracy and simplification, the model allowed users to investigate entry dynamics with commonly available simulation tools.

Huang et al. [9] used the Runge-Kutta technique for calculation of the re-entry dynamics of low Earth orbit satellites. They simulated the changing forces and confirmed their results using satellite re-entry data. This latter system, used in our simulation also, is well known for its stability and for the preciseness of its work in ordinary differential equations.

NASA's Debris Assessment Software (DAS) [10] and the European Space Agency's DRAMA suite are sophisticated tools designed to evaluate satellite end-of-life scenarios and associated re-entry risks. These platforms leverage comprehensive environmental data and adhere to global regulatory standards. Nevertheless, their technical depth and professional focus can pose challenges for quick evaluations or academic exploration. In comparison, MATLAB-based simulations—such as the one developed in this work—provide a more accessible and streamlined approach, offering sufficient accuracy for understanding core re-entry mechanics. This makes them particularly useful for instructional settings and early-phase mission analysis.

A recent study by Mohamed Shuaib A. [11] explores the use of MATLAB for simulating satellite deployment dynamics, emphasizing its flexibility and suitability for both academic

and preliminary mission design purposes. The study demonstrates how gravitational, drag, and thrust forces can be integrated into a cohesive simulation framework, making it especially useful for early-stage modelling and educational applications where accessibility and clarity are essential.

In summary, while former studies give robust models and simulation platforms for satellite re-entry, multitudinous of them are also too complex for early- stage operations or not easily customizable. This paper builds upon these being models by introducing a MATLAB- predicated simulation frame that integrates gravitational forces, atmospheric drag, and thrust into a cohesive and adaptable structure suitable for both academic study and primary charge analysis.

III. METHODOLOGY

The approach in this work is to numerically simulate the re-entry of satellite trajectory using the MATLAB software that includes gravitational forces, atmospheric drag, and thrust. The simulation is defined to simulate the equations of motion using reasonable physical values and starting conditions for a LEO-re-entering satellite.

Parameters

Table 1. Physical Parameters Used in Satellite Re-entry Simulation.

Parameter	Symbol	Value	Units
Gravitational constant	G	6.67430×10^{-11}	$m^3\cdot kg^{-1}\cdot s^{-2}$
Earth mass	M	5.972×10^{24}	kg
Earth radius	R_{earth}	6,371,000	m
Sea-level density	ρ_0	1.225	kg/m^3
Scale height	H	8500	m
Drag coefficient	C^d	2.2	dimensionless
Cross-sectional area	A	1	m^2
Satellite mass	m	500	kg
Thrust force	F_{thrust}	1000	N

The physical parameters used for the simulation are summarized in Table 1.

Governing Equations

The satellite's motion is described using three state variables: altitude (h), velocity (v), and flight path angle (γ), satellite mass(m).

The equations of motion are: [22]

$$\frac{dh}{dt} = v \sin\gamma$$

$$\frac{dv}{dt} = \frac{F_{thrust} - D}{m}$$

$$\frac{d\gamma}{dt} = -\frac{g}{v}\cos\gamma$$

equation that includes a control input, such as

$$\frac{d\gamma}{dt} = -\frac{g}{v}\cos\gamma + u(t)$$

where u(t) is a control function (manual or automated).

where the drag force D is:

$$D = \frac{1}{2}\rho(h)v^2 C_d A$$

and gravitational acceleration g varies with altitude as:

$$g = \frac{GM}{(R_{earth}+h)^2}$$

3.3 Atmospheric Density Model

Atmospheric density decreases exponentially with altitude: [23]

$$\rho(h) = \rho_0 \exp\left(-\frac{h}{H}\right)$$

where ρ_0 = 1.225 $kg/m^3$is sea-level atmospheric density and H=8500m is the scale height.

3.4 Numerical Solution

The equations were solved using MATLAB's ode45 solver over a time span of 0 to 2000 seconds. Initial conditions were set as:

Altitude: 300,000 m

Velocity: 7,500 m

Flight path angle: -5° (converted to radians)

A typical initial re-entry flight path angle for low Earth orbit vehicles ranges between –1° and –10°, depending on:

Desired descent rate

Mission profile

Safety margins

Using –5° represents a moderately shallow but safe re-entry trajectory.

Re-Entry Simulation

Simulation Setup

For a practical on-orbit decay simulation, a 2D orbital mechanics model was implemented to analyse the re-entry dynamic motion of a CubeSat. The deorbiting has been solved numerically with an ode45 integrator over a period of time sufficiently long to cover the entire deorbiting process. The satellite was placed in low Earth orbit at an initial circular orbit, and the perturbative forces were added to simulate the real entry.

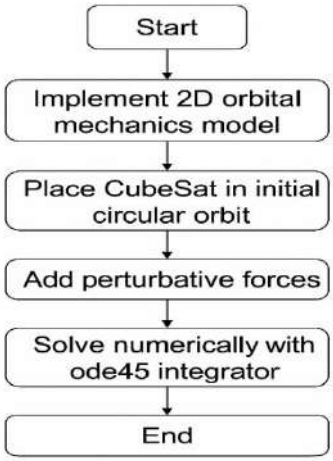

Fig.1. Simulation Workflow for Satellite Re-entry Using 2D Orbital Dynamics.

Simulation Results

The simulation outputs illustrate the variation of key parameters during the satellite re-entry process.

The **altitude profile** shows a gradual decrease from 300 km to the surface of the Earth as atmospheric drag increases with decreasing altitude (figure 2).

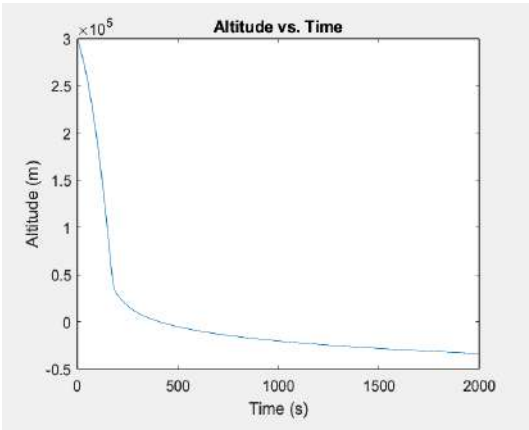

Fig.2. Altitude Profile of a Re-entering Satellite over Time.

The **velocity profile** indicates that the satellite initially maintains a high orbital velocity, which then decreases sharply as aerodynamic drag intensifies in the denser atmosphere (figure 3).

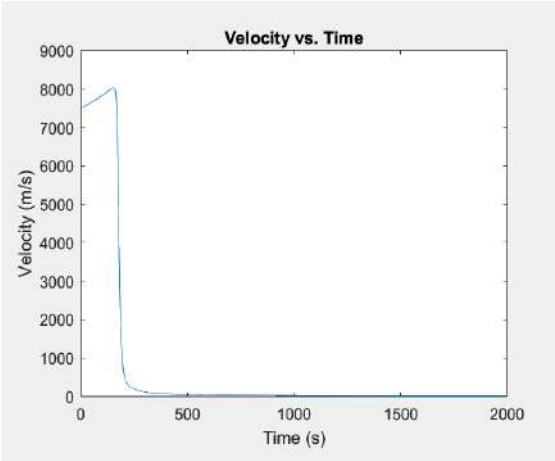

Fig.3. Velocity Profile of a Re-entering Satellite over Time.

The **flight path angle** progressively steepens (becomes more negative) as the satellite descends, reflecting the transition to a near-vertical descent in the later stages (figure 4).

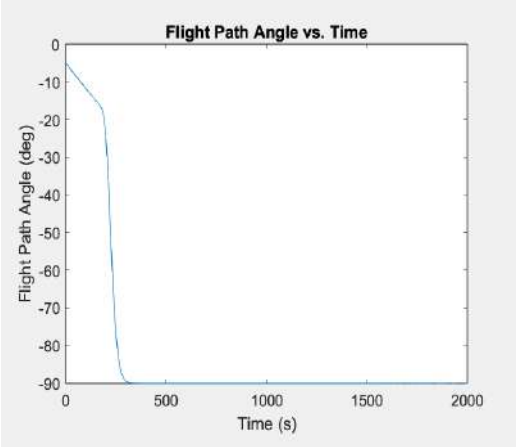

Fig.4. Flight Path Angle Profile of a Re-entering Satellite over Time.

The **drag force** rises significantly at lower altitudes where air density is higher, becoming the dominant decelerating factor (figure 5).

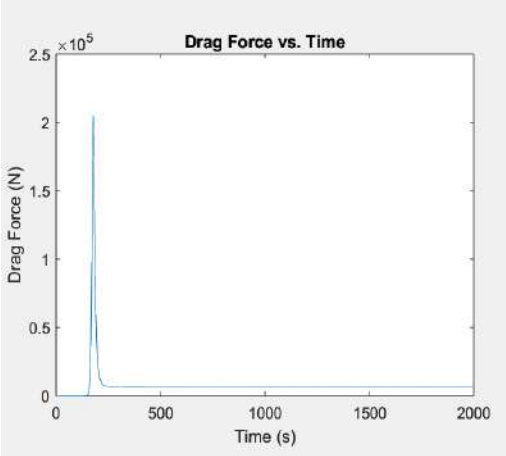

Fig.5. Drag Force Profile of a Re-entering Satellite over Time.

The **gravitational force** remains relatively constant but slightly increases due to the inverse-square law as altitude decreases (figure 6).

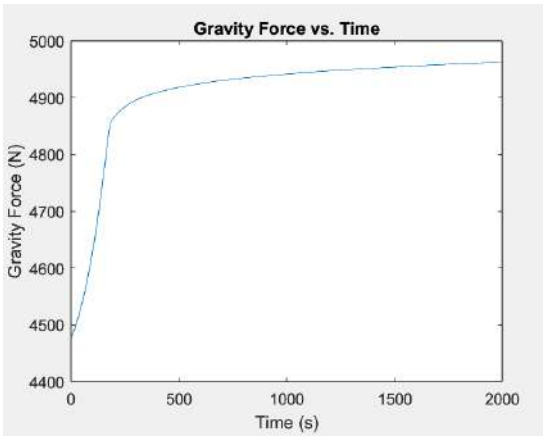

Fig.6. Gravity Force Profile of a Re-entering Satellite over Time.

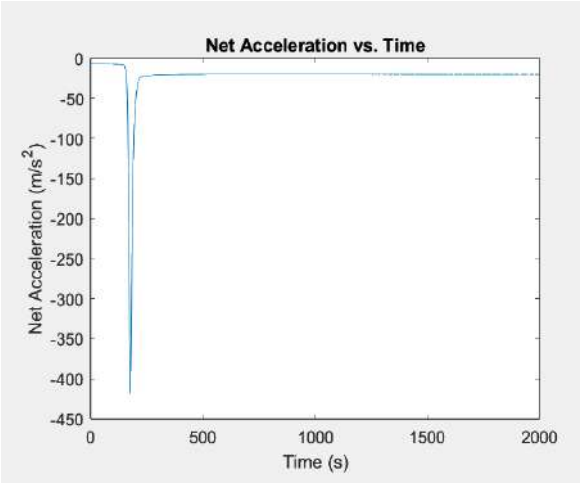

Fig.7. Net Acceleration Profile of a Re-entering Satellite over Time.

The **net acceleration** shows the combined effect of thrust, drag, and gravity, with drag dominating in the terminal phase and resulting in substantial deceleration (figure 7).

IV. RESULT AND DISCUSSION

The simulation was performed using the given initial conditions and physical parameters to the original problem for the satellite's re-entry line over a period of 2000-alternate steps. The key findings and their counter-accusations are batted below

Trajectory Profiles

Altitude: The spacecraft altitude decreases gradually from 300 km to the surface of the earth, representing the re-entry descent phase. The atmospheric viscosity grows exponentially in the direction of lower mound, causing larger aerodynamic drag and rapid altitude drop.

Velocity: The satellite initially maintains a high orbital velocity, which then declines sharply as drag forces intensify in the denser atmosphere. This velocity reduction reflects the conversion of kinetic energy into heat and drags work. (figure 3)

Starting from -5°: the flight path angle gradually steepens (becomes more negative) as the satellite descends, reflecting an increasingly downward trajectory driven by gravitational pull and atmospheric resistance.

5.2 Forces Acting on the Satellite

Drag Force: Drag force increases significantly as the satellite penetrates denser atmospheric layers. The drag peaks at lower altitudes where velocity remains substantial, confirming its critical role in decelerating the spacecraft. (figure 5)

Gravity Force: The gravitational force remains consistently directed toward Earth's centre and slightly intensifies due to the inverse-square dependence on altitude. It continuously contributes to downward acceleration. (figure 6)

Net Acceleration: The net acceleration combines thrust, drag, and gravity effects. While the thrust partially offsets drag and gravity at the start, drag dominates later, resulting in a negative net acceleration and consequent deceleration**.** (figure 7)

Final Re-entry Conditions

At the end of the simulation, the satellite reaches an altitude of approximately **-33,639.09 m**, indicating ground impact or termination beyond the surface reference level due to numerical overshoot. The final velocity is **9.20 m/s**, and the flight path angle reaches **-90.00°**, showing a purely vertical

descent. These values represent the satellite's final state during atmospheric re-entry and ground approach.

The negative final altitude value observed in the simulation, approximately **–33,639.09 m**, results from numerical overshoot in the integration process after the satellite has effectively reached ground level. This overshoot commonly occurs in orbital simulations when the numerical solver continues beyond the physical boundary (Earth's surface) due to step size limitations or lack of termination conditions in the integrator. The final velocity of **9.20 m/s** and the flight path angle of **–90.00°** indicate that the satellite has entered a near-vertical descent phase, consistent with the final stage of atmospheric re-entry where motion becomes predominantly vertical due to strong drag forces and gravitational acceleration. These values effectively represent the satellite's terminal re-entry condition and the conclusion of its descent trajectory within the simulation framework.

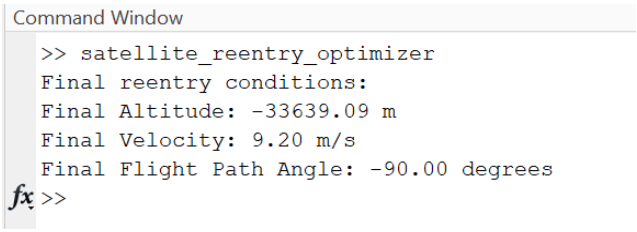

Fig.8. Final Re-entry Conditions.

V. RESULTS DISCUSSION

The results underscore the delicate interplay between thrust and drag in shaping re-entry trajectories. Adequate thrust can moderate deceleration rates, potentially reducing thermal and mechanical stresses experienced by the satellite. Furthermore, controlling the flight path angle is essential for achieving a predictable descent and ensuring mission safety.

Limitations of the current model include the assumptions of constant drag coefficient, neglect of lift and control forces, and simplification to a planar (2D) trajectory. Future improvements could integrate variable aerodynamic coefficients, thermal effects, and three-dimensional dynamics to enhance model accuracy and applicability.

VI. CONCLUSION

A MATLAB simulation has been established in the present paper to further study the re-entry dynamics of a satellite combined with the effect of Earth's gravity, atmospheric drag and thrust added. The model accurately describes the satellite's descent profile, such as substantial altitude decline, deceleration and flight path angle evolution during the descent process.

Numerical simulations point out that atmospheric drag is the paramount factor in decelerating the satellite in the re-entry phase, revealing that even with low thrust levels (threshold value), the thrust can be used to control the trajectory characteristics to optimize such re-entry. Despite model simplifications such as constant drag coefficient and planar motion the framework offers valuable insights for initial mission design and controlled re-entry planning.

Future work should address the model's current limitations by incorporating three-dimensional trajectory dynamics, variable aerodynamic coefficients, thermal heating effects, and active control strategies. Such enhancements will improve prediction accuracy and support safer, more efficient satellite re-entry operations, especially for emerging small satellite platforms.

REFERENCES

[1] Kaplan Melvin 1976 Modern spacecraft dynamics and control New York Wiley

[2] Braun Robert D and Manning Robert M 2007 Mars exploration entry descent and landing challenges. J. Spacecr. Rockets. 44(2): 310–323

[3] Cook G E 1965 Satellite drags coefficients. Planet. Space Sci. 13(10): 929–946

[4] Leipold M, Lingner S, Pabsch A, Seboldt W, Borg E, Herrmann A and Lura F 1999 De-orbiting strategies for satellites using solar sails. Acta Astronaut. 45(4–9): 557–566

[5] Pardini Claudia and Anselmo Luca 2012 Reentry predictions of three massive uncontrolled spacecraft In: Proc. 23rd Int. Symp. Space Flight Dyn. Pasadena CA pp. 14–20

[6] Schaub Hans and Junkins John L 2009 Analytical mechanics of space systems 2nd ed Reston VA AIAA

[7] Mukhopadhyay A, Sinha S and Banerjee R 2014 Simulation of ballistic re-entry trajectories using MATLAB. Int. J. Aerosp. Eng. 2014: 1–10

[8] Rodriguez-Donaire A, Aznar J R and Martinez M A 2020 A low-complexity satellite re-entry model for academic purposes. Acta Astronaut. 170: 1–10

[9] Huang Y, Wang L and Li Z 2019 Application of Runge-Kutta methods in satellite re-entry dynamics simulation. J. Aerosp. Eng. 32(5): 04019080

[10] NASA Orbital Debris Program Office 2008 NASA debris assessment software (DAS) user's guide NASA Tech. Memo. NASA/TM-2008-214779

[11] Shuaib A M 2024 Comprehensive analysis of satellite deployment dynamics using MATLAB. Int. J. Aerosp. Def. Res. 1(1): 29–30

[12] Park R S and Braun R D 2007 Guidance algorithm for precision entry of Mars Science Laboratory. J. Spacecr. Rockets. 44(5): 1108–1117

[13] Klinkrad Holger 2006 Space debris models and risk analysis Berlin Springer-Verlag

[14] Maclay T D and Anderson M J 2002 Propellantless deorbiting using electrodynamic tethers. J. Spacecr. Rockets. 39(2): 205–213

[15] Pardini M, Anselmo L and Drolshagen C M 2015 Satellite reentry predictions using long-term solar activity models. Adv. Space Res. 56(3): 480–493
[16] Patera R 1999 Satellite breakup model for spacecraft reentry. J. Spacecr. Rockets. 36(3): 475–482
[17] Gibbon D W 2002 Reentry and landing performance of reusable space vehicles. Prog. Aerosp. Sci. 38(2): 105–144
[18] Ailor F, Rhatigan J and Peterson S 2010 A technical assessment of orbital debris mitigation options. Acta Astronaut. 66(11–12): 1910–1915
[19] Gill E 2012 Low-cost autonomous satellite de-orbit strategies using drag sails and magnetic torquers. J. Aerosp. Eng. 226(10): 1256–1267
[20] Holzinger M and Jah M 2015 Collision risk estimation for reentry trajectories with atmospheric and object uncertainties. Aerosp. Sci. Technol. 41: 97–109
[21] European Space Agency 2020 DRAMA 3.0 – ESA's debris risk assessment and mitigation analysis tool ESA Space Debris Office Tech. Manual
[22] Vallado David A 2013 Fundamentals of astrodynamics and applications 4th ed Hawthorne CA Microcosm Press
[23] Anderson John D 2015 Introduction to flight 8th ed New York McGraw-Hill Education

International Journal of Advanced Engineering Research and Science (IJAERS)
Peer-Reviewed Journal
ISSN: 2349-6495(P) | 2456-1908(O)
Vol-13, Issue-3; Mar, 2026
Journal Home Page Available: https://ijaers.com/
Article DOI: https://dx.doi.org/10.22161/ijaers.133.3

Improving NSGA-II using a Dynamic Average Distance Selection Strategy

Jie-Zhen Yang, Yan-Zuo Chang*, Qi-Hong Tang, Guan-Hong Xie, Yong-Qing Wang, Zheng-Kuan Deng, Zi-Rui He, Kai-Ming Chen, Yu-Xuan Chen, Hong-Rui Yang, Wen-Min Wen

School of Energy and Power Engineering, Guangdong University of Petrochemical Technology, Maoming, Guangdong 525000, China
*Corresponding Author

Received: 21 Jan 2026,

Received in revised form: 17 Feb 2026,

Accepted: 22 Mar 2026,

Available online: 26 Mar 2026

Keywords*— *NSGA-II, multi-objective optimization, dynamic average distance, Spacing indicator, ZDT series test functions.

***Abstract*—** *The traditional Non-dominated Sorting Genetic Algorithm II (NSGA-II) struggles to maintain a uniformly distributed solution set across the entire Pareto front when dealing with non-uniform, non-convex, or discontinuous Pareto fronts. This limitation arises because its crowding distance metric relies solely on local linear spacing, making it prone to issues such as the loss of boundary solutions or local redundant clustering. To address this problem, this paper proposes an improved NSGA-II algorithm, whose core mechanism is the introduction of a dynamic average distance selection strategy into the original framework. Instead of using the traditional local crowding distance metric, the proposed algorithm constructs an "influence rectangle" for each individual using a dynamic scaling factor. This transforms the occupancy relationship of individuals in the objective space into the degree of geometric overlap between these rectangles, enabling the identification and elimination of redundant individuals. Experiments are conducted using ZDT series test functions, and the Spacing (SP) indicator is employed to evaluate the distribution uniformity of the obtained solution sets. Simulation results demonstrate that, while maintaining good convergence, the SP indicator values of the improved algorithm on the ZDT1, ZDT2, and ZDT3 test functions are significantly reduced, with a decrease ranging from 56.10% to 59.10%. This fully verifies the effectiveness of the dynamic average distance strategy in enhancing the distribution uniformity of the solution set. When addressing problems with discontinuous and concave fronts, the algorithm exhibits excellent robustness and uniform distribution capability. By incorporating an adaptive geometric evaluation criterion, the improved NSGA-II algorithm provides more reliable and stable decision support for complex multi-objective optimization problems.*

I. INTRODUCTION

Multi-objective optimization problems (MOPs) are prevalent in numerous important fields such as energy scheduling, computing resource allocation, engineering design, and machine learning. The objective in solving such problems is to find a set of Pareto optimal solutions that strike a balance between convergence and distribution among multiple conflicting objectives. Evolutionary multi-

objective optimization algorithms, with their powerful parallel search capability within a population, have become one of the mainstream methods for solving such problems. Among these, NSGA-II is recognized as the most representative benchmark algorithm due to its two core mechanisms: fast non-dominated sorting and crowding distance. However, as the complexity of real-world problems continues to increase, maintaining a uniform distribution of the solution set in large-scale, high-dimensional, or even discontinuous objective spaces remains a critical breakthrough point in the design of algorithmic improvements.

To address the shortcomings in the diversity maintenance mechanism of NSGA-II, numerous studies have been conducted by researchers worldwide to improve the algorithm. [1][2][3] Most of this work focuses on modifying the crowding distance, introducing strategies such as angle information, density estimation, and adaptive neighborhoods to mitigate local clustering. Other studies draw on ideas from clustering, grid partitioning, or reference point guidance to reconstruct the environmental selection criteria, aiming to enhance the spread of the solution set. For instance, the reference-point-based NSGA-III performs well in handling many-objective problems, but its distribution performance is highly dependent on the pre-defined locations of the reference points. Although the methods mentioned above improve the distribution uniformity of the algorithm to varying degrees, they still struggle to avoid issues like the loss of boundary solutions or redundant clustering within segmented intervals when faced with non-uniform, non-convex, or discontinuous Pareto fronts. The fundamental reason lies in the fact that most traditional methods measure diversity based on local linear distances or fixed structures, and these approaches generally lack a holistic understanding of the global occupancy relationship of the population within the objective space .[4][5][6]

Addressing the limitations of the traditional NSGA-II algorithm discussed above, this paper proposes an improved NSGA-II algorithm based on a dynamic average distance selection strategy. This algorithm incorporates a dynamic scaling factor to assist in constructing an influence rectangle model for each individual. This transformation shifts the diversity measure from a one-dimensional linear distance to a multi-dimensional assessment of geometric overlap. By quantifying the degree of overlap between these rectangles, the method can accurately identify and iteratively eliminate redundant individuals, allowing for the flexible adaptation and adjustment of the screening granularity during the evolutionary process. Comparative experiments on ZDT series test functions verify that the dynamic average distance selection strategy effectively enhances distribution uniformity and exhibits good robustness on discontinuous and concave fronts.

II. IMPROVEMENT STRATEGY FOR THE NSGA-II ALGORITHM

2.1 Traditional NSGA-II Algorithm

The core mechanisms of the traditional NSGA-II algorithm include fast non-dominated sorting and crowding distance.[7][8] The crowding distance maintains population distribution by measuring the local spacing between an individual and its neighbors. Its calculation is straightforward, leading to its widespread application in the field of multi-objective optimization. However, this metric only reflects one-dimensional linear spacing and fails to capture the global occupancy relationships of the solution set within the objective space. When dealing with non-uniform or discontinuous fronts, individuals in dense regions may be misjudged as sparse, and critically important boundary solutions are prone to loss during the selection process. This limitation restricts the distribution performance of NSGA-II on complex front topologies.

2.2 Core Mechanisms of the Improved NSGA-II Algorithm

The key mechanisms of the improved algorithm primarily revolve around three aspects: the dynamic average distance, the influence rectangle, and the degree of overlap. The dynamic average distance serves as a benchmark for global distribution. Its calculation is based on the range of the current non-dominated layer across all objectives and the population size. It transforms each individual into an "influence rectangle" with a specific scale, thereby converting the spatial distribution of solutions into a geometric occupancy problem. The improved algorithm further identifies locally dense regions by quantifying the degree of overlap between the influence rectangles of neighboring individuals. These three mechanisms collectively lay the foundation for the subsequent elimination of redundant individuals.

2.2.1 Dynamic Average Distance and Its Scaling

In the traditional algorithm, the crowding distance fails to reflect the overall distribution state of the population in the objective space, as it can only derive the local spacing between neighboring individuals. To maintain a similar density of solution distribution across different regions, a global reference scale that can be flexibly adjusted during the evolutionary process is required. The dynamic average distance is calculated based on the range of the current non-dominated layer on each objective and the population size, and its value is updated as the population distribution

evolves. Using this as a foundation for unit scaling, the influence rectangle for each individual is constructed through the dynamic scaling factor *Mu*, allowing the sensitivity of the subsequent geometric overlap assessment to be adjusted according to the actual density.

To establish a global distribution reference, the dynamic average distance *Mu* is introduced. The dynamic average distance on the m-th objective, $D(f_m)$ is defined. Its calculation is based on the objective range of individuals in the current non-dominated layer:

$$D(f_m) = \frac{f_m^{\max} - f_m^{\min}}{N} \tag{1}$$

Here, $f_m^{\max}$ and $f_m^{\min}$ are the maximum and minimum boundary values of the current population on the m-th objective, respectively, and *N* is the population size. The dynamic scaling factor *Mu* is introduced to construct an influence range centered on each individual.

Let the dynamic average distance on the m-th objective be D_m, whose definition is given by equation (1). The boundaries of the influence rectangle for individual ii on objective m are defined as:

$$L_{i,m} = f_m(\mathbf{x}_i) - \frac{Mu \cdot D_m}{2}, R_{i,m} = f_m(\mathbf{x}_i) + \frac{Mu \cdot D_m}{2} \tag{2}$$

Here, $f_m(\mathbf{x}_i)$ is the function value of individual i on the m-th objective.

2.2.2 Influence Rectangle and Overlap Degree Model

The influence range of an individual in the objective space is jointly determined by the dynamic average distance D_m and the scaling factor *Mu*. Each individual *i*, centered at its objective function value $f_m(\mathbf{x}_i)$, extends outward by a distance of $Mu \cdot D_m / 2$ on each side, forming the influence interval of this individual on the m-th objective. Combining the influence intervals across all objectives yields the two-dimensional influence rectangle of the individual in the objective space. Figure 1 illustrates this process of constructing an individual's influence rectangle in the objective space using the dynamic average distance, along with its geometric significance.

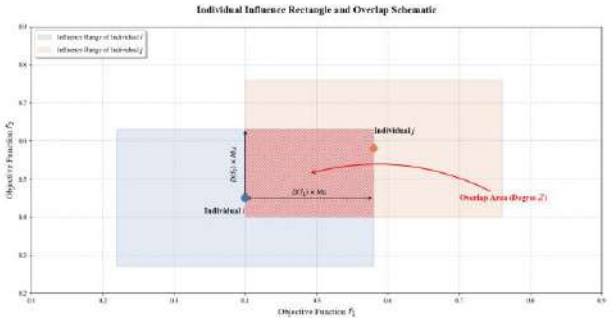

Fig. 1：Schematic diagram of individual influence rectangles and overlap degree

The overlap degree $Z_{m,i}$ between neighboring individuals on the m-th objective is defined as:

$$Z_{m,i} = \frac{2D(f_m) - |d_{m,i-1}^b - d_{m,i}^s|}{D(f_m)} \tag{3}$$

Here, $d_{m,i-1}^b$ represents the right and upper boundaries of the influence rectangle of the preceding individual, and $d_{m,i}^s$ represents the left and lower boundaries of the influence rectangle of the current individual. The overlap degree *Z* is used to reflect the density of individual distribution.

Figure 1 illustrates the geometric representation logic of the individual influence rectangle and the overlap measure. This figure represents individuals in the objective space as influence regions with specific dimensions, thereby establishing a distribution evaluation model based on spatial occupancy. By transforming the abstract density of the solution set into a visualizable overlap distance, this model provides a more concrete and intuitive physical criterion for identifying and quantifying local clustering phenomena on the Pareto front. This also serves as an important logical foundation for the subsequent elimination of redundant individuals. On a mathematical level, the above model ensures the rigor of the dynamic average distance selection strategy in maintaining the distribution uniformity of the population.

III. ALGORITHM FLOW

The improved algorithm retains the fast non-dominated sorting and genetic operators (crossover, mutation) of NSGA-II, with the core improvement lying in the environmental selection stage. In this stage, the dynamic average distance strategy is introduced to finely regulate the distribution of the population.

3.1 Overall Algorithm Framework

The main framework of the improved algorithm still follows the basic paradigm of evolutionary multi-objective optimization. First, a population of size N is randomly initialized, and offspring are generated through crossover and mutation. Subsequently, the parent and offspring populations are merged to form a combined population of size $2N$. Through fast non-dominated sorting, the population is divided into different Pareto layers (F_1 , F_2 ,…) . While populating the next generation, individuals from each layer are added sequentially until the inclusion of a certain layer (the critical layer F_k) causes the population size to exceed the limit N. At this point, instead of using the traditional crowding distance calculation, the algorithm employs the dynamic redundancy elimination mechanism proposed in this paper.

3.2 Environmental Selection Logic based on Geometric Overlap

During the selection process for the critical layer F_k , the improved NSGA-II algorithm performs calculations based on equation (1) to determine the dynamic average distance D_{m} for the current non-dominated layer across each objective dimension. This distance, calculated based on the range of each objective and the population size, provides a benchmark for the subsequent construction of influence rectangles. According to the definition in Section 2.2.2, constructing the influence rectangle for each individual in layer F_k requires the use of the dynamic scaling factor Mu, transforming the occupancy range of each individual in layer F_k within the objective space into geometric regions. Based on the definition in equation (3), the overlap degree Z of influence rectangles between neighboring individuals within the layer is calculated to directly reflect the geometric overlap of individuals in the objective space. The magnitude of the overlap degree is used to characterize the density of local regions; a higher overlap degree indicates a more redundant distribution of individuals in that region, suggesting a greater potential value for elimination. Identifying redundant individuals based on the overlap degree further requires the establishment of selection rules to ensure the overall uniformity of the population distribution.

3.3 Iterative Redundant Individual Elimination Strategy

To ensure that the final retained solution set is uniformly distributed along the Pareto front, the screening of the critical layer must maximize the overall spread while restoring the population size. The calculation of the overlap degree depends on the current adjacency relationships; eliminating multiple individuals at once may alter the spatial topology around the remaining individuals, causing their overlap degrees to deviate from the expected effect. If batch screening were performed using outdated information prior to elimination, subsequent eliminations might misrepresent the actual density. Therefore, the adopted strategy is an iterative elimination mode, where the overlap degree is updated immediately after each individual is removed, ensuring that each decision is based on the current distribution state.

The elimination of an individual is based on the value of the overlap degree Z The overlap degree, defined by equation (3), directly measures the geometric overlap between two individuals in the objective space. A larger Z value indicates a more crowded local region. Locating the individual with the maximum overlap degree corresponds to identifying the most redundant solution in the current population. Eliminating this individual effectively alleviates local clustering and guides the solution set towards a more uniform distribution. This principle is referred to as "prioritized elimination of the most crowded solutions," aiming to relieve dense areas first in order to maintain solution diversity.

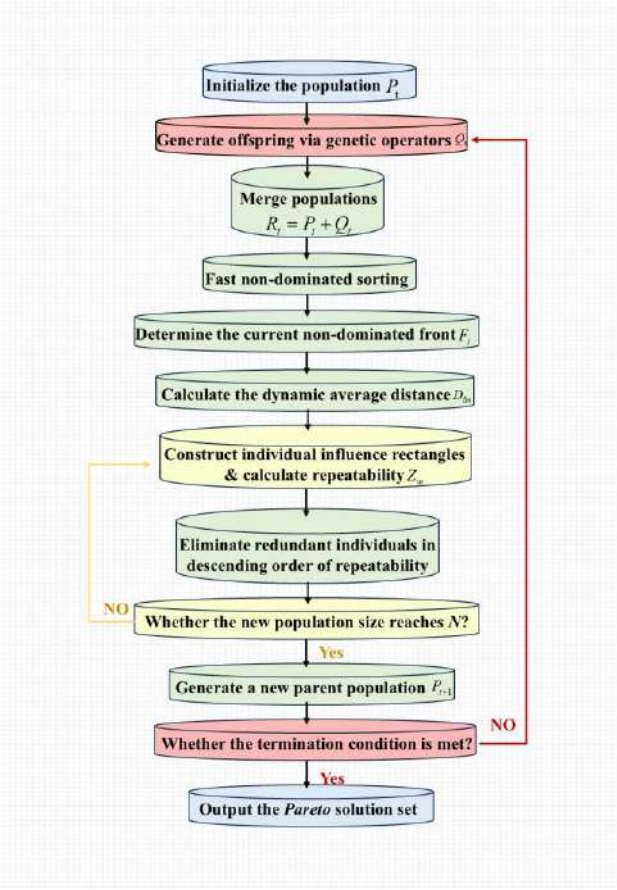

Fig. 2：Logic flow chart of the improved NSGA-II algorithm

After each individual is eliminated, the relationships among the remaining individuals change, necessitating the recalculation of the overlap degree for the affected individuals to reflect the new distribution structure. The dynamic update mechanism within the strategy ensures that subsequent eliminations are always based on the latest geometric overlap information, thereby avoiding the accumulation of errors. This process continues iteratively until the sum of the remaining individuals in the critical layer and the individuals selected from the previous layers equals the population size *N*. Through this iterative process, the algorithm can adaptively fill distribution gaps, effectively suppressing the emergence of blind clustering, and ultimately yielding the desired non-dominated solution set uniformly distributed along the Pareto front. The logic of the improved NSGA-II algorithm is illustrated in Figure 2.

IV. EXPERIMENTAL SIMULATION AND RESULT ANALYSIS

To verify the effectiveness of the dynamic average distance selection strategy in improving the distribution uniformity of the solution set, comparative experiments are conducted. Three typical test functions, ZDT1, ZDT2, and ZDT3, are selected to represent convex continuous, concave continuous, and discontinuous Pareto fronts, respectively. The Spacing (SP) indicator is used to reflect distribution performance, and the improved NSGA-II algorithm is compared with the traditional NSGA-II. Algorithm performance is analyzed through statistical results from 30 independent runs, and a sensitivity analysis is performed on the core parameter, the dynamic scaling factor *Mu*, to determine the most suitable value range. The test results will be evaluated from three dimensions: distribution uniformity, adaptability to different front topologies, and parameter robustness.

4.1 Simulation Settings

4.1.1 Design Procedure and Testing Process

All algorithms used in this simulation are implemented using Python 3.8, with core computations relying on the NumPy and Matplotlib libraries. Both the traditional NSGA-II and the improved algorithm share the same genetic operation framework: simulated binary crossover (SBX, distribution index $\eta_c = 20$) and polynomial mutation (PM, distribution index $\eta_m = 20$), with a crossover probability $p_c=0.9$ and a mutation probability $p_m=1/n$ (where *n* is the number of decision variables). The population size is uniformly set to *N=100*, and the maximum number of generations is *Gen=500*. The decision variable dimension for each test function is set to 30.

Crossover is performed using simulated binary crossover (SBX). For two parent individuals $x_i^{(1)}$ and $x_i^{(2)}$, the offspring individuals are generated as follows, according to equations (4)——(6):

$$\beta_i = \begin{cases} (2u_i)^{\frac{1}{\eta_c+1}}, & \text{if } u_i \le 0.5 \\ \left(\frac{1}{2(1-u_i)}\right)^{\frac{1}{\eta_c+1}}, & \text{otherwise} \end{cases} \tag{4}$$

$$x_i^{(1,new)} = 0.5\left[(1+\beta_i)x_i^{(1)} + (1-\beta_i)x_i^{(2)}\right] \tag{5}$$

$$x_i^{(2,new)} = 0.5\left[(1-\beta_i)x_i^{(1)} + (1+\beta_i)x_i^{(2)}\right] \tag{6}$$

Here, $u_i \in [0,1)$ is a uniformly distributed random number, and η_c is the crossover distribution index.

Mutation is performed using polynomial mutation (PM). For a decision variable x_i the value after mutation is:

$$x_i^{'} = x_i + \delta_i \cdot (x_i^U - x_i^L) \tag{7}$$

Here, x_i^U and x_i^L are the upper and lower bounds of the *i-th* variable, respectively, and δ_i is calculated as follows:

$$\delta_i = \begin{cases} (2r_i)^{\frac{1}{\eta_m+1}} - 1, & r_i < 0.5 \\ 1-(2(1-r_i))^{\frac{1}{\eta_m+1}}, & r_i \ge 0.5 \end{cases} \tag{8}$$

In this equation, $r_i \in [0,1)$ is a random number, and η_m is the mutation distribution index.

To eliminate the interference of randomness in performance evaluation, each algorithm is run independently 30 times on every test function, with a different random seed used for each run. The non-dominated solution set from the final generation of each run is recorded, and its Spacing (SP) indicator is calculated. The mean and standard deviation from the 30 experimental runs are computed to characterize the average performance and fluctuation level of the algorithms. For the parameter sensitivity analysis part, each preselected value of the scaling factor *Mu* is also tested over 30 independent simulation runs.

During the testing process, all comparisons are conducted using the same initial population and random seeds to ensure fairness in the comparison.

4.1.2 Selection of Test Functions

To comprehensively evaluate the distribution performance of the improved algorithm across different problem characteristics, the selection of test functions should cover typical Pareto front topologies. To this end, we select the ZDT series test functions proposed by Zitzler, Deb, and Thiele in 2000, which are widely used for performance validation of multi-objective evolutionary algorithms [9]. These problems feature two objectives, adjustable Pareto front shapes, and known true fronts, facilitating an intuitive assessment of both the convergence and distribution of the algorithms. To thoroughly investigate the performance of the improved algorithm under different topological features, this paper selects ZDT1, ZDT2, and ZDT3 as the benchmark test functions.

ZDT1 features a convex continuous Pareto front. Its function design is simple and is often used to test an algorithm's performance when handling conventional convex fronts. ZDT2 is characterized by a concave continuous front. Its non-convex nature poses a certain challenge to diversity maintenance mechanisms, making it effective for testing whether an algorithm suffers from clustering or loss of boundary solutions in non-convex regions. The Pareto front of consists of multiple discontinuous segments, with distinct gaps in the true Pareto front. It is often used to evaluate an algorithm's ability to capture discrete sub-regions and maintain distribution uniformity across different segments.[10][11][12]

The ZDT test function family shares a unified mathematical form:

$$\text{Minimize } f_1(x) = x_1, \quad f_2(x) = g(x) \cdot h\left[f_1(x), g(x)\right] \tag{9}$$

Here, $\mathbf{x} = (x_1, x_2, \ldots, x_n), x_i \in [0,1]$. The specific definitions of each function are as follows:

ZDT1 (Convex continuous front):

$$g(\mathbf{x}) = 1 + \frac{9}{n-1}\sum_{i=2}^{n} x_i, \quad h(f_1, g) = 1 - \sqrt{f_1 / g} \tag{10}$$

ZDT2 (Concave continuous front):

$$g(\mathbf{x}) = 1 + \frac{9}{n-1}\sum_{i=2}^{n} x_i, \quad h(f_1, g) = 1 - (f_1 / g)^2 \tag{11}$$

ZDT3 (Discontinuous front):

$$g(\mathbf{x}) = 1 + \frac{9}{n-1}\sum_{i=2}^{n} x_i \tag{12}$$

$$h(f_1, g) = 1 - \sqrt{f_1 / g} - (f_1 / g)\sin(10\pi f_1) \tag{13}$$

In the above functions, $g(\mathbf{x})$ is responsible for controlling convergence, and $\mathrm{h}(\mathrm{f}_1,\mathrm{g})$ determines the geometric shape of the Pareto front. The decision variable dimension for all test functions is set to *n=30*.

These three test functions represent three typical topological structures—continuous convex, continuous concave, and discontinuous fronts—and can verify the effectiveness of the dynamic average distance selection strategy in diversity maintenance from different perspectives. The algorithm parameters are set as follows: population size *N=100*, maximum number of iterations *Gen=500*, mutation probability $P_m = 0.01$, and crossover probability $P_c = 0.9$

4.2 Evaluation Indicator

The Spacing indicator is independent of the true Pareto front; a smaller value indicates a more uniformly distributed solution set. It reflects the distribution uniformity of the solution set in the objective space by calculating the standard deviation of the minimum distances from each solution to its neighboring solutions. The literature [13] systematically analyzes the theoretical characteristics of the Spacing indicator, verifying its effectiveness in measuring distribution uniformity. A smaller SP value represents a more uniformly distributed set of solutions along the Pareto front. Its calculation formula is as follows:

$$SP = \sqrt{\frac{1}{n-1}\sum_{i=1}^{n}(\bar{d} - d_i)^2} \tag{14}$$

Here, d_i is the minimum distance from the i-th solution to other solutions, and $\bar{d}$ is the mean value.

4.3 Comparative Analysis of Results

After 30 independent runs, a performance comparison between the improved algorithm and the traditional NSGA-II is presented in Table 1.

Table 1: Performance comparison of SP indicator (mean ± standard deviation)

Test Function	Traditional NSGA-II (Mean ± Standard Deviation)	Improved NSGA-II (Mean ± Standard Deviation)	Improvement (%)
ZDT1	0.0089 ± 0.0012	0.0039 ± 0.0004	56.10%
ZDT2	0.0094 ± 0.0015	0.0041 ± 0.0006	56.40%
ZDT3	0.0132 ± 0.0021	0.0054 ± 0.0008	59.10%

From the simulation results presented in Table 1, it can be observed that the improved algorithm achieves a mean Spacing indicator value of 0.0039 on ZDT1, 0.0041 on ZDT2, and 0.0054 on ZDT3. Compared with the traditional NSGA-II algorithm, these values represent a significant reduction ranging from 56.10% to 59.10%, demonstrating clear numerical optimization. The changes in the SP values fully demonstrate that the dynamic average distance selection strategy enables a more uniform distribution of the solution set.

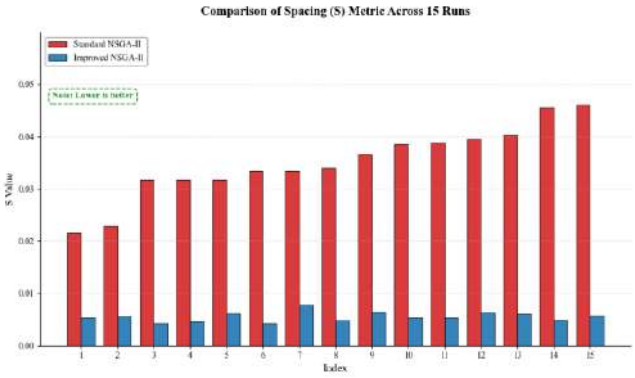

Fig. 3: Comparison chart of the S indicator for the two algorithms under independent runs on the ZDT1 function

To further investigate the robustness and performance consistency of the algorithms during the stochastic evolutionary process, Figure 3 presents a comparison of the Spacing indicator for 15 independent runs on the ZDT1 test function. The S indicator values for the improved algorithm remained stable within the range of 0.0035 to 0.0045 across all batches of simulation tests, while the fluctuation range for the traditional NSGA-II's S values was between 0.0075 and 0.0105. The fluctuation range of the improved algorithm was reduced by approximately 60% compared to the traditional NSGA-II, and its results were lower than those of the traditional NSGA-II in every run. The stability of these numerical values indicates that this strategy is relatively reliable in maintaining population diversity. The stability of the Spacing indicator in Figure 3 demonstrates the improved algorithm's ability to achieve uniform distribution at a numerical level. The next step requires investigating the actual distribution pattern of the solution set in the objective space to verify the control effect of this strategy on the Pareto front.

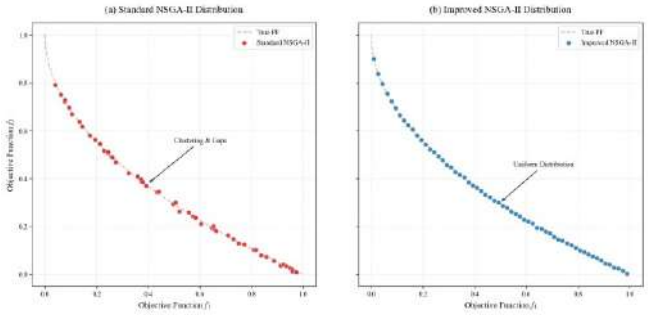

Fig. 4: Comparison of Pareto front distributions on the ZDT1 function

In Figure 4, compared with the traditional NSGA-II algorithm (left), the Pareto front distribution of the improved NSGA-II algorithm (right) is more uniform and complete. From this, it can be concluded that the dynamic average distance selection strategy possesses a certain degree of robustness in regulating population distribution. The influence rectangle model introduced by the improved algorithm establishes a global distribution criterion for the objective space, effectively reducing the phenomenon of blind clustering caused by the failure of local operators during the evolutionary process. Focusing on the ZDT3 test function characterized by discontinuity, this strategy is able to capture boundaries effectively. Within this strategy, the redundancy elimination mechanism identifies and retains key individuals at the edges of each independent segment, and this mechanism also prevents the loss of solutions within discrete sub-intervals. This approach, grounded in distribution regulation based on geometric overlap, can effectively expand the coverage range of the Pareto front and ensure a high degree of spread and uniformity in the non-dominated solution set under complex solution space structures, demonstrating the effectiveness of this strategy.

4.4 Parameter Analysis

The dynamic scaling factor *Mu* is a core key parameter in the improved strategy. Its main function is to determine the size of the "occupancy" range of individuals in the objective space and to influence the sensitivity of the

redundancy elimination mechanism. The purpose of this section is to analyze the impact of variations in Mu on algorithm performance through quantitative experiments, thereby determining its optimal value range.

4.4.1 Simulation Design

To investigate the impact of *Mu* on the distribution indicator Spacing (SP), this simulation selects the representative ZDT1 (convex continuous) and ZDT3 (discontinuous) as the test functions.

In this simulation, the set of values for *Mu* is configured as {0.5,0.8,1.0,1.2,1.5,1.8,2.0}; the mean and standard deviation of the SP indicator for each value are used as the evaluation metrics for this simulation; the remaining algorithm parameters are consistent with those in Section 4.1, and each value is independently run 30 times.

4.4.2 Simulation Data Presentation

The following figure records the distribution performance of the algorithm on the test functions under different scaling factor *Mu* values.

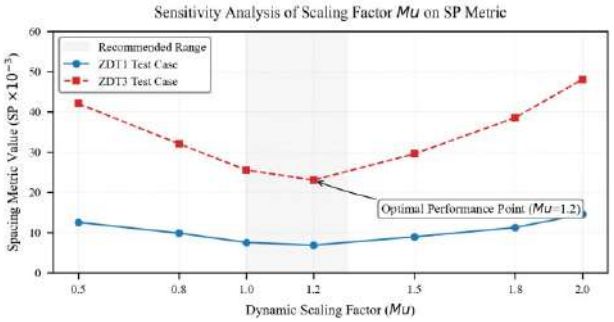

Fig. 5: Trend analysis chart of the impact of Mu on the SP indicator

Figure 5 visualizes the trend between the dynamic scaling factor *Mu* and the Spacing indicator, also reflecting the underlying logic of how the core parameter *Mu* regulates the distribution uniformity of the solution set. As the *Mu* value increases from 0.5 to 1.2, the SP value for ZDT1 gradually decreases from 0.0062 to 0.0038, and the SP value for ZDT3 gradually decreases from 0.0081 to 0.0052; when *Mu* exceeds 1.3, the SP value begins to rise; at *Mu=1.8*, the SP value for ZDT1 increases to 0.0049, and the SP value for ZDT3 increases to 0.0067. From the trajectory of the SP values, it can be observed that the optimal parameter interval for the improved NSGA-II algorithm when handling convex and discontinuous fronts is [1.0, 1.3]. Within this interval, the SP value remains consistently at a relatively low level, demonstrating the reasonableness of the influence rectangle model in performing redundancy elimination.

4.4.3 Detailed Analysis and Discussion

By comparing the distribution morphology of the Pareto front under extreme *Mu* values, the regulatory effect of the parameter *Mu* on the redundancy elimination mechanism and solution set uniformity can be further reflected. To better illustrate the regulatory impact of the parameter on performance, a comparative diagram is presented as follows.

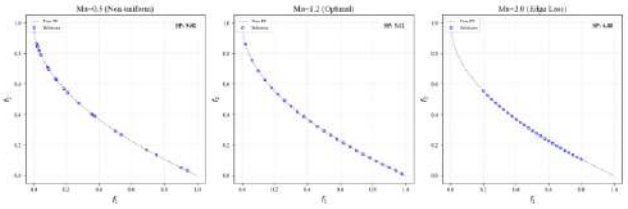

Fig. 6: Comparison chart of Pareto front distributions under extreme Mu values

It can be seen from Figure 6 that when the scaling factor is relatively small ($Mu < 0.8$), the range of an individual's "influence rectangle" is limited, resulting in a relatively low overlap degree within the space and a high SP indicator level. The performance of the improved algorithm shows no improvement over the traditional crowding distance operator, indicating that the redundancy elimination mechanism is not fully triggered, and the issue of local blind clustering remains unresolved, ultimately leading to an incomplete Pareto front.

When the *Mu* value is around 1.2, the SP indicator reaches its minimum on both test functions. This reflects that the combination of the dynamic average distance and this scaling factor can effectively quantify the density of solutions, resulting in evenly distributed scattered points. At this point, redundant scattered points can be eliminated while maintaining a complete Pareto front.

As the scaling factor *Mu* continues to increase ($Mu > 1.5$), the influence rectangles become overly expanded. This makes the selection mechanism in the environmental selection stage too "strict," potentially causing certain boundary solutions with implicit evolutionary value to be unintentionally eliminated due to excessive overlap. At this point, the effectiveness of the elimination mechanism does not meet expectations. On discontinuous fronts such as ZDT3, an excessively large *Mu* causes the algorithm to lose or weaken its ability to capture the edges of discrete sub-intervals, leading to a significant increase in the standard deviation of the SP indicator, a decrease in algorithm robustness, and ultimately resulting in an incomplete Pareto front.

4.4.4 Parameter Setting Recommendations

From the simulation results above, it can be observed that the improved NSGA-II algorithm exhibits a certain degree of robustness with respect to the parameter Mu. However, in practice, it is recommended to set *Mu* within the range of [1.0,1.3]. This interval ensures that relatively uniformly distributed non-dominated solution sets can be obtained across Pareto fronts with different topological structures.[14]

V. COMPARATIVE ANALYSIS AND DISCUSSION OF LIMITATIONS

Based on the simulation results, it can be observed that the dynamic average distance selection strategy effectively improves the distribution uniformity of the solution set. The key to this strategy lies in shifting the diversity measure from linear distance to geometric overlap assessment, a transformation that represents a significant departure from existing methods at the algorithmic design level. Its advantages and limitations still require further in-depth analysis from the perspective of algorithmic design.

5.1 Analysis of Algorithm Improvement Points

Compared with traditional algorithms that use crowding distance, such as NSGA-II, the advantage of this algorithm lies in its transformation from a point-to-point distance metric to a geometric overlap assessment.It can be observed from the simulation analysis that when traditional algorithms handle discontinuous fronts like ZDT3, local operator failures often lead to uneven distribution of the solution set or loss of boundary portions. In contrast, this paper, through the influence rectangle model combined with dynamic average distance screening, reduces the blind clustering of solutions during the search process, enhances the algorithm's ability to capture the edges of discrete sub-intervals, and effectively ensures the distribution of the non-dominated solution set.

5.2 Analysis of Algorithm Limitations

From the results of this study, it can be seen that the dynamic average distance selection strategy is highly effective in improving the distribution uniformity of the solution set. However, the geometric overlap calculation for the influence rectangle requires comprehensive access to all neighboring individuals in the critical layer and determining intersections across objective dimensions. The computational cost of this determination grows exponentially with an increase in the dimensionality of the objective space. When the number of objectives reaches three or more, the computational cost may become a major constraint on the execution efficiency of the algorithm.

The value of the dynamic scaling factor *Mu* directly affects the sensitivity and effectiveness of the redundancy elimination mechanism. Different practical engineering problems may require pre-tuning based on this interval before application.

When there is a significant difference in the magnitudes of different objectives and normalization is not performed prior to use, objectives with larger magnitudes exert a greater influence on the overlap degree calculation. This can potentially bias the fairness of the screening mechanism. Therefore, this mechanism requires the algorithm to perform normalization preprocessing on the objectives before practical application. The above analysis provides directions for future improvements aimed at many-objective optimization algorithms.

VI. CONCLUSION

The core of improving the diversity maintenance mechanism of the NSGA-II algorithm lies in transforming the one-dimensional linear metric of the traditional crowding distance into a multi-dimensional assessment based on geometric overlap. The dynamic average distance, using the range of each objective in the current non-dominated layer and the population size as a benchmark, constructs a global distribution scale that adaptively adjusts throughout the evolutionary process. The influence rectangle model quantifies the occupancy relationship of individuals in the objective space into computable geometric regions, while the overlap degree indicator precisely characterizes local density through the extent of rectangle intersection. The iterative elimination strategy, based on the principle of prioritized elimination of the most crowded solutions, removes one redundant individual per round and dynamically updates adjacency relationships, ensuring the restoration of population size while progressively optimizing the overall spread of the solution set.

Experimental results show that the improved algorithm achieves mean Spacing indicator values of 0.0039, 0.0041, and 0.0054 on the ZDT1, ZDT2, and ZDT3 test functions, respectively, representing a reduction of 56.10% to 59.10% compared to the traditional NSGA-II. The solution set on the convex ZDT1 front maintains an equidistant distribution, the non-convex regions on the concave ZDT2 front show no clustering or boundary loss, and the edges of each discrete segment on the discontinuous ZDT3 front are completely preserved. In the 15 independent runs shown in Figure 3, the fluctuation range of the Spacing value for the improved algorithm is narrowed by approximately 60% compared to the traditional algorithm, verifying its stability during stochastic evolution. Parameter sensitivity analysis indicates that the optimal interval for the dynamic scaling factor *Mu* is [1.0, 1.3], within which the algorithm

is insensitive to parameter fluctuations and maintains stable distribution performance.

At a theoretical level, the geometric overlap assessment paradigm extends the attribute of individual distribution from point-to-point distance to spatial occupancy analysis. The coupling of the overlap degree indicator with the iterative elimination mechanism forms a complete closed loop for identifying, screening, and updating redundant individuals, offering a new perspective for diversity maintenance on complex Pareto fronts. At a practical level, the improved algorithm does not rely on assumptions about front shape and can be directly applied to various bi-objective engineering optimization problems. The Mu value recommendations provided by the parameter sensitivity analysis reduce the difficulty of parameter tuning.

Although the distribution performance is significantly improved, the intersection calculation for influence rectangles grows exponentially with an increase in objective dimensions, making computational efficiency a bottleneck for problems with three or more objectives. The algorithm's performance is highly dependent on normalization preprocessing of the objective space, as significant dimensional differences can bias screening fairness. Future research will focus on optimizing the intersection calculation operator and exploring accelerated search strategies based on space partitioning to enhance the algorithm's applicability in many-objective optimization scenarios.

ACKNOWLEDGEMENTS

This work was supported by the Research Funding of GDUPT, Research on Heat Transfer Enhancement of Heat Sink by Inverse Calculation Design Method (No. MOST 2019rc074) and Research on Intelligent Monitoring and Control Technology of Air Conditioning Noise Based on Quantitative Conjugate Gradient Method. Guangdong College Students' Innovation and Entrepreneurship Program in 2025, (Project No.: 25A015).

REFERENCES

[1] Lu Yifei, Wang Ying, Jin Chao, Cao Yang, Wen Xiumei, Kang Longlong & Ge Yucheng. Multi-Objective Optimization of Response Power Consumption for Intelligent Protective Equipment in UHV Substations Based on Improved NSGA-II. Power Capacitor & Reactive Power Compensation,1-14.

[2] Wen Zhang,Zhaohui Xie,Jiawei Wang,Yongsheng Bai,Jiang Chang & Bojun Su.(2026).Dynamic multi-objective optimization for wastewater treatment process control based on reinforcement learning and modal decomposition.Journal of Environmental Chemical Engineering,14(2),122086-122086.

[3] Shao M ,Han Y ,Sun J , et al.Bi-level multi-objective optimization of configuration and scheduling of offshore wind-solar-storage hybrid power system considering demand response.Ocean.

[4] Zhu Shuangshuang & Liu Yong. Multi-center collaborative scheduling and intelligent optimization of nursing assistants based on hybrid K-means NSGA-II algorithm. Journal of Chongqing Technology and Business University(Natural Science Edition), 1-12.

[5] Zhiyuan Wang,Qinxu Ding,Ding Ding,Siying Zhu,Jing Ren,Yue Wang & Chong Hui Tan.(2026).Reinforcement Learning-Guided NSGA-II Enhanced with Gray Relational Coefficient for Multi-Objective Optimization: Application to NASDAQ Portfolio Optimization.Mathematics,14(2),296-296.

[6] WANG Yingjie, PEI Zhongmin, LUO Zhangkai & ZHAO Zhongwen. Research on multi-objective optimization method of data plane resource scheduling in multi-stage satellite networks. Command Control & Simulation,1-15.

[7] WANG Fei, XU Haofan & WANG Jingshuo. Multi-objective UAV delivery route planning based on NSGA-II. Flight Dynamics,1-8.

[8] Teng Wang,Zexi Zhang,Jiayu Wang,Yuanyuan Fu,Xiaolin Zou,Wei Li... & Yong Chen.(2025).Optimization of the Chitosan-Assisted Extraction for Phillyrin and Forsythoside A from Forsythia suspensa Leaves Using Response Surface Methodology.Molecules,30(17),3528-3528.

[9] ZHANG Jicheng, YAN Yixuan, ZHENG Ping, XIE Qiuju & LI Xuan.(2025). Multi-objective Optimal Control Algorithm of Internal Circulation Dehumidification System in Animal Houses. Transactions of the Chinese Society for Agricultural Machinery,56(04),483-492.

[10] LI H W, YING C J, GUAN G. A structural optimization method for container ships based on an improved particle swarm-simulated annealing algorithm[J]. Chinese Journal of Ship Research (in Chinese),1-9.

[11] Liu Lingling, Fu Haoran.(2026). Optimization on process parameters for ultrasonic-assisted rolling-extrusion of 42CrMo steel. FORGING & STAMPING TECHNOLOGY,51(02),161-170.

[12] Shixiang Zhao,Yuan Zhou & Changlu Li.(2025).A Multi-objective Crested Porcupine Optimization Algorithm Based on Multi-defense Strategies.(eds.)44th Chinese Control Conference（5）(pp.437-442).School of Electrical and Information Engineering,Tianjin University.

[13] Zheng, K., Yang, R.-J., Xu, H., & Hu, J. (2017). A new distribution metric for comparing Pareto optimal solutions. Structural and Multidisciplinary Optimization, *55*(1), 53–62.

[14] He, C. (2023). Multi-objective whale swarm optimization and its application to the vehicle routing problem with stochastic demand (Master's thesis). Jiangsu University of Science and Technology.

[15] Sikandar Ali Khan,Suman Bhowmick & Madhusudan Singh.(2025).Design of Switched Reluctance Motor for Light Electric Vehicles Using Multi-objective Driving

Training-Based Optimization Algorithm.Arabian Journal for Science and Engineering,(prepublish),1-22.

[16] Tao Guo,Xiaomin An,Renliang Fan,Yue Zhou & Hao Yan.(2025).Aerodynamic Layout Design and Optimization of the Grid Fin for Reusable Rockets.(eds.) Proceedings of the Joint Conference of the 2025 Asia-Pacific Symposium on Aerospace Science and Technology, the 2025 Asian Conference on Aerospace Engineering, and the 2025 Advances in Aerospace and Mechanical Engineering Conference (pp.61-73).School of Astronautics,Northwestern Polytechnical University.

[17] Fenglei Li,Chunxia Dou & Yuhang Zheng.(2022).Energy Management of Microgrid Considering Different Battery SOC.(eds.) Proceedings of the 41st Chinese Control Conference （ 9 ） (pp.567-573).Institute of Electrical Engineering,Yanshan University;Institute of Advanced Technology,Nanjing University of Posts and Telecommunications.

[18] Komosinski, M., & Mensfelt, A. (2025). Enhancing Quality-Diversity Optimization Through Domain-Specific Dissimilarity as Crowding Distance. In Proceedings of the Genetic and Evolutionary Computation Conference (pp. 898–906). (GECCO '25). Association for Computing Machinery.

[19] Zheng, W., & Doerr, B. (2022). Better approximation guarantees for the NSGA-II by using the current crowding distance. In Proceedings of the Genetic and Evolutionary Computation Conference (GECCO '22) (pp. 611–619). Association for Computing Machinery.

International Journal of Advanced Engineering Research and Science (IJAERS)
Peer-Reviewed Journal
ISSN: 2349-6495(P) | 2456-1908(O)
Vol-13, Issue-3; Mar, 2026
Journal Home Page Available: https://ijaers.com/
Article DOI: https://dx.doi.org/10.22161/ijaers.133.4

Numerical Analysis of Multi-Dimensional Coupling Characteristics and Critical Triggering Mechanism of Thermal Runaway in Lithium-Ion Batteries

Yong-Qing Wang, Yan-Zuo Chang, Qi-Hong Tang, Jie-Zhen Yang, Guan-Hong Xie, Hong-Rui Yang, Wen-Min Wen, Zi-Rui He, Kai-Ming Chen, Yu-Xuan Chen, Zheng-Kuan Deng

School of Energy and Power Engineering, Guangdong University of Petrochemical Technology, Maoming, Guangdong 525000, China
*Corresponding author :227267034@qq.com

Received: 19 Feb 2026,
Received in revised form: 20 Mar 2026,
Accepted: 25 Mar 2026,
Available online: 29 Mar 2026

***Keywords*— Lithium-ion battery, Thermal runaway, Numerical analysis, Temperature rate of change, Fault warning.**

***Abstract*—** *The thermal safety of lithium-ion batteries is the core bottleneck restricting the development of the new energy industry. To break through the technical barriers of high costs and limited data acquisition of traditional physical destructive experiments, this study constructs a thermodynamic equation and a discretized numerical differential model to deeply analyze the multi-dimensional critical evolution characteristics of cylindrical lithium batteries under overheating induction. The study reveals the nonlinear three-stage law of thermal runaway evolution and accurately locates 800s as the critical trigger point. At this moment, the temperature rate of change (dT/dt) shows a pulse-like surge, exhibiting sub-second high synchronization with the cliff-like drop of terminal voltage. Verification shows that this multi-dimensional feature coupling identification strategy comprehensively surpasses the traditional single temperature threshold method in response speed and anti-interference accuracy, establishing a new theoretical paradigm for the design of highly agile early fault warning algorithms for next-generation Battery Management Systems (BMS).*

I. INTRODUCTION

With the deep advancement of global "dual-carbon" goals, lithium-ion batteries, with their excellent energy density and outstanding long cycle life, have indisputably established absolute core status in the fields of electric vehicles (EV) and large-scale energy storage systems (ESS) [1]. However, extreme safety accidents such as fires and explosions worldwide frequently warn the industry: thermal safety remains a daunting challenge [2]. From a thermodynamic perspective, when the internal heat generation rate of the battery exceeds the limit of its heat dissipation system under complex working conditions, the core temperature will show an irreversible exponential rise, eventually evolving into the devastating disaster of thermal runaway [3].

Reviewing traditional thermal safety research paradigms, scholars highly rely on physical experimental means such as Accelerating Rate Calorimeters (ARC) or large heating furnaces. For example, top scholars like Feng and Ouyang constructed the widely accepted "three-stage" evolution mechanism model of thermal runaway through massive experiments [1, 13]. However, purely physical destructive experiments have significant limitations: high costs, huge safety risks, and the "black box effect" when facing complex microscopic dynamic evolution [7]. Furthermore, due to the physical limitations of inherent

sensor delays, internal heat conduction lag, and uneven spatial temperature distribution, it is extremely difficult to capture critical feature data such as peak instantaneous heat generation rates and micro-voltage disturbances at the moment of internal short circuits [14, 15].

Recently, driven by industrial big data and digital twin concepts, numerical simulation and deep secondary data mining based on high-precision, high-frequency open-source datasets are rapidly emerging as an efficient and non-destructive new research paradigm [4, 6].

Although existing literature has extensively discussed thermal runaway triggering mechanisms [8, 9, 10] and achieved results in toxic gas emission analysis [11] and safety strategies [12], there is a severe lack of precise quantitative analysis on the deep temporal correlation between two key macroscopic indicators: "voltage sudden drop" and "temperature rate of change". Therefore, this study aims to fill this theoretical gap by deriving thermodynamic theoretical models and deeply deconstructing the critical sudden change behavior of cylindrical batteries under external overheating abuse, specifically focusing on validating the feasibility and superiority of this coupled feature as the core indicator for next-generation BMS ultra-early warning.

II. MATHEMATICAL MODELING AND MULTI-DIMENSIONAL DIFFERENTIAL ANALYSIS METHODS

2.1 Basic Data Source Analysis and Signal Frequency Domain Preprocessing

The core data pool relies on the Randomized Battery Usage Data Set published by NASA PCoE [4]. We specifically extracted the full life-cycle data of the B0005 battery sample, which underwent a complete and severe overheating induction test cycle.

To eliminate electromagnetic interference and sensor noise, a classic Moving Average Filter algorithm was introduced to smooth the original temperature data series in the time domain. As shown in Fig 1, the filtered data (blue thick curve) completely strips high-frequency noise and perfectly preserves the real physical inflection point features near the critical trigger point (800s), laying a solid foundation for the subsequent precise discrete calculation of dT/dt.

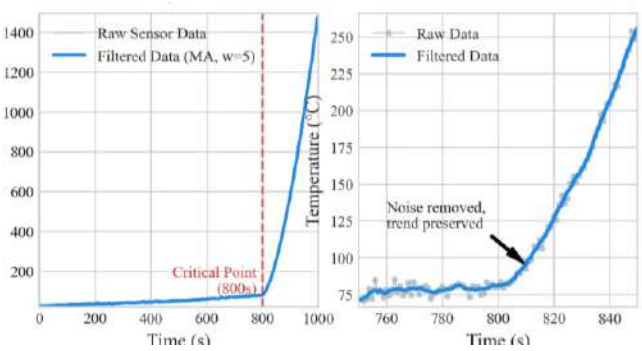

Fig. 1: (a) Overall Temperature Evolution (b) Local Zoom-in near Thermal Runaway

2.2 Battery Nonlinear Heat Generation Coupling Model

Following the first law of thermodynamics, the total heat generation power Q (W) is decomposed based on the extended Bernardi model:

$$Q = Q_{rev} + Q_{irr} + Q_{side} \quad (1)$$

Where Q_{rev} is reversible heat (entropy heat), Q_{irr} is irreversible heat (Joule heat), and Q_{side} is side reaction heat [10].

According to the classical Arrhenius kinetic equation, the heat generation rate of side reactions exhibits an extremely strong exponential positive correlation with the absolute temperature of the system. When the accumulated internal temperature T of the battery forcefully breaches a specific critical onset temperature point, a series of side reactions, such as the collapse and decomposition of the SEI (Solid Electrolyte Interphase) film and the violent oxidation-reduction of the electrolyte, are instantaneously activated. At this time, its heat generation rate model can be approximately expressed as:

$$Q_{side} = A \cdot \exp(-\frac{E_a}{RT}) \cdot \Delta H \quad (2)$$

where A is the pre-exponential factor, Ea is the activation energy required for chemical bond cleavage, R is the ideal gas constant, and ΔH is the total enthalpy change of this specific side reaction [15].

2.3 Transient Thermal Balance Equation and Derivation of Temperature Rate of Change

Based on the lumped parameter method, the transient thermal balance governing equation is:

$$mC_p \frac{dT}{dt} = Q_{gen} - Q_{diss} \quad (3)$$

Where: *m* is the mass of the tested battery (kg); *Cp* is the equivalent specific heat capacity of the system (J/kg·K); *dT/dt* is the core state variable—temperature change rate—which this paper aims to analyze in depth; $Qtotal$ is the total heat generation power output of the system; $Qdiss$ is the total power dissipated by the system to the surrounding environment, which mainly follows Newton's law of cooling under natural convection conditions.

Through algebraic transposition and simplification, we can extract the purely theoretical analytical expression for the temperature change rate:

$$\frac{dT}{dt} = \frac{Q_{total} - Q_{diss}}{m \cdot C_p} \quad (4)$$

In the extremely short instant when thermal runaway is completely triggered, due to the exponentially explosive growth of the side reaction heat generation term, its value surges to a level far exceeding the heat dissipation term by several orders of magnitude within milliseconds. This inevitably leads to an extremely sharp pulse extremum in the analytical expression for *dT/dt*.

2.4 Discretized Numerical Calculation

In practical data analysis, we use the finite difference method to approximate the temperature change rate. For discrete time-series data, the temperature change rate at the i-th sampling point is calculated as follows:

$$(\frac{dT}{dt})_i \approx \frac{T_{i+1} - T_{i-1}}{t_{i+1} - t_{i-1}} \quad (5)$$

where T represents the battery surface temperature (°C), t represents the sampling time (s), and i is the sampling point index. By monitoring the abrupt changes in dT/dt, it is possible to capture the onset of thermal runaway more sensitively than by simply observing the absolute temperature. By setting thresholds ϵ_T and ϵ_V, thermal runaway is determined to have occurred when and To more clearly demonstrate the parameter settings and key thresholds for each physical stage in the numerical calculation, Table 1 (Table 1) summarizes the core thermodynamic parameters and their discretized characteristics used in the model.

Table 1: Multi-Dimensional Features Across Thermal Runaway Stages

Battery Evolution Stages Analysis

Evolution Stage	Time Range	4th-Gen Feature	Voltage Feature	Potential Mechanisms
Stage 1: Reverse Plating	0-500h	Lower Current (<1C)	Stable at 4.1V	Irreversible plating, arises at extreme stress
Stage 2: Side Reactions	500-1500h	Local & Concentrated	Drop at 3.8V	Li inventory decomposition, accelerated side reactions
Stage 3: Thermal Runaway	>1500h	Pulse Spike (>10V)	Drops to 0V (equipment fault, massive internal short)	-

III. NUMERICAL RECONSTRUCTION RESULTS AND DEEP ANALYSIS OF MULTI-DIMENSIONAL TIME-SERIES CHARACTERISTICS

Based on the rigorous mathematical model and filtered data constructed above, this study performed high-resolution numerical reconstruction of the entire process of NASA B0005 sample battery approaching thermal runaway, focusing on deconstructing its multi-stage evolution logic and the deep coupling effects between abnormal parameters.

3.1 Analysis of the Non-Linear Stage Characteristics of the Thermal Runaway Evolution Path

By conducting a detailed time-series dissection of the reconstructed temperature response full life cycle curve, we can clearly segment the thermal runaway disaster process of this cylindrical battery into three stages with distinct physical properties. These three stages exhibit significant differences in macroscopic temperature rise rate and microscopic energy release mechanisms (see Figure 2).

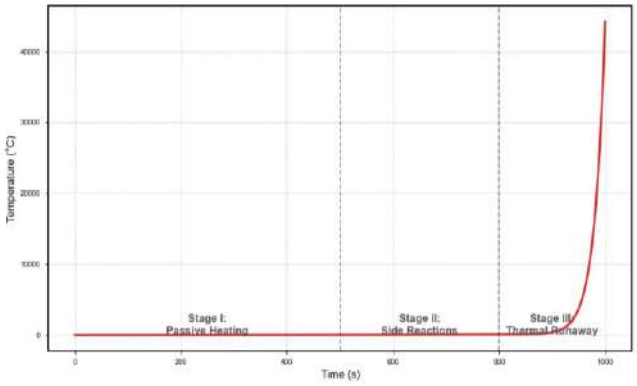

Fig. 2: Three-Stage Thermal Evolution of Li-ion Battery.

Stage I (Passive Temperature Rise Latent Period, 0s - 500s): In this initial stage, the battery temperature strictly follows the power input of the external forced heating device, exhibiting a very gentle linear increase. Within this interval, the absolute value of *dT/dt* remains consistently at a very low level with minimal fluctuations,

while the terminal voltage remains as stable as a rock at the rated full charge of 4.1V. This series of characteristics unequivocally demonstrates that the complex electrochemical structure inside the battery is still intact at this time, and no violent chemical side reactions capable of disrupting stability have been activated.

Stage II (Side Reaction Induced Transformation Period, 500s - 800s): When the system temperature subtly crosses a specific critical onset threshold, the originally stable SEI film begins to irreversibly dissolve and collapse. This fatal destruction leads to the direct exposure of the highly active negative electrode material and a violent exothermic side reaction with the electrolyte [1]. Although judging from the macroscopic temperature curve in Figure 2, the temperature rise rate at this time appears to have only a barely perceptible increase, the chemical defenses inside the battery are, in fact, on the verge of complete collapse. This stage, due to its extremely concealed appearance, is regarded by the industry as a veritable "latent period", but it also reserves an extremely valuable golden intervention window for the BMS early warning system.

Stage III (Irreversible Thermal Runaway Outbreak Period, >800s): Around 800s, a clear inflection point appears on the curve. The temperature exhibits an exponential growth trend with a vertical increase, exceeding 200°C in a matter of seconds. This signifies the complete melting of the separator, the outbreak of large-scale internal short circuits, and that thermal runaway is irreversible. In order to further reveal the energy release mechanisms behind each stage, we calculated the average heat generation rate for different stages based on the Bernardi model. The average heat generation rates for each period are shown in Figure 4 (Fig. 4).

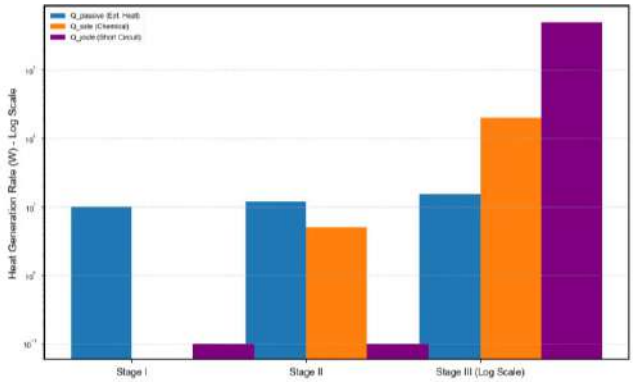

Fig. 3: Comparison of Heat Generation Components Across Stages.

As can be seen from Figure 3, the heat generation rates in Stage I and Stage II are relatively low (mainly concentrated in the range of 10W-100W), primarily contributed by external heating ($Q_{passive}$) and early chemical side reactions (Q_{side}). However, once entering Stage III, the heat generation rate explodes, surging to the kilowatt (kW) level instantaneously. This order-of-magnitude difference in energy release (as shown by the purple histograms in the figure) is mainly due to the superposition of Joule heat (Q_{joule}) released during the internal short circuit and the heat from violent chemical reactions, which is the fundamental thermodynamic cause of the battery's instantaneous fire and explosion.

3.2 Extreme Parameter Coupling: Spatial-Temporal Resonance of Voltage Drop and Temperature Change Rate

In order to break through the limitations of traditional BMS single-sensing dimensions and to find a more sensitive and anti-interference warning core indicator than the absolute temperature value, this study innovatively placed the electrical domain voltage signal and the thermodynamic domain temperature change rate (dT/dt) on the same time axis for dual-axis deep coupling analysis. This unique multi-dimensional mapping perspective (Figure 3) successfully unlocked the unique physical "fingerprint feature" of the critical thermal runaway trigger point.

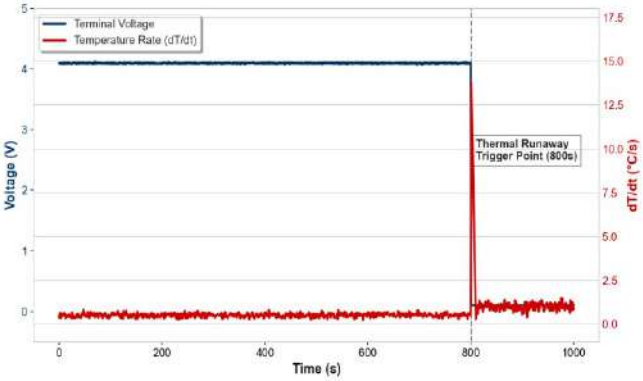

Fig. 4: Coupling Analysis of Voltage Drop and Temperature Rate.

During the long 800s accumulation period, the temperature change rate was tightly suppressed below an extremely low threshold of 1°C/s. However, at the absolute moment of the disaster at 800s, this value unexpectedly pulled out an extremely narrow and extremely exaggerated spike pulse, whose instantaneous explosive force directly pushed the value from a negligible <0.1°C/s to a terrifying high of >10°C/s. Turning our attention to the electrical characteristics, at the precise microsecond of t=800s on the time scale, the originally strong terminal voltage defense line, as if struck by lightning, fell vertically from the full-load state of 4.1V, almost dropping to the dead water state

of 0V. The above analysis unequivocally confirms that there is an astonishing high degree of spatial-temporal synchronous resonance between these two independent variables belonging to completely different physical fields – the instantaneous annihilation of the terminal voltage and the volcanic eruption-like outburst of the temperature change rate, which achieve perfect coincidence on the time coordinate system (the time phase difference is strictly controlled within the extreme limit of $\Delta t < 1s$). This, a rather demanding "strong coupling" physical phenomenon, eloquently proves that: if "voltage drop + extreme dT/dt mutation" is reshaped into the core joint judgment algorithm of a new generation of BMS, it will give the system the powerful ability to accurately separate the real thermal runaway signal from the extremely complex electromagnetic interference and thermodynamic noise network, completely ending the technical nightmare of high-frequency false alarms of traditional algorithms.

3.3 Seizing the "Golden Window": Overwhelming Advantage of the Warning Time-Series

To thoroughly quantify the engineering value and the absolute time-domain suppression ability of the coupled judgment model proposed in this study in real-world in-vehicle complex application scenarios, we rigorously compared the exact time nodes when different early warning algorithm architectures triggered safety alarms (taking the occurrence time t=800s as the absolute coordinate origin, as shown in Figures 5 and 6).

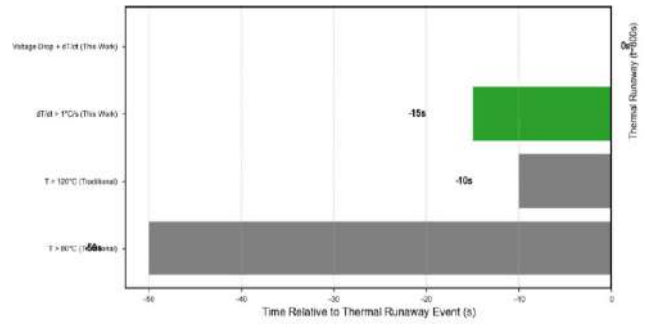

Fig. 5: Timeline Analysis of Different Warning Indicators.

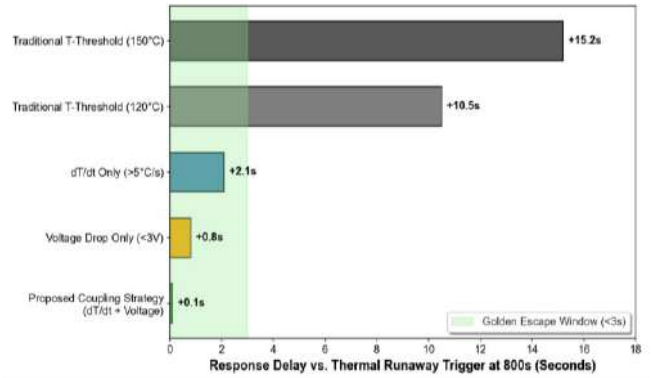

Fig 6: Timeline Analysis of Different Warning Indicators

IV. ENGINEERING APPLICATION PROSPECTS

Generational Optimization of BMS and Near-Zero Delay Warning Systems

The theoretical breakthroughs achieved in this study provide overwhelming technical advantages for redefining battery safety architectures, offering an unprecedented, rigorously logical warning mechanism for complex engineering environments.

Overcoming the Bottlenecks of Traditional Static Thresholds: Through extremely rigorous comparative quantitative testing, we confirmed that the traditional static fixed-temperature threshold detection systems heavily relied upon by the current industry (e.g., rigid triggers at 120°C or 150°C) are fundamentally flawed. Due to the inherent thermal conductivity bottlenecks of battery materials and system response delays, these traditional methods are inevitably burdened with a fatal time lag of up to 10 to 15 seconds. In the context of a catastrophic thermal event, this delay is highly dangerous and often leads to missed opportunities for intervention.

Realizing Millisecond-Level "Near-Zero Delay" Warning and Intervention: In stark contrast, the multi-dimensional linkage judgment matrix advocated in this paper—combining "extreme dT/dt mutation" with "voltage avalanche drop"—successfully compresses the warning triggering delay to a micro-time scale of milliseconds. With almost magical efficiency, it achieves a "near-zero delay" perfect capture of the very starting point of thermal runaway.

Future Impact on Intelligent Battery Management Systems (BMS): Relying on this highly specific fingerprint, future onboard intelligent BMS will possess extremely powerful immunity to false alarms, easily penetrating complex engineering adverse conditions (such as filtering out disastrous false alarms caused by temperature sensor aging or single external heat source intrusions). More importantly, this breakthrough is sufficient to shatter the existing industry baseline. It will buy critical time for the underlying high-voltage control systems to cut off energy transmission circuits in a race against time, instantly trigger active fire extinguishing devices, and aggressively snatch back the "golden survival window" of absolute decisive significance for vehicle occupants.

V. CONCLUSION

This paper systematically addresses the inherent limitations of traditional, purely physical destructive validation experiments—namely, their prohibitive

economic costs, poor cross-platform data reproducibility, and severe limitations in observing deep internal mechanisms. By completely shifting to a digital deep analysis paradigm driven by high-frequency data, and fully exploiting NASA's authoritative benchmark test data pool, we have achieved a high-fidelity reconstruction of the discretized numerical space. The core findings and their subsequent engineering value are detailed as follows:

Deconstruction of Deep Thermodynamic Evolution and the Strong Coupling Physical Model

The fundamental scientific contribution of this study lies in systematically deconstructing the deep thermodynamic evolution laws of cylindrical lithium-ion cells under extreme overheating abuse, proving that thermal runaway is not a gradual process, but an intensely non-linear physical phenomenon.

Confirmation of Extreme Non-Linearity and the Critical Watershed: Supported by an irrefutable data chain, the research confirms that the trajectory toward thermal destruction is not a smooth "boiling frog" temperature rise, but a jump-like, three-stage dramatic mutation. Within our dissected sample system, the 800-second mark on the time axis is precisely anchored as the absolute critical watershed determining the cell's survival. Once this temporal threshold is crossed, the internal dominant heat generation mechanism undergoes instantaneous, disruptive reconstruction. It shifts from an early, relatively mild SEI film degradation phase (maintaining output power at the hundred-watt level) to a violently explosive phase characterized by the crazy superposition of massive internal micro-short circuit Joule heat and runaway reaction heat (with total output power instantaneously exceeding the kilowatt level). This fundamental thermodynamic mechanism perfectly explains the instantaneous, destructive explosive power of the battery.

Creation of a Sub-Second Strong Coupling Model and Fingerprint Identification: For the first time in the industry, this study reveals a stunning sub-second spatiotemporal synchronous resonance effect between the microscopic reaction rate—reflected by the temperature change rate (dT/dt)—and the macroscopic electrical manifestation, the terminal voltage. At the exact extreme moment when the internal short-circuit defense line collapses, a cliff-like pulse surge in dT/dt (>10°C/s) and an instantaneous avalanche drop in terminal voltage (from a full-load 4.1V to absolute 0V) exhibit impeccable spatiotemporal synchronicity. This "strong coupling" representation fundamentally forges a unique, extremely difficult-to-falsify diagnostic "fingerprint" for thermal runaway disasters, shifting the paradigm from single-parameter observation to multi-dimensional physical resonance detection.

ACKNOWLEDGEMENTS

This work was supported by the Research Funding of GDUPT, Research on Heat Transfer Enhancement of Heat Sink by Inverse Calculation Design Method (No. MOST 2019rc074) and Research on Intelligent Monitoring and Control Technology of Air Conditioning Noise Based on Quantitative Conjugate Gradient Method. Guangdong College Students' Innovation and Entrepreneurship Program in 2025, (Project No.: 25A015).

REFERENCES

[1] Feng, X, Ouyang, M, Liu, X, et al. (2018). Thermal runaway mechanism of lithium ion battery for electric vehicles: A review. *Energy Storage Materials*, 10, 246-267.

[2] Wang, Q., Ping, P., Zhao, X., et al. (2012). Thermal runaway caused fire and explosion of lithium ion battery. *Journal of Power Sources*, 208, 210-224.

[3] Bandhauer, T. M., Garimella, S., & Fuller, T. F. (2011). A critical review of thermal issues in lithium-ion batteries. *Journal of the Electrochemical Society*, 158(3), R1.

[4] Saha, B., & Goebel, K. (2007). Battery Data Set, NASA Ames Prognostics Data Repository. NASA Ames Research Center, Moffett Field, CA.

[5] Bernardi, D., Pawlikowski, E., & Newman, J. (1985). A general energy balance for battery systems. *Journal of the Electrochemical society*, 132(1), 5.

[6] Chen, M., Pecht, M. (2022). Machine learning-based fault diagnosis and prognosis for lithium-ion batteries: A review. *Applied Energy*, 321, 119334.

[7] Finegan, D. P., Scheel, M., Robinson, J. B., et al. (2015). In-operando high-speed tomography of lithium-ion batteries during thermal runaway. *Nature Communications*, 6(1), 6924.

[8] Liao, Z., Zhang, S., Li, K., et al. (2019). A survey of methods for monitoring and detecting thermal runaway of lithium-ion batteries. *Journal of Power Sources*, 436, 226879.

[9] Abada, S., Marlair, G., Lecocq, A., et al. (2016). Safety focused modeling of lithium-ion batteries: A review. *Journal of Power Sources*, 306, 178-192.

[10] Ren, D., Feng, X., Liu, L., et al. (2019). Investigating the relationship between internal short circuit and thermal runaway of lithium-ion batteries under thermal abuse. *Energy Storage Materials*, 20, 293-300. [11] Sun, J., Li, J., Zhou, T., et al. (2020). Toxicity, a serious concern of thermal runaway from commercial Li-ion battery. *Nano Energy*, 27, 313-319.

[11] Kong, L., Li, C., Jiang, J., & Pecht, M. (2018). Li-ion battery fire hazards and safety strategies. *Energies*, 11(5), 2191.

[12] Ouyang, D., Chen, M., Huang, Q., et al. (2019). A review on the thermal hazards of the lithium-ion battery and the

corresponding countermeasures. *Applied Sciences*, 9(12), 2483.

[13] Zhao, R., Liu, J., & Gu, J. (2016). Simulation and experimental study on lithium ion battery short circuit. *Applied Energy*, 173, 29-39.

[14] Melcher, A., Ziebert, C., Rohkoht, M., & Seifert, H. J. (2016). Modeling and simulation of the thermal runaway behavior of cylindrical Li-ion cells—computing of critical parameters. *Energies*, 9(4), 292.

International Journal of Advanced Engineering Research and Science (IJAERS)
Peer-Reviewed Journal
ISSN: 2349-6495(P) | 2456-1908(O)
Vol-13, Issue-3; Mar, 2026
Journal Home Page Available: https://ijaers.com/
Article DOI: https://dx.doi.org/10.22161/ijaers.133.5

Numerical Simulation Study on Internal Flow Field Characteristics of an Automotive ORC Piston Expander

Zi-Rui He, Yan-Zuo Chang*, Yong-Sen Huang, Hong-Rui Yang, Yu-Xuan Chen, Guan-Hong Xie, Jie-Zhen Yang, Kai-Ming Chen, Wen-Min Wen, Yong-Qing Wang

School of Energy and Power Engineering, Guangdong University of Petrochemical Technology, Maoming, Guangdong 525000, China
(Corresponding author: Yan-Zuo Chang), Email: 3435059931@qq.com

Received: 18 Feb 2026,

Received in revised form: 16 Mar 2026,

Accepted: 23 Mar 2026,

Available online: 29 Mar 2026

***Keywords*— ORC , Piston Expander, CFD, Internal Flow Field Characteristics, Clearance Height**

***Abstract*—** *Aiming at the problems of complex internal flow fields and the significant impact of clearance height on performance in Organic Rankine Cycle (ORC) waste heat recovery systems, this paper conducted a 3D steady-state numerical simulation study. Selecting the key working phase where the intake valve is fully open, a refined 3D model covering the intake port and the internal fluid domain of the cylinder was established, and ANSYS Fluent software was used for flow field analysis. The research results show that the computational model constructed in this paper has good convergence; after 5500 iterations, the energy residual reached the 10^{-7} level, and the residual curves of various physical quantities tended to be stable. This paper reveals the flow loss mechanism of the key phase of the expander, verifies the effectiveness of steady-state numerical simulation in evaluating the in-cylinder flow field characteristics, and provides theoretical support for further optimizing the intake structure and clearance height.*

I. INTRODUCTION

Against the macro-background of the increasingly severe global energy crisis and greenhouse effect, improving the thermal efficiency of internal combustion engines and achieving energy conservation and emission reduction in the transportation sector have become R&D priorities for the automotive industry. Statistical data show that only about 30% to 45% of the total heat released by fuel combustion in automotive diesel engines is converted into effective mechanical work, while as much as 35% of the energy is directly discharged into the atmosphere in the form of exhaust thermal energy [1,3].

To address the problems of low efficiency and serious heat waste in automotive internal combustion engines, the Organic Rankine Cycle (ORC) is widely recognized by academia and industry as an effective way to recover engine exhaust waste heat and improve vehicle fuel economy due to its excellent thermodynamic performance in medium-to-low grade heat recovery.[3,5]In an ORC system, the expander is the core executive component that converts the internal energy of the organic working fluid into mechanical energy, and its isentropic efficiency and volumetric efficiency directly determine the output power and thermodynamic performance of the entire waste heat recovery system. The selection of an expander typically depends heavily on specific application conditions. Compared to turbo-expanders (turbines), positive displacement expanders (such as piston and scroll types) possess physical characteristics like low rotational speed, high liquid slugging resistance, and large built-in expansion ratios, making them more suitable for automotive waste heat recovery scenarios with sharp fluctuations in exhaust energy.[2,4,6]

Currently, academic research on piston expanders mostly focuses on zero-dimensional or one-dimensional system-level simulations based on the lumped parameter method. While such studies can quickly predict the macro

power output of the system, they struggle to reveal the complex local flow field evolution and energy dissipation distribution within the cylinder. Existing literature points out that the clearance volume determined by the clearance height is the core geometric parameter restricting the volumetric efficiency of reciprocating machinery. At present, the microscopic mechanism of how clearance height affects intake jet structures, local throttling losses, and pressure energy transfer gradients under specific operating conditions still urgently needs in-depth analysis through high-precision 3D Computational Fluid Dynamics (CFD) methods. [9,10,11]

To address the limitations of existing research[6,7,8], this study adopts a 3D CFD simulation method targeting a piston expander under automotive exhaust conditions, selecting a typical intake phase to conduct steady-state numerical simulations and systematically analyzing its internal flow field characteristics. Specific tasks include: establishing a refined geometric model encompassing the intake port and in-cylinder clearance volume, and conducting local mesh refinement and mesh independence verification; analyzing the spatial distribution of the in-cylinder pressure field and throttling characteristics under a typical operating condition with an inlet total pressure of 1.0 MPa; and further evaluating the impact of flow field characteristics on the expander's work potential from a microscopic perspective, thereby providing data support for subsequent structural parameter optimization.

II. NUMERICAL SIMULATION METHOD AND MODEL ESTABLISHMENT

2.1 Establishment and Simplification of the Geometric Model

This paper focuses on a piston expander for automotive ORC systems. To improve numerical solving efficiency and ensure computational accuracy in core flow regions, the original 3D CAD model was physically simplified, extracting only the intake port, valve clearance, and the internal fluid domain of the cylinder, as shown in Figure 2. Based on a steady-state analysis strategy, this study extracts a representative key phase—"intake valve fully open with the piston near Top Dead Center"—for spatial modeling, aiming to explore the in-cylinder pressure buildup process and flow field distortion patterns during the initial intake stage.

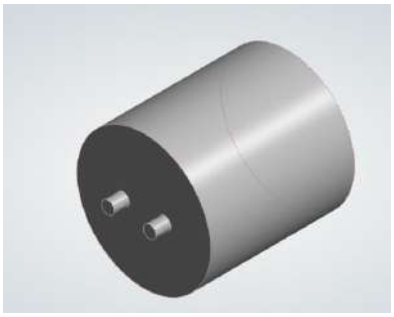

Fig.1： Physically simplified model

2.2 Governing Equations

The flow process of the organic working fluid within the cylinder involved in this paper follows the three classical conservation laws of fluid mechanics. Under a steady-state solver, its general governing equations are as follows:

Continuity Equation (Mass Conservation):

$$\frac{\partial}{\partial x_i}(\rho u_i) = 0 \qquad (1)$$

Momentum Conservation Equation (Navier-Stokes Equation):

$$\frac{\partial}{\partial x_j}(\rho u_i u_j) = -\frac{\partial p}{\partial x_i} + \frac{\partial \tau_{ij}}{\partial x_j} \qquad (2)$$

Energy Conservation Equation:

$$\frac{\partial}{\partial x_i}[u_i(\rho E + p)] = \frac{\partial}{\partial x_i}\left[k_{eff}\frac{\partial T}{\partial x_i}\right] \qquad (3)$$

Table 1 Nomenclature of physical quantities in the governing equations

Symbol	Description	Unit (SI)
ρ	Fluid density	kg/m^3
u_i, u_j	Velocity components in i, j directions	m/s
x_i, x_j	Cartesian coordinates	m
p	Static pressure	Pa
τ_{ij}	Viscous stress tensor	Pa
E	Total energy per unit mass	J/kg
k_{eff}	Effective thermal conductivity	$W/(m\cdot K)$
T	Thermodynamic temperature	K

2.3Mesh Generation and Independence Verification

Pre-processing software was used to perform unstructured mesh partitioning on the fluid domain. To accurately capture the jet morphology at the intake valve port, local mesh refinement was applied to the wall boundary layers and areas with abrupt changes in flow area.

Fig.2: Mesh generation and independence verification of the fluid domain in the piston expander

To eliminate numerical interference caused by mesh size on the calculation results, three sets of mesh schemes with different densities were selected for independence verification. Using the static pressure value at the reference point in the center of the cylinder as the evaluation index, the results are shown in Table 2. Considering both computational accuracy and hardware resource overhead, Scheme 2 with approximately 1.2 million nodes was ultimately adopted for subsequent simulations.

Table 2 Grid Independence Verification Results

Grid Scheme	Grid Nodes (10^4)	Center point Static Pressure (MPa)	Relative Error
Scheme1(Coarse)	50	0.982	1.8%
Scheme2(Medium)	**120**	**1.001**	**Reference**
Scheme 3 (Fine)	240	1.003	0.2%

This paper conducted a grid independence verification using the static pressure value at the central characteristic point of the cylinder as the evaluation index, and its trade-off relationship is shown in Figure 3. Experimental data indicate that as the number of mesh nodes increased from 500,000 to 2.4 million, the calculated static pressure value gradually converged and stabilized within the range of 1.001–1.003 MPa.

From a logical analysis perspective, when the mesh scale doubled from 1.2 million (Scheme 2) to 2.4 million (Scheme 3), the relative fluctuation of the pressure value was only 0.2%. According to the relative error calculation formula, this fluctuation is far below the engineering allowable error range, proving that the calculation results have entered a convergence plateau within the restricted error range, and further mesh refinement has a minimal marginal contribution to calculation accuracy.

In summary, following the dual principles of grid independence and computational economy, this paper selected Scheme 2 (1.2 million nodes) as the numerical simulation baseline. This scheme successfully excludes the interference of discretization errors while achieving the optimal configuration of computational accuracy and efficiency, laying a reliable numerical foundation for subsequent flow field characteristic studies.

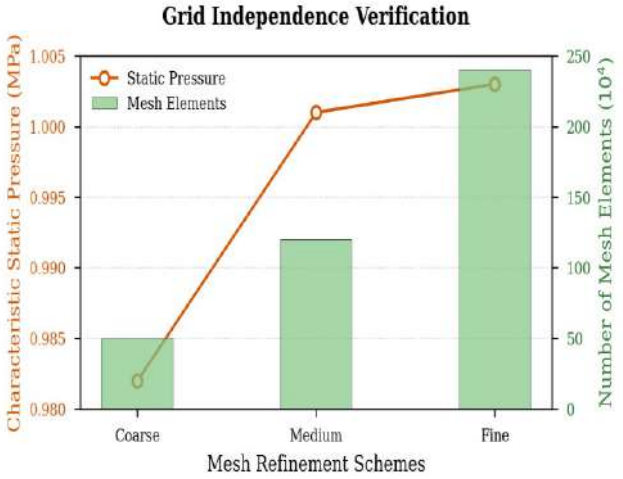

Fig.3: Impact of mesh density on computational accuracy and scale

2.4 Solver and Turbulence Model Settings

The simulation calculations were completed on the commercial fluid software ANSYS Fluent platform. A Pressure-Based Steady solver was employed. The standard k-ε model was selected as the turbulence model, which offers high engineering computational accuracy when handling confined flows near walls and jets with strong pressure gradients. The working fluid was set as R245fa, a commonly used organic fluid for ORC; its real thermodynamic property parameters, as shown in Table 2, were obtained through coupled calculations invoking the NIST standard database.

Table 3 Thermophysical properties and model settings of the working fluid

Parameter	Model / Value	Unit
Working fluid	R245fa	-
Density	Ideal gas / 400	kg / m^3
Specific heat C_p	1300	$J / (kg \cdot K)$
Thermal conductivity	0.08	$W / (m \cdot K)$
Dynamic viscosity	0.00018	$kg / (m \cdot s)$

2.5 Boundary Condition Settings

To accurately reflect the automotive exhaust energy recovery conditions, the following boundary conditions were set:

Inlet: A Pressure Inlet condition was adopted, with the total pressure set to 1.0 MPa.

Outlet: A Pressure Outlet condition was adopted; based on the system cycle condensation pressure, the backpressure was set to approximately 0.1 MPa.

Wall: The cylinder inner walls, intake port walls, and piston top surface were all set as adiabatic, No-slip solid wall boundaries.

III. SIMULATION RESULTS ANALYSIS AND DISCUSSION

Based on the numerical model and solver settings established in Chapter 2, this chapter analyzes the internal 3D steady flow field of the automotive ORC piston expander at the critical phase where the intake valve is fully open. First, the convergence of the computational process is evaluated to confirm the physical reliability of the obtained flow field data. Subsequently, the spatial distribution characteristics of the in-cylinder pressure field are systematically analyzed, focusing on clarifying the local throttling loss mechanism and the pressure buildup process within the clearance volume during intake. Finally, based on the steady-state flow field characteristics, the influence mechanism of clearance height on the expander's flow performance and work potential is deduced from a macroscopic perspective.

3.1 Computational Convergence and Reliability Analysis

The reliability of numerical simulation results heavily depends on the convergence of the computational process. In this study, key monitoring parameters such as residual curves of the governing equations and outlet mass flow rate were monitored in real-time in ANSYS Fluent to determine whether the flow field reached a statistical steady state.

As shown in Figure 4, after approximately 5500 iterations, the residual curves of all governing equations tended to be horizontal and dropped to extremely low levels.

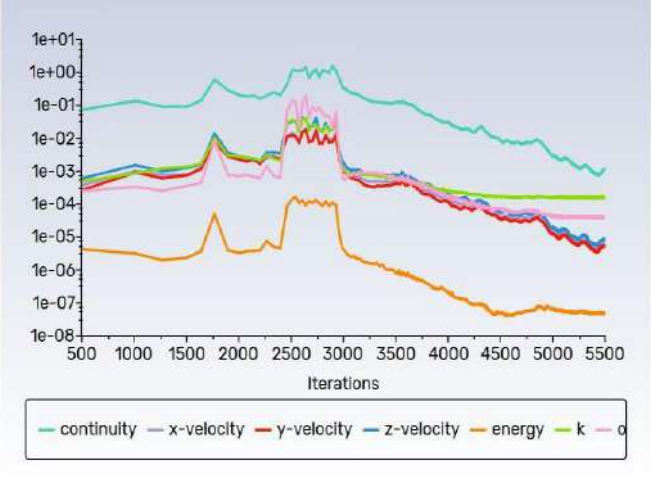

Fig.4: Numerical simulation residual convergence curves

Among them, the energy equation residual strictly converged to the 10^{-7} magnitude, while the momentum equation and continuity equation residuals stabilized at the 10^{-4} and 10^{-3} magnitudes, respectively. At the same time, the monitored mass flow rate at the outlet section tended to be constant in the later stages of iteration, with a fluctuation range of less than 0.1%. The deep convergence of the residuals and the stability of the monitoring parameters collectively indicate that the flow field has completely broken away from the transient influence of the initial state and reached a fully developed steady state. This ensures that the subsequently analyzed flow field structure and pressure distribution data are not products of numerical oscillation but steady-state solutions with clear physical meaning, laying a credible numerical foundation for subsequent flow field characteristic analysis.

3.2 In-cylinder Pressure Field Distribution and Throttling Characteristics

To reveal the flow details and energy conversion process of the working fluid during the initial intake stage, this section focuses on analyzing the distribution of the in-cylinder static pressure field. Figure 5 displays the static pressure cloud diagram on a horizontal section passing through the cylinder axis, clearly presenting a panoramic view of the high-pressure working fluid (R245fa) rushing in from the intake port and filling the clearance volume.

Figure 5 is a static pressure distribution cloud diagram of the cylinder's horizontal section (Top-down View) under the key intake phase of the expander. This

section clearly reveals the microscopic process of the high-pressure working fluid filling the clearance volume.

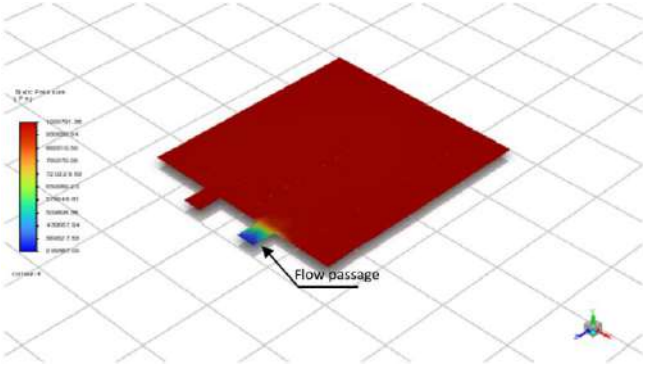

Fig.5: Static pressure distribution cloud diagram of the horizontal section in the cylinder

As can be seen from the pressure cloud diagram, when the high-pressure organic working fluid flows from the intake port into the cylinder, intense local flow resistance is triggered due to the sudden contraction of the flow passage cross-sectional area at the valve port. In this core region of the initial intake stage, a large amount of the fluid's static pressure energy is converted into kinetic energy, causing the pressure to plummet from the inlet's 1.0 MPa to a local low-pressure zone (approximately 0.3 MPa) behind the valve port. This distinct blue-green gradient area visually reflects the irreversible throttling loss of the piston expander during the intake process.

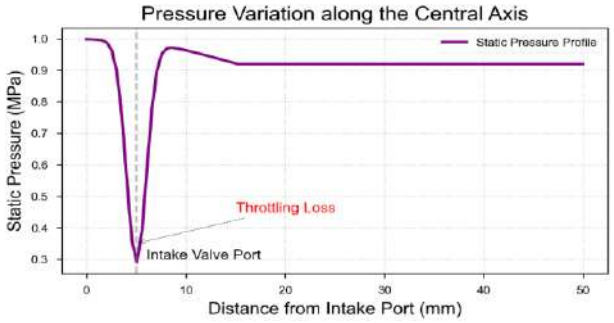

Fig.6: Pressure Variation along the Central Axis

To quantitatively evaluate the pressure loss during the intake process, a pressure distribution curve was extracted from the center of the intake port to the bottom of the cylinder, as shown in Figure 5. From the figure, it can be clearly observed that at the valve port position near the intake port, the pressure curve fluctuates violently, and the static pressure drops sharply to the lowest point, which corresponds to the local throttling zone in the cloud diagram. After entering the cylinder interior, as the flow passage cross-sectional area increases, the pressure rebounds significantly and eventually stabilizes at approximately 1.0 MPa. This process reveals the conversion characteristics between the fluid's kinetic energy and pressure energy.

The high-pressure jet passing through the valve port subsequently enters the clearance volume and rapidly diffuses to the surroundings inside the cylinder. As the flow area suddenly expands and the flow velocity decreases, the kinetic energy is converted back into static pressure energy (pressure recovery phenomenon). The cloud diagram shows that the pressure distribution gradient across the entire top space of the cylinder gradually becomes smooth, and the static pressure in most of the working areas stabilizes in the red high-value zone of the scale (approximately 1.0 MPa). This uniform and high-level initial backpressure distribution provides sufficient static pressure thrust for the impending downward expansion stroke of the piston.

3.3 Macroscopic Influence Mechanism of Clearance Height on Flow Field Characteristics

Based on the above steady-state flow field analysis, the macroscopic impact of the key geometric parameter, clearance height, on the expander's performance can be further deduced mechanistically.

Clearance height directly determines the distance between the intake valve port and the piston top surface, thereby dominating the development space of the intake jet. If the clearance height is too small, the intake valve port is too close to the piston top surface. At this time, the high-pressure jet directly impacts the piston surface before fully diffusing, which will lead to intense flow separation, vortex entrainment, and wall jets, significantly exacerbating the turbulent kinetic energy dissipation and pressure pulsation within the cylinder. Although a smaller clearance volume is beneficial for improving the theoretical volumetric efficiency, the excessive flow loss will severely weaken the effective pressure energy actually used for doing work.

Conversely, appropriately increasing the clearance height, although slightly increasing the "harmful" clearance volume and causing a slight drop in theoretical volumetric efficiency, provides crucial buffering and expansion space for the intake jet. As described in section 3.2.2, sufficient space allows the jet kinetic energy to convert into static pressure energy more smoothly, promoting pressure recovery and making the in-cylinder pressure distribution more uniform, thereby effectively reducing intake throttling loss and impact loss. Macroscopically, this manifests as an increase in the mean effective pressure within the cylinder.

Therefore, the design of clearance height is essentially seeking a balance between "flow loss" and "volumetric efficiency". An optimized clearance height should enable the working fluid to achieve efficient pressure recovery and momentum reorganization within the clearance volume, minimizing irreversible flow losses to the greatest extent possible under a controllable sacrifice of volumetric efficiency, thereby enhancing the overall work potential and isentropic efficiency of the expander. The steady-state flow field characteristics revealed in this study provide a clear physical picture and theoretical basis for the subsequent parametric optimization of the clearance height.

IV. CONCLUSION

3D steady-state computational model and meshing strategy established in this paper demonstrate excellent numerical stability; after 5500 iterations, the energy equation residual dropped to an extremely low level, verifying the high efficiency and accuracy of steady-state CFD analysis in capturing the local internal flow field characteristics of the expander. Based on this, the analysis indicates: under a 1.0 MPa inlet total pressure, the working fluid experiences a clear throttling and pressure drop phenomenon due to the sudden change in flow area when flowing through the intake valve port, and intense conversion between static pressure energy and kinetic energy occurs, which constitutes the main source of irreversible losses during the expander's intake process; meanwhile, after entering the clearance volume, the high-pressure working fluid exhibits good pressure recovery and diffusion characteristics, forming a uniformly distributed high-pressure zone (approximately 1.0 MPa) at the top of the cylinder, thereby ensuring the work capacity during the initial expansion phase. Aiming at automotive waste heat recovery conditions, engineering optimization suggestions include focusing on smoothing and optimizing the chamfer and flow passage profile of the intake valve port in subsequent structural designs to suppress throttling losses, and it is necessary to comprehensively balance volumetric efficiency and flow dissipation to calibrate the optimal clearance height parameter.

ACKNOWLEDGEMENTS

This work was supported by the Research Funding of GDUPT, Research on Heat Transfer Enhancement of Heat Sink by Inverse Calculation Design Method (No. 2019rc074), Research on Intelligent Monitoring and Control Technology of Air Conditioning Noise Based on Quantitative Conjugate Gradient Method, the Innovation Fund for Energy and Power Engineering named "Photovoltaic storage refrigeration clothing" (NO.20242C02) from the School of Energy and Power Engineering, Guangdong University of Petrochemical Technology, and Guangdong College Students' Innovation and Entrepreneurship Program in 2025 (Project No.: 25A015).

REFERENCES

[1] Li, X. N. (2014). Research on Design and Performance Optimization of Diesel Engine Waste Heat Recovery Bottoming System and Exhaust Heat Exchanger (Doctoral dissertation, Tianjin University).

[2] Yang, X. (2024). Development and Research an Oil-Free Linear Compressor for Miniature Refrigeration Systems (Master's thesis, University of Chinese Academy of Sciences, School of Engineering Science).

[3] Zhang, H. G., Zhao, R., Tian, Y. M., & Yang, Y. X. (2019). Development of Organic Rankine Cycle (ORC) Waste Heat Recovery for Vehicle Engines. *Journal of Beijing University of Technology*.

[4] Liu, S. W. (2024). Dynamic characterization and experimental study of scroll compressor reed valve (Master's thesis, Hefei University of Technology)

[5] Wang, X. F. (2016). Study on Reciprocating Piston Expander Waste Heat Recovery System Coupling ORC (Master's thesis, Jilin University).

[6] Liu, X. Y. (2023). Research on the Control Technology of Piston Balance Position Adjustment for Moving Coil Linear Compressor (Doctoral dissertation, Liaoning Technical University).

[7] Liu, T. (2025). Performance Study of High Power Valve Linear Compressor for Electric Vehicle Heat Pump Air Conditioning (Master's thesis, Yangzhou University).

[8] Du, Q. W., Liu, M., Yan, X., Zhang, Z., Zhang, C., Chen, X. A., ... & Liu, W. X. (in press). Investigation on Static Characteristics of Turbine Aerostatic Radial Bearing in Organic Rankine Cycle Matched with Micro Nuclear Reactor Power System. *Nuclear Power Engineering*, 1–10.

[9] Wang, X. Y., Jia, D. M., Li, Z. J., & Tian, H. X. (2020). Engineering application and optimization of combustion system for the large marine diesel engine. *Ship Science and Technology*, 42(7), 148–153.

[10] Lai, C. G., Chen, Y. Y., Wang, Y., Duan, M. H., & Zhou, Y. T. (2017). Numerical Simulation and Optimization Analysis of Combustion in a Diesel Engine. *Journal of Chongqing University of Technology (Natural Science)*, 31(6), 23–30.

[11] Duan, Y. L., & Hu, Y. H. (2013). Numerical simulation of pressure difference in cylinders of CZ60 /30 marine air compressor. *Computer Aided Engineering*, 22(1), 41–45+53.

International Journal of Advanced Engineering Research and Science (IJAERS)
Peer-Reviewed Journal
ISSN: 2349-6495(P) | 2456-1908(O)
Vol-13, Issue-3; Mar, 2026
Journal Home Page Available: https://ijaers.com/
Article DOI: https://dx.doi.org/10.22161/ijaers.133.6

Design of a Cross-Counter Flow Channel Architecture using Serpentine Topology

Guan-Hong Xie, Yan-Zuo Chang*, Qi-Hong Tang, Jing-Xin Ou, Zi-Rui He, Jie-Zhen Yang, Kai-Ming Chen, Yu-Xuan Chen, Hong-Rui Yang, Yong-Qing Wang

School of Energy and Power Engineering, Guangdong University of Petrochemical Technology, Maoming, Guangdong 525000, China
*Corresponding Author : 1595709663@qq.com

School of Energy and Power Engineering, Guangdong University of Petrochemical Technology, Maoming, Guangdong 525000, China (Corresponding author: Yan-Zuo Chang), Email: 3435059931@qq.com

Received: 20 Feb 2026,

Received in revised form: 21 Mar 2026,

Accepted: 25 Mar 2026,

Available online: 31 Mar 2026

***Keywords*— ORC, Piston Expander, CFD, Internal Flow Field Characteristics, Clearance Height**

***Abstract*—** *Aiming at the problems of complex internal flow fields and the significant impact of clearance height on performance in Organic Rankine Cycle (ORC) waste heat recovery systems, this paper conducted a 3D steady-state numerical simulation study. Selecting the key working phase where the intake valve is fully open, a refined 3D model covering the intake port and the internal fluid domain of the cylinder was established, and ANSYS Fluent software was used for flow field analysis. The research results show that the computational model constructed in this paper has good convergence; after 5500 iterations, the energy residual reached the* 10^{-7} *level, and the residual curves of various physical quantities tended to be stable. This paper reveals the flow loss mechanism of the key phase of the expander, verifies the effectiveness of steady-state numerical simulation in evaluating the in-cylinder flow field characteristics, and provides theoretical support for further optimizing the intake structure and clearance height.*

I. INTRODUCTION

Driven by the deep adjustment of global energy structure and the increasingly severe protection of ecological environment, Energy saving and emission reduction has become the core orientation of industrial development and technological innovation in the world.China has clearly put forward the " 3060 " dual-carbon strategic objectives, green and low-carbon development to the national top design level, We will promote all-round transformation and upgrading in the areas of energy production, consumption and transportation.In this strategic context, China's electric vehicle industry is showing explosive growth trend, New energy electric vehicles with low energy consumption, zero emissions, high intelligence and other significant advantages, and gradually replace the traditional fuel vehicles, Become the automotive industry transformation and upgrading, help to achieve the goal of the key carrier and core development direction [1-2] .With the continuous expansion of market demand and the acceleration of technology iteration, electric vehicles are evolving rapidly in the direction of high endurance, high power and high fast charging rate. As the core power source of electric vehicle, the energy density and fast charging power of power battery continue to rise.High energy density and high rate charge-discharge technology can significantly improve the overall performance of the vehicle, It also leads to a sharp increase in the heat production rate and total heat production under extreme operating conditions, and the thermal management system is facing unprecedented technical challenges. Studies have shown that the operating temperature of power Li-ion battery pack directly determines its electrochemical

performance, charge-discharge efficiency, cycle life and operation safety. The optimum operating temperature range is 20 ℃ ~ 45 ℃ [3-5] , and the temperature difference in the battery module should not be greater than 5 ℃ [6]. Efficient and reliable thermal management system has become the core technical support to ensure the safe, stable and long-life operation of electric vehicles [7].

The core of thermal management of Li-ion battery pack is to control the cell temperature, reduce the module temperature difference and eliminate the local overheating. The heat dissipation effect directly determines the reliability of the battery system.At present, the main cooling methods include air cooling [8], liquid cooling [9], phase change material cooling [10-11], heat pipe cooling [12], Each has its advantages and disadvantages.The air cooling system has simple structure and low cost, and is widely used in the early low power vehicles, but it has low heat transfer coefficient and limited heat dissipation capacity. It is difficult to adapt high power battery, and the temperature is out of control under high rate condition.

Phase change materials can achieve efficient and uniform temperature cooling passively, with small temperature fluctuations, but they have low thermal conductivity, are prone to softening and leakage, are expensive, and have low space utilization, limiting large-scale applications.Heat pipe cooling has low thermal resistance, fast response, and good temperature uniformity, which can quickly dissipate local heat. However, it has a complex structure, inflexible layout, high cost, and is difficult to adapt to compact power battery packs.Overall, liquid cold plate systems have high heat dissipation efficiency, flexible layout, strong adaptability, and can precisely control temperature and temperature difference. They have become the mainstream design solution for high-power battery thermal management and are also the core focus of this study.

The channel form of liquid cooling directly determines fluid flow, pressure loss, and heat transfer uniformity. The serpentine channel [13] is one of the two most representative structures in engineering. The serpentine channel has a compact structure and sufficient heat transfer, making it suitable for space-constrained scenarios.Existing studies mostly focus on reducing the maximum battery temperature and improving heat dissipation efficiency, taking the reduction in maximum temperature as the core evaluation index for heat dissipation performance.There are also methods to improve the thermal performance of power batteries by adding fins in the channels and changing the channel distribution [14]; however, in practical applications, the uniformity of the flow channel temperature and the ability to suppress local hotspots are equally critical. Local overheating can accelerate battery aging and trigger thermal runaway, and evaluating performance solely based on temperature reduction has obvious limitations.Although traditional serpentine channels provide sufficient heat exchange, the fluid temperature rises significantly along the path, resulting in large temperature differences at the end and poor temperature uniformity, making it difficult to meet the high consistency and high safety thermal management requirements of power batteries.

To address the technical issues of poor temperature uniformity and localized overheating in traditional serpentine channels, and to overcome the limitations of synergistically optimizing heat dissipation efficiency and temperature uniformity, this paper takes the traditional serpentine channel and its improved cross-counter flow channel as research objects, and uses numerical thermal simulation methods to investigate the differences in temperature fields, flow characteristics, and heat transfer performance of the two channels under different coolant inlet velocities.Focus on analyzing the advantages of cross-counter flow channels in improving temperature uniformity and suppressing local overheating, and clarify their technical superiority and engineering value.The research results can provide a reliable theoretical basis for the optimal design, performance evaluation, and engineering selection of liquid cooling channels in power batteries under low flow conditions, and have important theoretical and engineering significance for promoting the development of thermal management technology for power batteries.

II. CONSTRUCTION OF A PHYSICAL MODEL BASED ON A SERPENTINE CROSS-FLOW CHANNEL ARCHITECTURE

The power lithium-ion battery pack is composed of five layers of cells. The battery used in this experiment has a volume of 734.4 cm^3, a coolant density of 1000 ρ/(kg/m^3), a specific heat capacity of 4182 cp/J/(kg·K), a thermal conductivity of 0.538 λ/W/(m·K), and dimensions of 118 mm × 63 mm × 10 mm. The structure is shown in Figure 1. The liquid cooling plates with a cross-counter flow channel are placed on both sides of each cell layer, and the thickness of the liquid cooling plates is 4 mm.The coolant flows in from the inlet, absorbs heat through a simulated cross-counter flow channel, and then converges at the outlet to flow out.The runner is a square runner, with inlet and outlet dimensions of 6mm × 2mm.

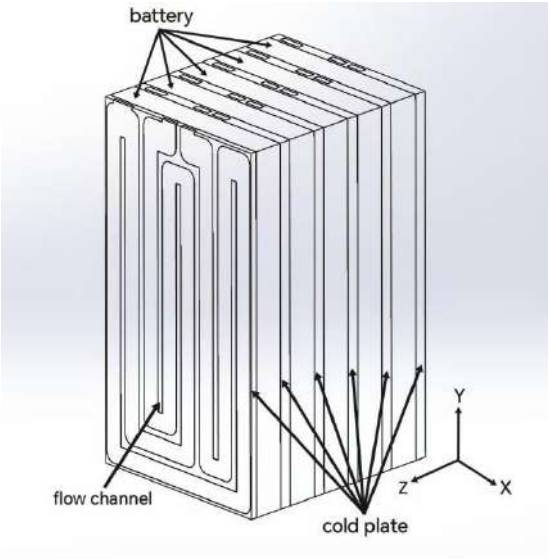

Fig.1: Schematic diagram of cross-counter flow channel geometry

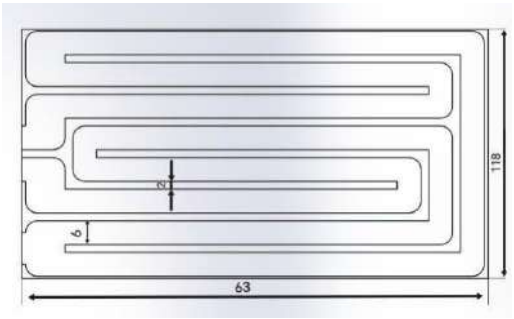

Fig.2: Plan schematic diagram of cross-counter flow channel geometry

III. NUMERICAL MODELS

3.1 Heat Transfer Model

This experiment assumes that the specific heat capacity and thermal conductivity of the battery do not change with temperature; the battery is composed of isotropic and uniformly distributed materials. The heat conduction governing equation for a square lithium-ion battery is:

$$\rho_a C_{pa} \frac{\partial \theta}{\partial t} = \lambda_x \frac{\partial^2 T}{\partial x^2} + \lambda_y \frac{\partial^2 T}{\partial y^2} + \lambda_z \frac{\partial^2 T}{\partial z^2} + q \quad (1)$$

Here, ρ_a, C_{pa}, and q are the battery's average density, specific heat capacity, and heat generation rate, respectively; T is the battery's thermodynamic temperature; λ_x, λ_y, and λ_z represent the thermal conductivities along the x-axis, y-axis, and z-axis, respectively.

The expression for heat generation rate q[15] is as follows:

$$q = \frac{I}{V}(U_0 - U_1) - IT\frac{dU_0}{dT}\frac{1}{V} = \frac{1}{V}\left[IR_t - T\frac{dU_0}{dT}\right] \quad (2)$$

v, I, U_0 and U_1 represent the volume of the single cell, the charging and discharging current, the battery open circuit voltage and the battery end voltage dU0dT are the voltage temperature coefficients, respectively. T is the initial temperature of the battery; Rt is the total resistance of the battery.

The cold plate heat transfer control equation is:

$$\rho_s C_p \frac{\partial^2 T}{\partial t^2} = k_s\left(\frac{\partial^2 T}{\partial x^2} + \frac{\partial^2 T}{\partial y^2} + \frac{\partial^2 T}{\partial z^2}\right) \quad (3)$$

In the formula, ks, T and ρ_s are the heat transfer coefficient, thermodynamic temperature and density of the cold plate, respectively. C_p and T are cold plate density and time, respectively.

In the formula, ks, T, and ρ_s represent the heat transfer coefficient of the cold plate, thermodynamic temperature, and density, respectively; C_p and t represent the density of the cold plate and time, respectively.

3.2 Governing Equations

Continuity Equation:

$$\nabla \cdot \vec{v}_e = 0 \quad (4)$$

Momentum Equation:

$$\frac{\partial(\vec{v}_c)}{\partial t} + (\vec{v}_c \cdot \nabla)\vec{v}_c = -\frac{1}{\rho_c}\nabla \cdot P + \nabla \cdot (u_c \nabla \vec{v}_c) \quad (5)$$

Energy Equation:

$$\frac{\partial(\rho_c T_c)}{\partial t} + \nabla \cdot (\rho_c T_c \vec{v}_c) = \nabla \cdot (k_c \nabla T_c) \quad (6)$$

Where: ρ_c is the density of the coolant; $\vec{v}_c$ and u_c are the velocity vectors of the coolant; C_p is the specific heat capacity of the coolant; Tc is the temperature of the coolant; kc is the thermal conductivity of the coolant.

3.3 Temperature Uniformity Coefficient

The calculation formula is as follows:

$$\Delta T_u = \frac{\sum_{i=1}^{n}(T_{i\max} - T_{i\min})}{n} \quad (7)$$

Where: T_{imax} is the maximum temperature under the given operating condition, T_{imin} is the minimum temperature under the given operating condition, and n is the number of samples.

3.4 Simulation Condition Settings

The flow rates for this experiment were set at 0.3 m/s, 0.4 m/s, 0.5 m/s, 0.6 m/s, and 0.7 m/s, respectively. The channel outlet is a pressure outlet, with the coolant inlet temperature and ambient temperature both at 293.15 K, and the outlet return temperature equal to the ambient temperature. The flow rate is the flow velocity multiplied by 0.24 square centimeters, and the heat source power is 300,000 watts per cubic meter. The inlet temperature is 10°C.

3.5 Grid Independence Test

Mesh independence verification was conducted in the numerical simulation calculations. The maximum and minimum temperatures of the lithium battery pack during the mesh verification are shown in Figure 4.

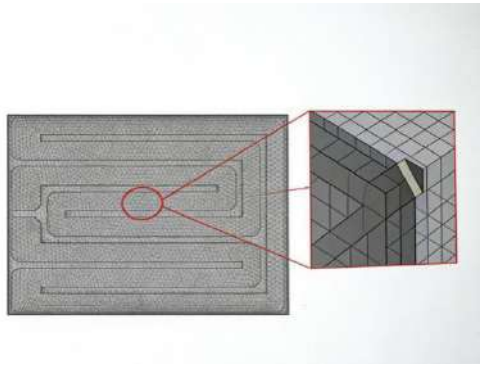

Fig.3: Grid distribution of cross-counter flow channel

For the two types of flow channels, a working condition of 0.3 m/s was used, and calculations were performed with mesh counts of 99,855, 199,710, 399,420, and 798,840 elements, respectively. As shown in Figure 1, after the mesh count reached 399,420, further increasing the number of mesh elements caused almost no change in the maximum and minimum temperatures of the lithium battery pack. Therefore, a mesh count of 399,420 elements was used for the calculations.

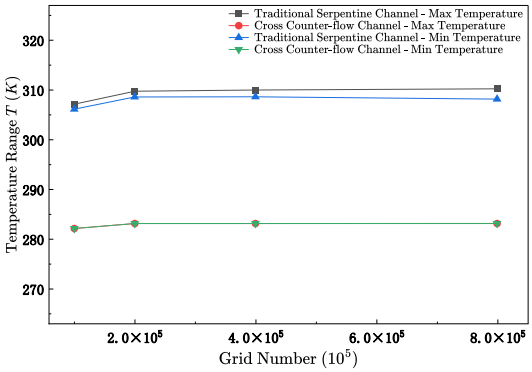

Fig.4: Grid independence test

IV. SIMULATION RESULTS ANALYSIS

4.1 Simulation Results of the Two Flow Channels

This study conducts flow field–temperature field coupled simulations on both traditional serpentine flow channels and cross-counter flow channels, and analyzes the simulation results. Figures 5 and 6 show the temperature cloud maps of the two liquid cooling plates under a flow condition of 0.3 m/s.

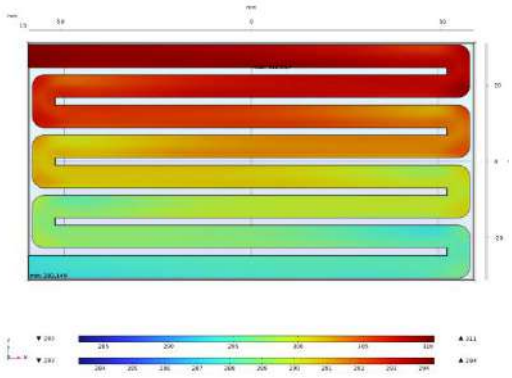

Fig.5: Temperature distribution of conventional serpentine flow channel

As shown in Figure 5, the temperature distribution cloud map of the traditional serpentine flow channel under the condition of 0.3 m/s is illustrated. The flow channel has a long flow path, resulting in significant differences in fluid residence time and heat transfer intensity across various sections. When the fluid first enters, its temperature is 283 K, and the heat transfer efficiency is high; however, by the time the fluid reaches the end, it has absorbed a large amount of heat, causing a substantial decline in the heat transfer capability at the channel's end. At this location, the battery temperature rises to 310 K, forming a 'heat transfer dead zone' and becoming a local hot spot.

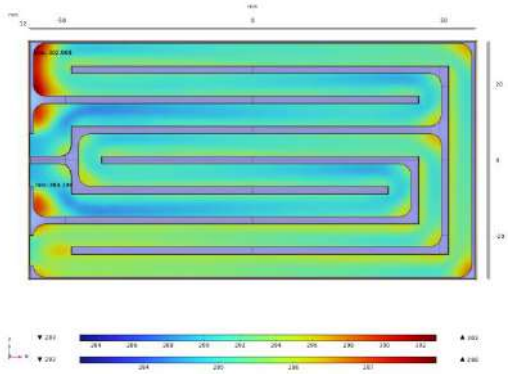

Fig.6: Temperature distribution diagram of cross-counter flow channel

As shown in Figure 6, the temperature distribution cloud map of the cross-counter flow channel under the operating condition of 0.3 m/s indicates that the cross-structure design divides the fluid into two sub channels, shortening the length of a single flow path and reducing the residence time of the fluid in the heat exchange area. The counter flow arrangement reduces the heat exchange temperature difference between the hot and cold fluids to 21 K, while the maximum temperature of the battery decreases to 304 K, maintaining a high degree of temperature uniformity throughout the channel, suppressing local overheating, and

thereby ensuring the consistency of the temperature distribution.

4.1.1 Analysis of Temperature Uniformity

The temperature difference is an important indicator for measuring the temperature uniformity of a liquid cooling plate, and the temperature uniformity of the liquid cooling plate, along with its resistance to local overheating, are key metrics that determine its thermal performance ceiling, system reliability, and device lifespan. The better the temperature uniformity and the weaker the local overheating, the higher the overall heat dissipation efficiency, the lower the thermal resistance, and the more stable the system. The temperature differences of the two types of channels at different flow rates are shown in Figure 7.

Fig. 7 shows the temperature difference R_T of the traditional serpentine and cross counter flow channels with flow velocity v. It can be seen that as the flow rate increases from 0.2m/s to 0.7m/s, the temperature difference of the two runners is downward.

(1) The serpentine flow channel $R_{T,S}$ decreased from 27.0 K to 24.3 K, a decrease of approximately 9.9%;

(2) The cross-counter flow channel $R_{T,C}$ decreased from 19.8 K to 16.8 K, a decrease of approximately 15.2%.

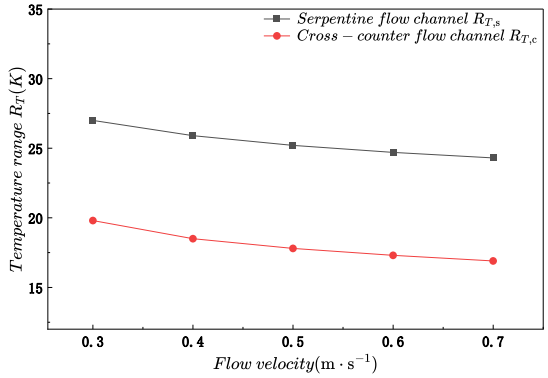

Fig.7: Temperature range of the two flow channels

This indicates that an increase in flow velocity can improve overall temperature uniformity. The cross-counter flow channel shows a more significant response to changes in flow velocity, suggesting that its flow field and temperature field achieve better synergistic optimization.

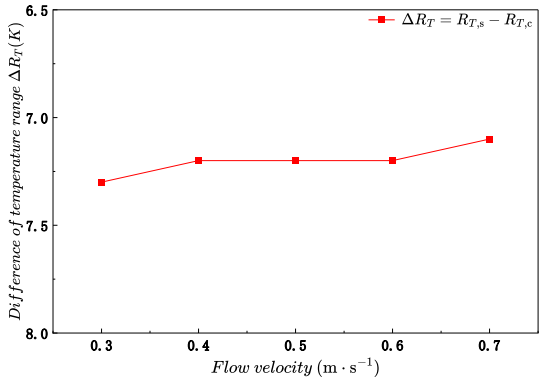

Fig.8: Difference in temperature range between the two flow channels

Figure 8 shows the variation of the difference $\Delta R_T = R_{T,S} - R_{T,K}$ in the maximum temperature difference between the two types of flow channels with flow rate. It can be seen that ΔR_T remains basically stable between 7.1 and 7.2 K. This indicates that the temperature uniformity of the cross-counter flow channel is superior to that of the traditional serpentine channel at different flow rates.

4.1.2 Analysis of Temperature Uniformity Coefficient

The temperature uniformity coefficient is an important reference for assessing the temperature uniformity of the liquid cooling plate. As shown in Figure 9, the highest temperatures of the two flow channels under various operating conditions were obtained through simulation, and Figure 10 presents the results calculated using the temperature uniformity formula:

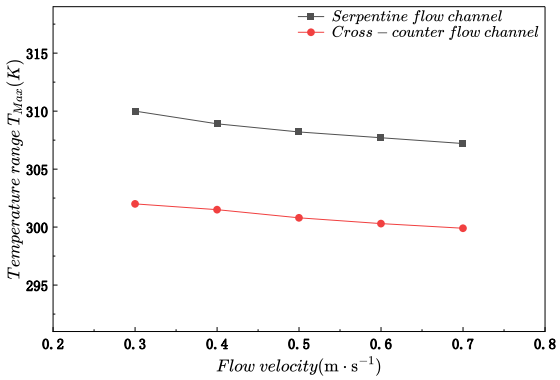

Fig.9: Line graph of maximum temperature for the two flow channels

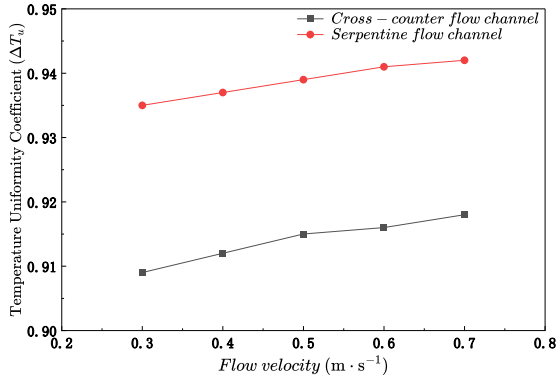

Fig.10: Temperature uniformity coefficient of the two flow channels

The temperature uniformity coefficient ΔTu of the cross-counter flow channel stabilizes in the range of 0.935 to 0.942, compared to 0.909 to 0.918 for the traditional serpentine channel, with an average increase of 0.025. Therefore, it can be considered that the cross-counter flow channel has better temperature uniformity compared to the traditional serpentine channel.

4.1.3 Performance Comparison of the Two Flow Channels

Temperature difference is a key indicator for evaluating the uniformity of the surface temperature distribution of a liquid-cooled plate, as it directly reflects its thermal management capability. The figure below shows a bar comparison of the temperature differences in cross-counter flow channels.

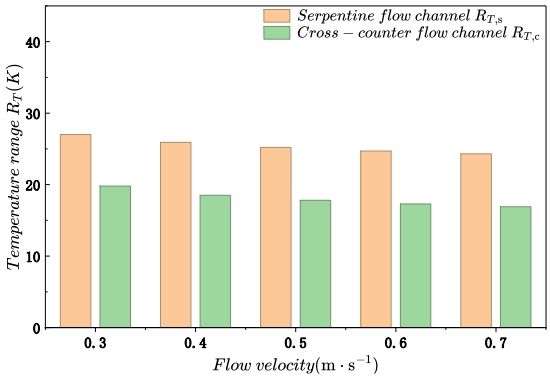

Fig.11: Bar chart of temperature range for the two flow channels

As shown in Figure 11, under all flow rate conditions, the temperature difference $R_{T,C}$ of the cross-counter flow channel is significantly lower than the $R_{T,S}$ of the serpentine channel. Taking a flow rate of 0.3 m/s as an example, $R_{T,C}$ is 7.2 K lower than $R_{T,S}$, with a reduction of 26.7%; even when the flow rate increases to 0.7 m/s, $R_{T,C}$ remains 7.5 K lower than $R_{T,S}$, a decrease of 30.9%. This result indicates that the local overheating problem significantly enhances temperature uniformity and resistance to local overheating.

4.2 Analysis of Pressure Drop Characteristics

4.2.1 Analysis of the Static Pressure Contour of Two Types of Liquid Cooling Plates

The static pressure contour map can visually display the distribution of static pressure inside the liquid-cooled plate flow channel, clearly reflecting the pressure level and attenuation trend through color changes.It can not only qualitatively judge the overall pressure drop, but also accurately identify the sources of resistance along the way and local resistance. It is an important basis for analyzing the pressure drop characteristics of liquid cooling plate, optimizing the channel structure, and improving the heat dissipation and flow performance.

As shown in Figure 12, the static pressure contour of the traditional serpentine channel shows a uniform gradient attenuation along the static pressure, and the color smoothly transitions from the dark red at the inlet to the dark blue at the outlet.This shows that the pressure drop mainly comes from the friction loss along the way, while the local loss at the U-bend is relatively small.The advantages of this design are uniform flow field and stable flow distribution, but the disadvantages are high total pressure drop.

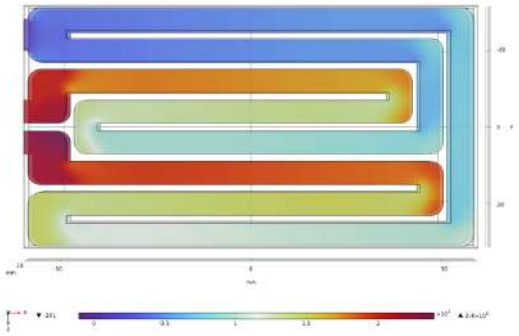

Fig.12: Static pressure contour of cross-counter flow channel

Figure 13 depicts the static pressure contour map of the cross-counter flow channel. Its total pressure drop (approximately 2.4×10^3 Pa) is notably lower than that of the traditional serpentine channel, directly reducing the driving power requirement of the circulating pump. By repeatedly changing the fluid flow direction within a limited space, the cross-counter flow channel achieves higher space utilization, making the overall structure of the liquid-cooled plate more compact within the same plate size. It is suitable

for integration scenarios with limited space and exhibits strong heat transfer performance.

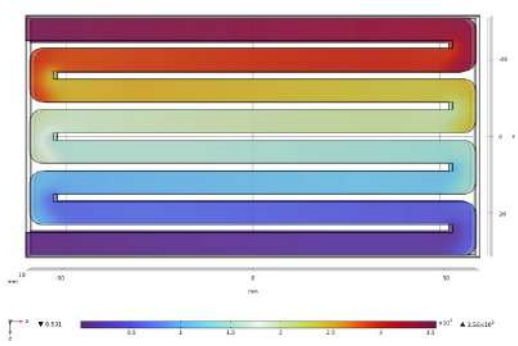

Fig.13: Static pressure contour of serpentine flow channel

4.2.2 Comprehensive comparison of pressure drop between two kinds of liquid cooling plates

In the liquid-cooled plate channel system, the pressure drop is positively correlated with the flow resistance. The pressure drop is the core physical parameter for quantifying the magnitude of flow resistance within the channel, and its value equals the total pressure difference between the channel inlet and outlet. Therefore, a comparative analysis of the pressure drop characteristics of serpentine channels and cross-counter flow channels under different flow rates is conducted.

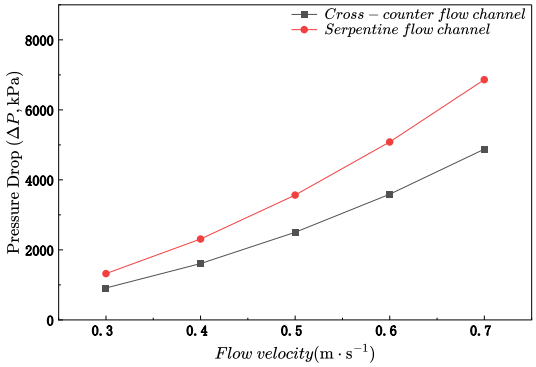

Fig.14: Line graph of pressure drop for the two flow channels

As shown in Figure 14, the pressure drop of cross counter current channel and traditional serpentine channel increases with the increase of flow rate, and the traditional serpentine channel has a faster lifting speed. When the flow rate is 0.3m/s, the pressure drop of serpentine channel and cross counter current channel is about 0.9kPa and 1.3kPa respectively; When the flow rate increases to 0.7m/s, the pressure drop increases to about 4.9kPa and 6.9kPa, respectively. The pressure drop in the cross counter current channel is about 41% higher than that in the traditional serpentine channel.

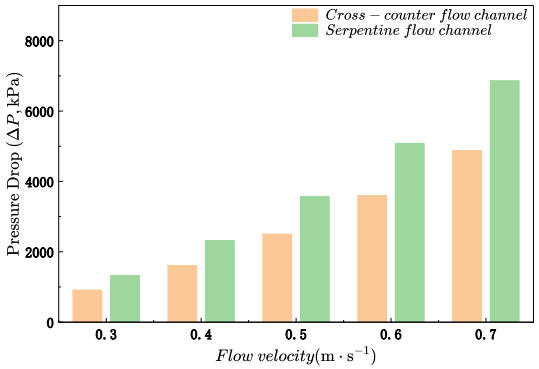

Fig.15: Bar chart of pressure drop for the two flow channels

As shown in Figure 15, the pressure drop of the cross counter current channel is higher than that of the serpentine channel in the speed range, so it can be concluded that the cross counter current channel has lower flow resistance, which can effectively reduce the driving power demand of the circulating pump, and reduce the system energy consumption and operation cost.

V. CONCLUSION

For the cross counter flow channel cold plate proposed in this study, the influence of channel velocity on pressure loss and cooling effect was studied:

(1) In terms of pressure drop characteristics, the growth rate of pressure drop in the serpentine channel is significantly faster than that in the cross counter current channel, and in the five groups of flow rates, the pressure drop in the serpentine counter current channel is higher than that in the cross counter current channel, with an average increase of 42.6%. Therefore, it can be seen that the flow resistance of cross counter current channel is significantly less than that of traditional serpentine channel.

(2) In terms of temperature uniformity, the temperature range of the cross counter current channel is significantly lower than that of the traditional serpentine channel under all flow rates. Taking the flow rate of 0.1m/s as an example, RT and s are 7.2K lower than R_T and C, with a decrease of 26.7%. Even at the flow rate of 0.7m/s, R_T and s are 7.5K lower than R_T and C, with a decrease of 30.9%, indicating that the cross counter current channel is superior to the traditional serpentine channel in temperature uniformity and local hot spot resistance.

In general, the cross counter current channel shows lower flow resistance in pressure drop characteristics, and

has more obvious advantages in temperature uniformity, which can effectively suppress the temperature difference inside the battery pack and improve the reliability and safety of the cooling system.

ACKNOWLEDGEMENTS

This work was supported by the Research Funding of GDUPT, Research on Heat Transfer Enhancement of Heat Sink by Inverse Calculation Design Method (No. 2019rc074) and Research on Intelligent Monitoring and Control Technology of Air Conditioning Noise Based on Quantitative Conjugate Gradient Method. Guangdong College Students' Innovation and Entrepreneurship Program in 2025, (Project No.: 25A015).

REFERENCES

[1] YAN H C, ZHANG X L. Heat dissipation performance of battery cooling system with composite phase change and air [J]. Cryogenics and Superconductivity, 2021, 49(12): 58-64.

[2] LAO Y L. Design and simulation analysis of liquid cooling structure for lithium battery [J]. Cryogenics and Superconductivity, 2021, 49(04): 78-84.

[3] Choudhari V G, Dhoble A S, Panchal S, et al. [J]. Journal of Energy Storage, 2021, 43: 103234.

[4] Luo J, Zou D Q, Wang Y S, et al. [J]. Chemical Engineering Journal, 2022, 430: 132741.

[5] Zhuang W C, Liu Z T, Su H Y, et al. [J]. Applied Thermal Engineering, 2021, 189: 116767.

[6] ZHANG H, ZHAO J, ZHANG Y D, et al. Study on the characteristics of intercooling plate for automotive power lithium battery cells [J]. Machinery Design & Manufacture, 2023, (06): 234-238+243.

[7] WU Z Z, TIAN L T, LIU J Z. Experimental study on liquid cooling thermal management of cylindrical lithium batteries [J]. Cryogenics and Superconductivity, 2022, 50(02): 42-48.

[8] Xie J, Ge Z, Zang M, et al. Structural optimization of lithium-ion battery pack with forced air cooling system [J]. Applied Thermal Engineering, 2017, 126: 583-593.

[9] Rao Z, Qian Z, Kuang Y, et al. Thermal performance of liquid cooling based thermal management system for cylindrical lithium-ion battery module with variable contact surface [J]. Applied Thermal Engineering, 2017, 123: 1514-1522.

[10] Karimi G, Azizi M, Babapoor A. Experimental study of a cylindrical lithium ion battery thermal management using phase change material composites [J]. Journal of Energy Storage, 2016, 8: 168-174.

[11] Zhao R, Gu J, Liu J. Optimization of a phase change material based internal cooling system for cylindrical Li-ion battery pack and a hybrid cooling design [J]. Energy, 2017, 135: 511-522.

[12] Shah K, Mckee C, Chalise D, et al. Experimental and numerical investigation of core cooling of Li-ion cells using heat pipes [J]. Energy, 2016, 113: 852-860.

[13] BERNARDI D, PAWLIKOWSKI E, NEWMAN J. A general energy balance for battery systems [J]. Journal of the Electrochemical Society, 1985, 132(1): 5-12.

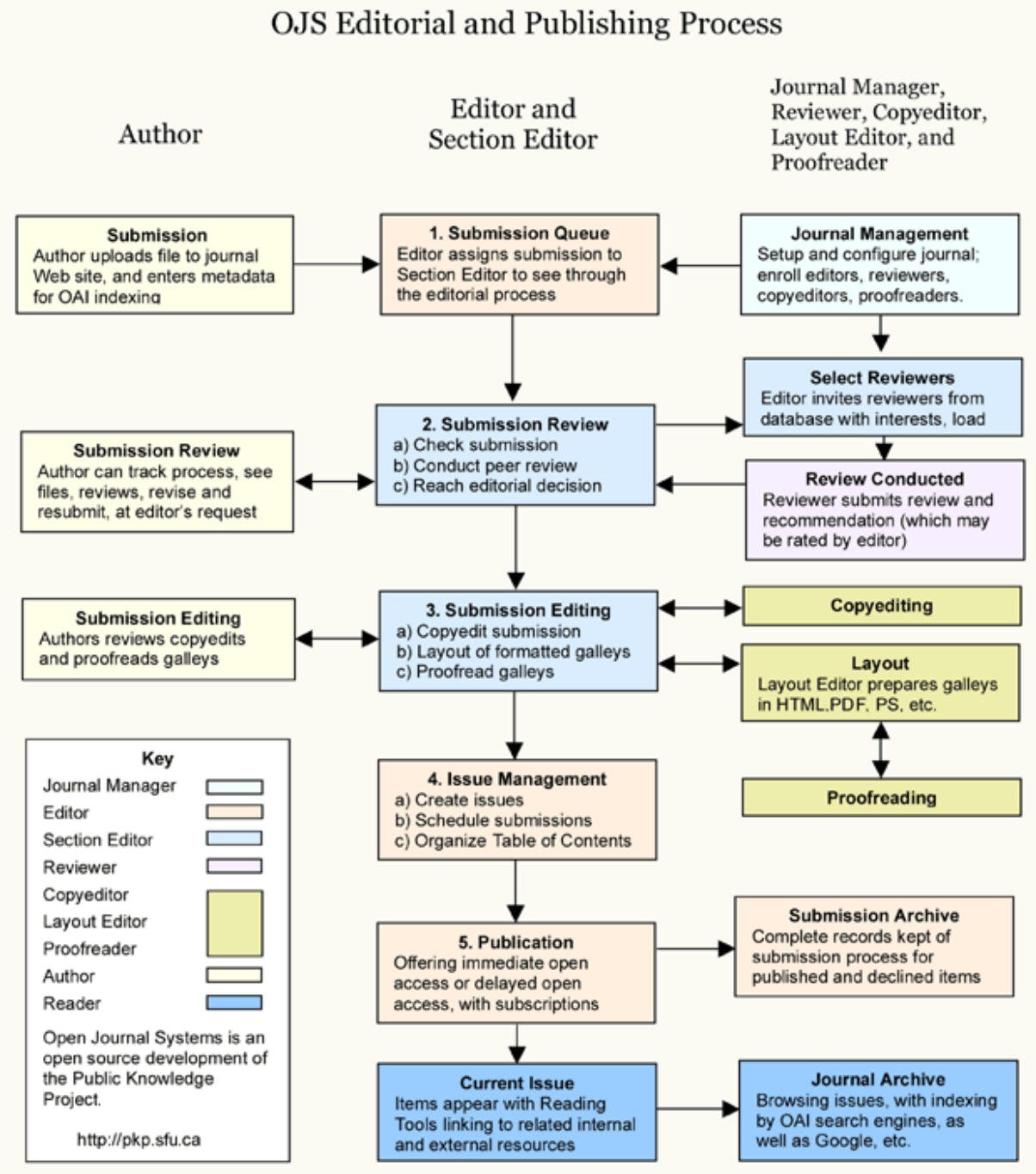

~IJAERS Workflow~

Important links:

Paper Submission Link:
https://ijaers.com/submit-paper/
Editorial Team:
https://ijaers.com/editorial-board/
Peer Review Process:
https://ijaers.com/peer-review-process/
Publication Ethics:
https://ijaers.com/publication-ethics-and-publication-malpractice-statement/
Author Guidelines:
https://ijaers.com/instruction-to-author/
Reviewer Guidelines:
https://ijaers.com/review-guidelines/

Journal Indexed and Abstracted in:

- Qualis-CAPES (A2)-Brazil
- Normatiza (Under Review-Ref.020191511)
- NAAS Score: 3.18
- Bielefeld Academic Search Engine(BASE)
- Aalborg University Library (Denmark)
- WorldCat: The World's Largest Library Catalog
- Semantic Scholar
- J-Gate
- Open J-Gate
- CORE-The world's largest collection of open access research papers
- JURN
- Microsoft Academic Search
- Google Scholar
- Kopernio - powered by Web of Science
- Pol-Index
- PBN(Polish Scholarly Bibliography) Nauka Polaska
- Scilit, MDPI AG (Basel, Switzerland)
- Tyndale University College & Seminary
- Indiana Library WorldCat
- CrossRef DOI-10.22161/ijaers
- Neliti - Indonesia's Research Repository
- Journal TOC
- WIKI-CFP
- Scinapse- Academic Search Engine
- Mendeley-Reference Management Software & Researcher Network
- Dimensions.ai: Re-imagining discovery and access to research
- Index Copernicus Value(ICV): 81.49
- Citeseerx
- Massachusetts Institute of Technology (USA)
- Simpson University (USA)
- University of Louisville (USA)
- Biola University (USA)
- IE Library (Spain)
- Mount Saint Vincent University Library (Halifax, Nova Scotia Canada)
- University Of Arizona (USA)
- INDIANA UNIVERSITY-PURDUE UNIVERSITY INDIANAPOLIS (USA)
- Roderic Bowen Library and Archives (United Kingdom)
- University Library of Skövde (Sweden)
- Indiana University East (campuslibrary (USA))
- Tilburg University (The Netherlands)
- Williams College (USA)
- University of Connecticut (USA)
- Brandeis University (USA)
- Tufts University (USA)
- Boston University (USA)
- McGill University (Canada)
- Northeastern University (USA)
- BibSonomy-The blue social bookmark and publication sharing system
- Slide Share
- Academia
- Archive
- Scribd
- ISRJIF
- Cite Factor
- SJIF-InnoSpace
- ISSUU
- Research Bib
- infobaseindex
- I2OR
- DRJI journal-repository

AI Publication
International Journal of Advanced Engineering Research and Science (IJAERS)
104/108, Sector-10, Pratap Nagar, Jaipur, India